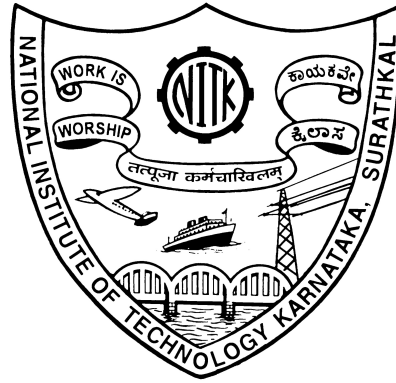


# PERFORMANCE ANALYSIS AND ENHANCEMENT OF ROFSO COMMUNICATION SYSTEM

Thesis

Submitted in partial fulfillment of the requirements for the degree of  
DOCTOR OF PHILOSOPHY

by  
**ABHISHEK KUMAR**



DEPARTMENT OF ELECTRONICS AND COMMUNICATION ENGINEERING  
NATIONAL INSTITUTE OF TECHNOLOGY KARNATAKA  
SURATHKAL, MANGALORE - 575025

October 2024



## DECLARATION

I hereby *declare* that the Research Thesis entitled **PERFORMANCE ANALYSIS AND ENHANCEMENT OF ROFSO COMMUNICATION SYSTEM** which is being submitted to the *National Institute of Technology Karnataka, Surathkal* in partial fulfillment of the requirement for the award of the Degree of *Doctor of Philosophy* in **Department of Electronics and Communication Engineering** is a *bonafide report of the research work carried out by me*. The material contained in this Research Thesis has not been submitted to any University or Institution for the award of any degree.



ABHISHEK KUMAR

Reg. No. 207510/207EC014

Department of Electronics and Communication Engineering.

Place: NITK, Surathkal.


Date: 29/10/2024



# CERTIFICATE

This is to certify that the Research Thesis entitled **PERFORMANCE ANALYSIS AND ENHANCEMENT OF ROFSO COMMUNICATION SYSTEM** submitted by Mr. **ABHISHEK KUMAR** (Register Number: 207510/207EC014) as the record of the research work carried out by him, is accepted as the *Research Thesis submission* in partial fulfillment of the requirements for the award of degree of **Doctor of Philosophy**.

Research Guide



(Dr. PRABU K)

Chairman-DRPC



(Prof. Neelawar Shekar Vittal Shet)

प्राध्यापक एवं विभागाध्यक्ष/PROF & HEAD  
इ. एवं सी. विभा. / Department of E & C  
एन.आई.टी.के. सुरथकल/NITK Surathkal  
मंगलूर / MANGALURU - 575 025

## Acknowledgements

I thank my esteemed research advisor, **Dr. Prabu K**, for his unwavering guidance and mentorship throughout the research journey. His invaluable suggestions and insightful guidance were instrumental in keeping me on the right path. Engaging in discussions with him broadened my understanding and fostered a deeper analysis of complex concepts. I am profoundly indebted to him for his unwavering support, astute guidance, and encouragement, which have been pivotal to my research endeavours.

My sincere gratitude also goes to **Prof. T. Laxminidhi**, who served as the Head of the Department of Electronics and Communication Engineering during my enrollment in the Ph.D. program. Likewise, I extend my appreciation to **Prof. Ashvini Chaturvedi** and **Prof. N. S. V. Shet**, who assumed leadership roles within the Department of E & C Engineering during the course of my research. Their unwavering support, assistance, and encouragement have been instrumental in my academic journey.

I am immensely thankful to my Research Program Advisory Committee (RPAC) members, specifically **Dr. Vignesh Kumar V** from the Department of Electrical and Electronics Engineering and **Dr. Sandeep Kumar** from the Department of E & C Engineering. Their invaluable comments and suggestions have consistently enhanced the quality of my research.

My heartfelt thanks to my course instructors, including **Dr. Prashantha Kumar H.**, **Dr. A. V. Narasimhadhan**, and **Prof. Muralidhar Kulkarni**, for their dedication to imparting knowledge. Additionally, I thank **Prof. A. H. Sequeria** for his exemplary guidance during the research methodology course.

I wish to acknowledge the diligent reviewers of journals who offered constructive suggestions, significantly contributing to the refinement of my research work.

I owe a debt of gratitude to my seniors, **Dr. L. Bhargav Kumar** and **Dr. Pradeep Gorre**, for their invaluable technical discussions and firm support.

I would also like to thank the dedicated faculty members and staff of the E & C Department at NITK Surathkal, whose assistance has been invaluable.

I also thank the staff in Academic, Admission and Cash sections of NITK for their assistance.

My appreciation extends to all my friends and colleagues at NITK for their unwavering support, which has made my time at the institution genuinely memorable.

In this journey, I am deeply thankful to my parents, **Sri. Arjun Prasad** and **Smt. Manorma Sinha**, my wife **Mrs. Jyoti Mahato**, and my sister **Ms. Anupma Kumari**, for their enduring support, boundless love, and unwavering encouragement.

I reserve a special place in my heart for all the teachers who have guided, inspired and encouraged me, nurturing my growth professionally and personally throughout my life.

Lastly, I thank the divine for blessing me with good health, strength, and serenity during my research work.

ABHISHEK KUMAR

Place: NITK, Surathkal

Date:

Dedicated to  
**My Parents & Family**



# Abstract

Radio over Free Space Optics (RoFSO) communication is a promising technology addressing the escalating demands for high bandwidth and rapid data transfer, capitalizing on its inherent capacity to transcend conventional radio transmission capabilities. The features of RoFSO includes huge bandwidth, license free spectrum, low power consumption and immunity from electromagnetic interference. However, RoFSO's complete potential is only attainable when it effectively mitigates the adverse influences of the atmospheric channel, encompassing scattering, absorption, turbulence, and the pervasive issue of pointing errors. In this thesis, we have introduced mitigation techniques Multiple Input Multiple Output (MIMO), Reed Solomon (RS) and Bose-Chaudhuri-Hocquenghem (BCH) error correcting codes, and Reconfigurable Intelligent Surface (RIS) to overcome these challenges.

In our first research work, we harnessed spatial diversity at transmission and reception ends to bolster RoFSO performance across diverse turbulence and meteorological scenarios. Employing the Malaga distribution for modelling atmospheric turbulence, we examined configurations spanning Single Input Single Output (SISO), Single Input Multiple Output (SIMO), Multiple Input Single Output (MISO), and MIMO. We derived closed-form expressions for the average bit error rate (ABER) within this framework. We also explored two combining techniques, Optimal Combining and Equal Gain Combining, to further improve system performance.

In our second research work, we introduced error-correcting codes RS and BCH for binary phase shift keying (BPSK) orthogonal frequency division multiplexing (OFDM) based RoFSO for 5G applications. This pioneering approach yielded impressive results, with an ABER of  $10^{-6}$  achieved at carrier to noise plus distortion ratio (CNDR) of 40 dB, 17 dB, and 4 dB for the uncoded, RS-coded, and BCH-coded systems, respectively, under conditions of weak turbulence.

RoFSO's inherent line of sight (LOS) nature led to the emergence of skip zone challenge in targeted areas ; to address this obstacle, our third research work introduced RIS to facilitate LOS connections, extending com-

munication channel coverage in a smart and controllable manner. Robust performance analysis, incorporating outage probability, ergodic channel capacity, and ABER assessment with heterodyne detection, substantiated the merits of RIS in resolving LOS challenges.

Our fourth research work unveiled a multi-RIS-assisted RoFSO system operating within the dynamic framework of the Malaga distributed atmospheric turbulence model. This comprehensive exploration yielded precise closed-form expressions for performance metrics, encompassing outage probability, ergodic channel capacity, and ABER. The inquiry embraced heterodyne detection and scrutinized two modulation schemes, namely differential binary phase-shift keying (DBPSK) and M-ary quadrature amplitude modulation (M-QAM). Comparisons were drawn across different turbulence conditions, link lengths, and scattering error conditions. The findings underscored the advantages of deploying a multi-RIS-assisted RoFSO system, particularly in vehicular communication scenarios.

**Keywords:** Free Space Optics; Radio over Free space optics communication; Multiple-Input Multiple-Output; BCH Code; RS Code; Reconfigurable Intelligent Surface; Multiple Reconfigurable Intelligent Surface.

# Contents

Acknowledgements . . . . .	i
Abstract . . . . .	v
List of Figures . . . . .	xi
List of tables . . . . .	xv
Abbreviations . . . . .	xvii
Nomenclature . . . . .	xx
<b>1 INTRODUCTION</b>	<b>1</b>
1.1 Research Motivation . . . . .	1
1.2 Free space Optics link . . . . .	6
1.2.1 Transmitter . . . . .	6
1.2.2 Receiver . . . . .	7
1.2.3 FSO Channel . . . . .	8
1.3 RoFSO . . . . .	9
1.4 Applications of FSOC . . . . .	10
1.5 Prior work . . . . .	13
1.6 Problem statement, Objectives and Thesis contributions . . . . .	16
1.6.1 Problem statement . . . . .	16
1.6.2 Objectives . . . . .	16
1.6.3 Main Contribution of the thesis . . . . .	16
1.7 Organisation of the Thesis . . . . .	17
<b>2 Free Space Optical Communication Systems</b>	<b>19</b>
2.1 Atmospheric Attenuation . . . . .	19
2.1.1 Absorption . . . . .	20
2.1.2 Scattering . . . . .	20
2.2 Atmospheric turbulence . . . . .	22

2.2.1	Gamma-Gamma turbulence channel model . . . . .	22
2.2.2	Malaga turbulence channel model . . . . .	23
2.3	Pointing error . . . . .	24
2.4	Mitigation techniques . . . . .	25
2.4.1	Aperture Averaging . . . . .	26
2.4.2	Diversity techniques . . . . .	27
2.4.3	Adaptive optics . . . . .	28
2.4.4	Error correcting Codes . . . . .	29
2.4.5	Hybrid RF/FSO . . . . .	29
2.4.6	Other Mitigation techniques . . . . .	30
2.4.6.1	Pointing, Acquisition, and Tracking (PAT) . . . . .	30
2.4.6.2	Background noise rejection . . . . .	31
2.4.6.3	Reconfigurable Intelligent Surface (RIS) . . . . .	31
2.5	Summary . . . . .	32
<b>3</b>	<b>ABER Performance Enhancement of RoFSO Communication System with MIMO configuration</b>	<b>33</b>
3.1	Introduction . . . . .	33
3.1.1	Contributions . . . . .	34
3.2	System model . . . . .	34
3.3	Channel Model . . . . .	36
3.4	Analysis of SISO RoFSO system . . . . .	40
3.5	Analysis of MIMO RoFSO system . . . . .	41
3.6	Different Combining Techniques . . . . .	42
3.6.1	Optimal Combining . . . . .	42
3.6.2	Equal Gain Combining . . . . .	43
3.7	Results and Discussion . . . . .	44
3.8	Summary . . . . .	48
<b>4</b>	<b>RoFSO communication system's performance enhancement with BCH and RS error correcting codes</b>	<b>49</b>
4.1	Introduction . . . . .	49
4.1.1	Contribution . . . . .	50
4.2	System Model . . . . .	50

4.3	Channel Model . . . . .	52
4.4	BCH Code . . . . .	55
4.5	RS Code . . . . .	57
4.6	Analytical ABER Evaluation . . . . .	57
4.6.1	ABER Evaluation for BCH Coded RoFSO system . . . . .	58
4.6.2	ABER Evaluation for RS Coded RoFSO system . . . . .	59
4.7	Result and Discussion . . . . .	59
4.8	Summary . . . . .	63
<b>5</b>	<b>RIS-aided RoFSO communication system for mitigating skip zone problem</b>	<b>65</b>
5.1	Introduction . . . . .	65
5.1.1	Contribution . . . . .	67
5.2	System model . . . . .	67
5.3	Channel model . . . . .	68
5.4	Closed form Statistical Analysis . . . . .	71
5.4.1	End to End SNR . . . . .	72
5.4.2	PDF in terms of End to End SNR . . . . .	72
5.4.3	CDF in terms of End to End SNR . . . . .	74
5.5	Performance Analysis . . . . .	74
5.5.1	Outage Probability . . . . .	75
5.5.2	Ergodic channel capacity . . . . .	75
5.5.3	ABER for selected binary schemes and M-QAM . . . . .	76
5.6	Results and discussion . . . . .	78
5.7	Summary . . . . .	84
<b>6</b>	<b>RoFSO communication system using multiple RIS for vehicular communication</b>	<b>85</b>
6.1	Introduction . . . . .	85
6.1.1	Contribution . . . . .	87
6.2	System Model . . . . .	87
6.3	Channel model . . . . .	88
6.4	Closed form Statistical Analysis . . . . .	91
6.4.1	Scenario 1 :Single RIS . . . . .	91
6.4.1.1	End to End SNR . . . . .	91

6.4.1.2	PDF in terms of End to End SNR . . . . .	92
6.4.1.3	CDF in terms of End to End SNR . . . . .	94
6.4.2	Scenario 2: Multi-RIS . . . . .	95
6.4.2.1	End to End SNR . . . . .	95
6.4.2.2	PDF in terms of End to End SNR . . . . .	96
6.4.2.3	CDF in terms of End to End SNR . . . . .	98
6.5	Performance analysis . . . . .	98
6.5.1	Outage Probability . . . . .	98
6.5.1.1	Scenario 1: Single RIS . . . . .	98
6.5.1.2	Scenario 2: Multi-RIS . . . . .	99
6.5.2	Ergodic Channel Capacity . . . . .	100
6.5.2.1	Scenario 1: Single RIS . . . . .	100
6.5.2.2	Scenario 2: Multi-RIS . . . . .	101
6.5.3	ABER for DBPSK and M-QAM . . . . .	102
6.5.3.1	Scenario 1: Single RIS . . . . .	102
6.5.3.2	Scenario 2: Multi-RIS . . . . .	104
6.6	Result and discussion . . . . .	106
6.7	Summary . . . . .	113
<b>7</b>	<b>Conclusions and Future Scope</b>	<b>115</b>
7.1	Conclusions . . . . .	115
7.2	Future Scope . . . . .	116
	<b>Publications based on the thesis</b>	<b>134</b>

# List of Figures

1.1	Number of Global IoT-connected devices from 2019 to 2023, with projections extending from 2022 to 2030 [Vailshery (2023)] . . . . .	2
1.2	Block diagram of FSO Communication . . . . .	6
1.3	Different atmospheric effect on FSO link [Trichili <i>et al.</i> (2021)] . . . . .	8
1.4	simplified block diagram of RoFSO communication system. [Jahid <i>et al.</i> (2022)] . . . . .	10
1.5	RoFSO communication system [Jahid <i>et al.</i> (2022)] . . . . .	11
1.6	Few applications of FSO systems [Jahid <i>et al.</i> (2022)] . . . . .	12
2.1	The atmospheric transmission spectrum, extending to 14 $\mu\text{m}$ , delineates wavelength bands in which specific molecules absorb electromagnetic waves. [Garlinska <i>et al.</i> (2020)] . . . . .	20
2.2	FSO Link (a) without Pointing error (b) with pointing error . . . . .	24
2.3	Different mitigation techniques . . . . .	25
2.4	Aperture averaging of FSO transceiver [Jahid <i>et al.</i> (2022)] . . . . .	26
2.5	Visualization of conventional adaptive optics system. [Kaushal and Kaddoum (2016)] . . . . .	28
2.6	(a)RIS offer a solution for mitigating the stringent LOS constraints in FSOC systems (b) RIS allows the redirection of optical beams as desired. [Najafi <i>et al.</i> (2021)] . . . . .	32
3.1	RoFSO system with DPSK modulation . . . . .	35
3.2	RoFSO system model with spatial diversity and MIMO configuration . . . . .	35
3.3	Optical beam propagation in M distribution model. . . . .	38
3.4	Average BER versus Average SNR for SISO and SIMO having EGC and OC combining techniques with different weather conditions (Strong turbulence, $\rho = 0.7$ , $g = 4.167$ ). . . . .	45

3.5	Average BER against Average SNR for SIMO OC with different turbulence conditions (Very clear air weather condition, $\rho = 0.7$ , $g = 4.167$ ).	45
3.6	Average BER against Average SNR for SIMO OC with different pointing error conditions (Very clear air weather condition and strong turbulence).	46
3.7	Average BER against Average SNR for SIMO OC with different diversity schemes (Very clear air weather condition and weak turbulence).	46
3.8	3D Plot for ABER variation(z-axis) with scattering parameter ( $\rho$ ) (y-axis) and $g$ variation(x-axis) (Very clear air weather condition and strong turbulence).	47
4.1	RoFSO link with Bpsk modulation and RS/BCH coding	51
4.2	Block diagram of BCH encoder/decoder	56
4.3	Average BER performance comparison of BCH and RS coded with uncoded OFDM ROFSO communication with different turbulence conditions.	60
4.4	Average BER performance comparison of BCH and RS coded with uncoded OFDM ROFSO communication with different scattering conditions (different $\rho$ values).	60
4.5	Average BER performance comparison of BCH and RS coded with uncoded OFDM ROFSO communication with different weather conditions	61
4.6	Average BER performance comparison of BCH and RS coded with uncoded OFDM ROFSO communication with different pointing errors.	62
5.1	RIS-aided RoFSO system.	68
5.2	Block diagram of RoFSO system.	69
5.3	OP results showing the performance of the RIS-assisted RoFSO system with different turbulence conditions in terms of the SNR.	79
5.4	ECC against SNR for different link lengths of the channel.	80
5.5	ECC against SNR for different turbulence conditions.	80
5.6	ABER against SNR with various QAM and moderate turbulence in the proposed RIS-assisted RoFSO system.	81
5.7	ABER against SNR with different lengths of communication and different modulation schemes in the proposed RIS-assisted RoFSO system.	82

5.8	ABER against SNR with different turbulence conditions and different modulation schemes in the proposed RIS-assisted RoFSO system. . . . .	83
5.9	ABER against SNR with different scattering error and different modulation schemes in the proposed RIS-assisted RoFSO system. . . . .	83
6.1	RIS-assisted RoFSO system for vehicular communication with two scenarios. . . . .	88
6.2	The results of the OP analysis for the RIS-aided RoFSO system under various turbulence conditions and with varying numbers of RISs, in terms of the average SNR. . . . .	107
6.3	ECC against average SNR for various numbers of RISs. . . . .	108
6.4	ECC performance against the average SNR for different turbulence conditions with various number of RISs. . . . .	108
6.5	ECC performance against average SNR for various scattering errors and numbers of RISs. . . . .	109
6.6	The performance of the proposed RIS-assisted RoFSO system in terms of its ABER with respect to average SNR values, considering different communication distances, modulation schemes, and numbers of RISs. .	110
6.7	The performance of the RIS-assisted RoFSO system in terms of ABER for different modulation schemes, turbulence conditions and the number of RISs. . . . .	111
6.8	ABER performance against SNR for various modulation schemes and numbers of RISs, under different levels of scattering error. . . . .	112
6.9	The findings of the OP exact and asymptotic analysis, considering weak turbulence condition and varying number of RISs, are presented in terms of the average SNR for the RIS-aided RoFSO system. . . . .	113



# List of Tables

- 1.1 Comparison among FSO, RF & RoF communication systems [[Majumdar et al. \(2019\)](#), [Mohsan et al. \(2023\)](#)] . . . . . 5
- 2.1 Attenuation coefficient for 1550 nm wavelength [([Balaji and Prabu, 2018b](#))]. . . . . 21
- 3.1 Different attenuation coefficients at 1550 nm [[Kumar and Krishnan \(2020b\)](#)] . . . . . 37
- 3.2 ABER performance comparison at different weather conditions . . . . . 48
- 4.1 Minimal Polynomial of GF( $2^5$ ) for  $t = 4$  [[Ramavath et al. \(2020a\)](#)] . . . . . 56
- 4.2 ABER performance comparison at different turbulence conditions . . . . . 63



## Abbreviations

ABER	Average Bit Error Rate
AO	Adaptive Optics
APD	Avalanche Photodetector
AWGN	Additive White Gaussian Noise
BCH	Bose-Chaudhuri-Hocquenghem
BER	Bit Error Rate
BPSK	Binary Phase-Shift Keying
CBPSK	Coherent Binary Phase-Shift Keying
CDF	Cumulative distribution function
CNDR	Carrier to noise plus distortion Ratio
DBPSK	Differential Binary Phase Shift Keying
DF	Decode and forward
DPIM	Digital Pulse Interval Modulation
DPSK	Differential Phase Shift Keying
ECC	Ergodic Channel Capacity
EGC	Equal Gain Combining
FEC	Forward Error Correction
FOV	Field of View
FSO	Free space optics
FSOC	Free space optical communication
GF	Galois Field
HD	Heterodyne Detection
IM	Intensity Modulation
IM/DD	Intensity Modulation Direct Detection
IMD	Inter-Modulation Distortion
IoT	Internet of Things
IR	Infrared
LAN	Local Area Network
LD	Laser Diode
LDPC	Low-Density Parity-Check
LED	Light Emitting Diode

LOL	Local Oscillator Laser
LOS	Line of Sight
LS	Laser Source
M distribution	Malaga distribution
MIMO	Multiple-Input Multiple-Output
MISO	Multiple-Input Single-Output
MPOLSK	Multilevel Polarization Shift Keying
MRC	Maximal Ratio Combining
NBFSK	non-coherent binary frequency shift keying
NLOS	Non-Line-Of-Sight
NRZ-OOK	Non Return to Zero - On Off Keying
OAM	Orbital Angular momentum
OC	Optimal Combining
OFDM	Orthogonal Frequency Division Multiplexing
OOK	On Off Keying
OP	Outage Probability
PAM	Pulse Amplitude Modulation
PAPR	Peak to Average Power Ratio
PAT	Pointing Acquisition and Tracking
PBS	Polarisation Beam Splitter
PDF	Probability Density Function
PD	Photo Detector
PFM	Pulse Frequency Modulation
PM	Phase Modulation
POLSK	Polarization Shift Keying
PPM	Pulse Position Modulation
PSK	Phase Shift Keying
PSK	Phase Shift Keying
PWM	Pulse Width Modulation
QAM	Quadrature Amplitude Modulation
QPSK	Quadrature Phase shift Keying
QoS	Quality of service
RF	Radio Frequency
RIS	Reconfigurable Intelligent Surfaces

RoF	Radio over Fiber
RoFSO	Radio over Free Space Optics
ROVs	Remotely Operated Vehicles
RS	Reed-Solomon
RZ-OOK	Return to Zero - On Off Keying
SNR	Signal-to-Noise Ratio
SISO	Single-Input Single-Output
SIM	Subcarrier Intensity Modulation
SIMO	Single-Input Multiple-Output
SOP	State of Polarisation
TCM	Trellis-Coded modulation
UAVs	Unmanned Aerial Vehicles
UOWSNs	Underwater Optical Wireless Sensor Networks
UWSNs	Underwater Wireless Sensor Networks
UWOC	Underwater Wireless Optical Communication
UWAV	Underwater Wireless Autonomous Vehicle
V2I	Vehicle to Infrastructure
VLC	Visible Light Communication
WAN	Wide Area Network
WLAN	Wireless local area network
WOC	Wirless Optical Communication

## Nomenclature

$I_l, h_l$	Atmospheric Attenuation
$L$	Link Length
$I, h$	Over all channel effect
$I_a, h_s$	Atmospheric turbulence
$I_p, h_p$	Pointing error
$\Gamma(\cdot)$	Gamma function
$K_v(\cdot)$	Modified Bessel function of second kind
$G_{\cdot}(\cdot)$	Meijer G function
$\gamma$	Instantaneous SNR
$\bar{\gamma}$	Average SNR
$\gamma_{th}$	Threshold SNR
$C_n^2$	Refractive index structure coefficient
$R$	Photodetector Respnsivity
$erfc$	Complementary error function
$\xi, g$	Pointing error Parameter
$\alpha$	Large scale turbulent eddies
$\beta$	Small scale turbulent eddies

# Chapter 1

## INTRODUCTION

The progression of wireless communication applications, marked by the proliferation of devices such as Internet of Things (IoT) devices, gaming consoles, and high-quality video streaming services, has led to a substantial increase in users, demanding advanced network infrastructure. The shift from traditional Radio Frequency (RF) wireless communication systems to higher data rate access became imperative, with the number of users forecasted to grow significantly. The looming bandwidth congestion, particularly at the backhaul end and last-mile access, is expected to intensify with the advent of 5G and beyond services. While fiber optic networks are ideal for backhaul, they pose challenges for last-mile access due to high installation and maintenance costs, especially in rural areas. Free Space Optics (FSO) communication, being wireless, emerges as a promising technology to alleviate the last-mile bottleneck associated with RF technology. FSO communication offers several key features, including its potential for reduced energy consumption compared to RF, massive bandwidth capacity, quick deployment, and high security due to the narrow path vulnerability that discourages eavesdropping. These attributes position FSO as a viable solution to address the evolving demands of wireless communication networks.

### 1.1 Research Motivation

In recent times, diverse multimedia applications have witnessed significant expansion, resulting in a surge of mobile data and high data-rate wireless connectivity. In recent times, diverse multimedia applications have witnessed significant expansion, leading to an increase in mobile data usage and the demand for high-speed wireless connectivity. The upcoming 5G and beyond technology promises an array of appealing services, including extensive system capacity, robust device connectivity, heightened

security, minimal latency, and deficient power consumption, all while delivering an exceptional quality of experience [Ijaz *et al.* (2016), Chowdhury *et al.* (2020)]. Notably, 5G communication envisions ultra-dense heterogeneous networks, supporting substantially higher wireless device connectivity and transmission rates compared to existing networks [Chowdhury *et al.* (2018)]. Consequently, the demand for high-capacity backhaul connectivity to facilitate hyper-dense fast access networks, low power usage, and minimal end-to-end delays in 5G and beyond networks has surged [Attaul Mustafa *et al.* (2016)].

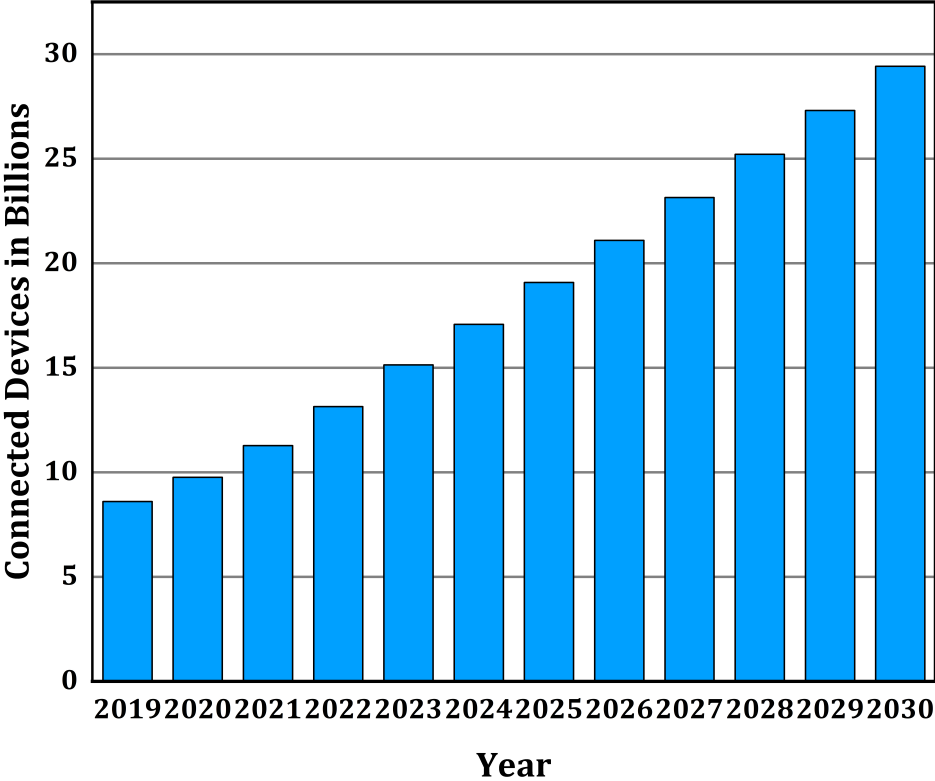


**Figure 1.1:** Number of Global IoT-connected devices from 2019 to 2023, with projections extending from 2022 to 2030 [Vailshery (2023)]

However, managing the unprecedented volume of data in 5G connectivity presents a formidable challenge, necessitating robust technical solutions to guarantee quality of service (QoS) for end users. In contrast, RF technology, commonly employed in

wireless communications, has limitations owing to spectrum scarcity [Obeed *et al.* (2018)], the rapid expansion of the IoT technologies has further compounded this demand. IoT, facilitating real-time communication, sensing, monitoring, and resource sharing across an extensive array of smart devices for social, industrial, and commercial purposes, has led to an exponential rise in connected physical devices [Schulz *et al.* (2017)]. Consequently, as shown in Figure 1.1, the increasing multitude of IoT devices generates a substantial volume of data. To address the mounting requirements of 5G networks and cater to the massive requirements of the IoT landscape, it is apparent that the presently allocated electromagnetic frequency bands (30 kHz to 300 GHz) are insufficient. 5G technology holds the potential to deliver the necessary data rate (1 Gbps) and low latency (in the millisecond range) [Yilmaz *et al.* (2015)]. Achieving this is facilitated by employing low-power small cells, such as microcells and picocells, which enhances network coverage and capacity through the spatial reuse of spectrum. Radio over free space optics (RoFSO) communication can be used to connect the macro, micro and pico cells from one to other and from backhaul network.

Radio frequency typically refers to the electromagnetic spectrum ranging from 30 kHz to 300 GHz, which is primarily utilized in wireless communication. However, with the rising demands of 5G networks and the expanding Internet of Things (IoT) landscape, it is evident that the existing RF spectrum is becoming insufficient to meet these requirements.

RF technology, widely used in wireless communication, faces challenges due to spectrum scarcity, limiting its ability to provide the necessary bandwidth and security for future communication needs. As these demands continue to grow, Free Space Optical Communication (FSOC) emerges as a promising wireless alternative. FSOC not only addresses the limitations of RF technology by offering higher bandwidth and secure communication but also alleviates bottlenecks in last-mile access networks. This makes FSOC an effective solution to bridge the gap between the increasing demand for data and the services provided by traditional RF-based systems.

Radio-over-Fiber (RoF) communication systems offer high bandwidth, minimal signal loss and immunity to electromagnetic interference. They are well-suited for backhaul networks in the context of 5G and beyond services; nevertheless, they may not be the optimal choice for last-mile access due to the significant costs associated with installation and maintenance, which is especially apparent in rural, remote, and architecturally significant areas, including historic city districts and national parks

[Seymour *et al.* (2011)]. Moreover, fiber optic networks represent a wired communication approach, lacking the advantages inherent in wireless communication, such as providing users with the flexibility to access the Internet at any time and from various locations.

The need for extensive bandwidth and secure wireless communication will escalate as we progress. Free space optical communication (FSOC) offers a wireless alternative, positioning it as a suitable option to bridge the disparity between the increasing demand and the services provided by RF technology and also promises to alleviate the bottleneck concerns associated with last mile access networks [Chowdhury *et al.* (2018), Henniger and Wilfert (2010)]. FSO can also contribute to meeting the demanding requirements of 5G and beyond standards.

In RF systems, bandwidth can reach up to 20 % of the carrier frequency. However, in FSOC, with a conservative 1 % bandwidth assumption (approximately  $10^{16}$  Hz), the allowable bandwidth extends to an impressive 100 THz; this puts optical frequencies in the THz range, around  $10^5$  times greater than typical RF carriers [Williams *et al.* (2007)]. FSOC systems utilize very narrow laser beams, resulting in a high reuse factor, inherent security, and robustness against electromagnetic interference. They also have lower power requirements. Furthermore, FSOC technology operates at frequencies above 300 GHz, unlicensed globally, eliminating the need for license fees [Chan (2006)]. FSO systems are known for their ease of deployment and can be reinstalled without incurring the cost associated with dedicated fiber optic connections. Table 1.1 provides a comparative analysis of three distinct communication techniques: FSO, RF, and RoF across various parameters.

Some of the salient features of FSOC:

- According to the report smart 2020 [e Sustainability Initiative *et al.* (2008)], 2% - 10% of worldwide energy consumption occurs from information and communication technology. To decrease global warming, reducing energy consumption is a critical requirement that can be fulfilled through FSO due to its potential for environmentally friendly energy consumption compared to RF. [Bonetto *et al.* (2009)].
- Potentially, FSO can provide a massive bandwidth of 2,000 THz, much higher than the maximum data rate of RF technologies [Sinefeld *et al.* (2013)]. It also allows dense spatial reuse [Saari *et al.* (2013)].

**Table 1.1:** Comparison among FSO, RF & RoF communication systems [Majumdar *et al.* (2019), Mohsan *et al.* (2023)]

Parameter	FSO	RF	RoF
Frequency range	> 300GHz	30KHz to 300 GHz	> 300GHz
Bandwidth	Unlimited	Limited	Unlimited
Data rate	Gbps to Tbps	Mbps to Gbps	Gbps to Tbps
Installation	Moderate	Difficult	Difficult
Bandwidth regulated	No	Yes	No
path loss	High	High	Low
Power consumption	Low-medium	Medium	Depends on the link length
Security at physical layer	Very High	Very Low	High
EMI	No	Yes	No
Communication Distance	$\leq 10$ km (Terrestrial)	$> 100$ km	approximately 100 km without using amplifier or repeater
Coverage	Narrow	Mostly wide	wired communication
Deployment time	low	moderate	high
Initial investment for few subscribers	low	moderate	high

- In a survey, it is established that FSO can be deployed much quicker than any other fixed communication technology [Rahman *et al.* (2008)].
- FSOC is one of the most secure communications because, for eavesdropping, one has to come in contact with a narrow path of FSO, which can cause link outage due to beam obstruction [Liu (2015)].

## 1.2 Free space Optics link

An FSOC system, as depicted in Figure 1.2, primarily operates through line-of-sight communication, facilitating point-to-point data transmission. For selecting the optical wavelength for FSOC, several key factors come into consideration, including atmospheric attenuation, eye safety, the availability of components, and cost-effectiveness. Currently, the wavelength of 1550 nm stands out as the most favoured choice, considering all of these factors carefully. Like other communication technologies, FSOC comprises three crucial components: the transmitter, the atmospheric channel, and the receiver.

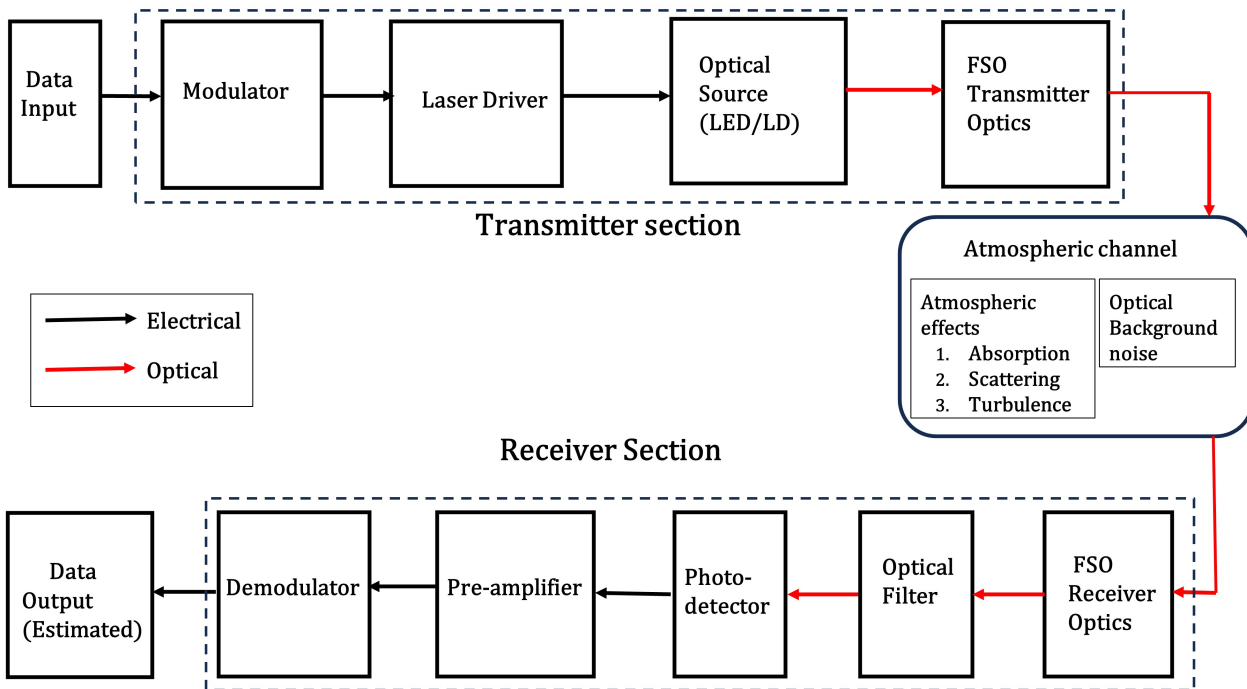


Figure 1.2: Block diagram of FSO Communication

### 1.2.1 Transmitter

The primary function of the transmitter is to modulate the message signal onto the optical carrier and transmit it through the atmosphere to the receiver. As illustrated in Figure 1.2, the critical components of the transmitter encompass the optical modulator, laser driver, optical source, and FSO transmitter optics. An optical modulator is a device that manipulates a specific characteristic of an optical beam generated

from the optical source. The type of modulator used depends on the property of the controlled light and may include intensity modulators, phase modulators, spatial light modulators, and others. In FSO systems, intensity modulation (IM) is commonly employed, where the source data is modulated onto the optical carrier's intensity. The modulation process can be accomplished by directly altering the driving current of the optical source with the message signal or by using an external modulator. Additionally, a laser driver is utilized in FSO systems to maintain the stability of optical emissions, particularly in the presence of temperature fluctuations. The FSO transmitter optics consist of components such as a collimator or telescope, which directs the optical emissions towards the receiver.

In FSO systems, Laser Diodes (LDs) and Light Emitting Diodes (LEDs) are familiar optical sources. LDs are preferred for applications requiring high data rates because of their elevated optical power outputs and wider modulation bandwidths. However, LD usage is subject to standards and power restrictions to ensure safety, particularly concerning eye and skin hazards [Ghassemlooy *et al.* (2019)]. In contrast, LEDs find favour in indoor settings with low to medium data rate requirements due to their cost-effectiveness and reliability. LEDs are considered safer for operation at higher powers because of their extended sources with more significant emitters. However, LEDs are limited to lower data rates compared to LDs [Singh *et al.* (2002)].

## 1.2.2 Receiver

The primary role of the receiver is to retrieve the transmitted data from the incoming optical radiation. Figure 1.2 shows that the receiver consists of several key components, including FSO receiver optics, an optical filter, a photodetector, and a post-detection processor. The FSO receiver optics comprise a telescope that gathers and concentrates the incoming optical radiation onto the photodetector while passing it through the optical filter. This optical filter serves to reduce background noise. On the other hand, the photodetector plays a pivotal role in converting the incident optical signal into an electrical signal. Subsequently, the post-detection processor, which encompasses tasks like demodulation and amplification, is responsible for estimating the transmitted data.

In FSO systems, two primary types of photodetectors are commonly employed: Positive-Intrinsic-Negative (PIN) photodetectors and Avalanche Photodetectors (APDs) [Ghassemlooy *et al.* (2015)]. PIN photodetectors are preferred in low-cost, low-data-

rate FSO links due to their cost-effectiveness, ability to operate at low bias and tolerance to temperature fluctuations [Singh *et al.* (2002)]. In contrast, APDs are PIN photodetectors functioning at significantly high reverse bias levels, resulting in substantial internal electrical gain that bolsters the Signal-to-Noise Ratio (SNR) at the receiver [Heatley *et al.* (1998)]. APDs outperform PIN photodetectors, particularly in systems with limited ambient light noise, making them the preferred choice for high-data-rate and high-performance FSO systems. However, it's worth noting that APDs are comparatively more expensive and exhibit temperature-dependent gain characteristics.

### 1.2.3 FSO Channel

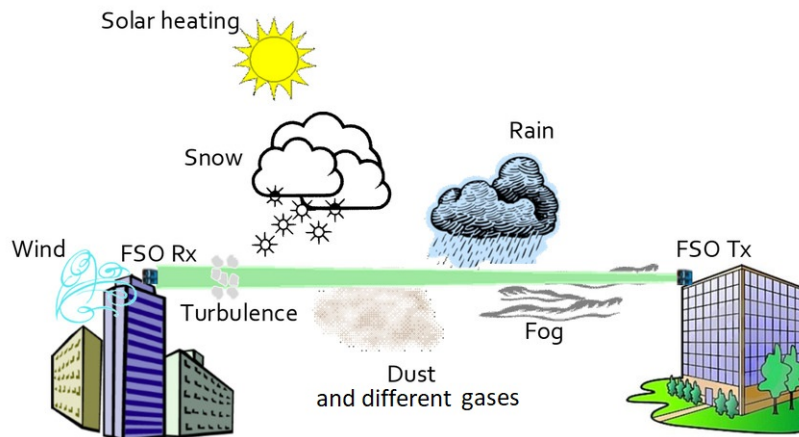


**Figure 1.3:** Different atmospheric effect on FSO link [Trichili *et al.* (2021)]

In FSOC, the communication channel is atmosphere, which is very complex and dynamic. This atmosphere significantly impacts the optical beams traversing through it, resulting in optical power attenuation and turbulence-induced fluctuations in amplitude and phase. Figure 1.3 shows that atmospheric turbulence and spatially varying FSO channel characteristics, influenced by fog, rain, snow, smog and wind, significantly affect optical propagation.

- **Absorption**

In the visible and infrared (IR) spectrums, the primary atmospheric absorbers consist of water molecules, carbon dioxide, and ozone [Long (1963)]. It's essential to note that atmospheric absorption exhibits wavelength dependency,

meaning that the extent to which these molecules absorb optical signals varies with different wavelengths across the spectrum.

- **Scattering**

Light scattering can profoundly influence the performance of FSO systems. Unlike processes associated with the absorption of light energy, scattering doesn't result in energy loss. Instead, it involves the redirection of light, which can substantially reduce the intensity of received light.

- **Atmospheric turbulence**

Atmospheric turbulence arises from uneven temperature distribution on Earth, variable wind speeds, and atmospheric pressure variations due to irregular wind flow, affecting optical beam propagation in both temporal and spatial domains. Factors like moisture, aerosols, temperature variations, and pressure fluctuations create refractive index deviations in air density called eddies. These variations result in phase perturbations of propagating optical light, leading to interference and amplitude variations among wavefronts. Consequently, the received optical signal fluctuates randomly. Additionally, variations in the arrival times of multiple wavefronts lead to temporal fluctuations in light intensity at the receiver's end.

- **Optical background noise**

Within the realm of FSOC, the principal origins of background noise include (a) the pervasive diffused extended noise emanating from the Earth's atmosphere, (b) noise contributions derived from celestial objects such as the Sun and other discrete point sources, and (c) the light that becomes scattered and subsequently collected by the receiver.

### 1.3 RoFSO

Conventional FSO systems have been configured for various digital data transmissions, encompassing diverse data rates such as wireless local area network (WLAN) access points, cellular entry, digital TV, and more. Radio over free space optics (RoFSO) technology represents an advanced approach that facilitates the concurrent transmission and reception of multiple RF signals over FSO links. Figure 1.4 provides a simplified block diagram elucidating the RoFSO system's architecture.

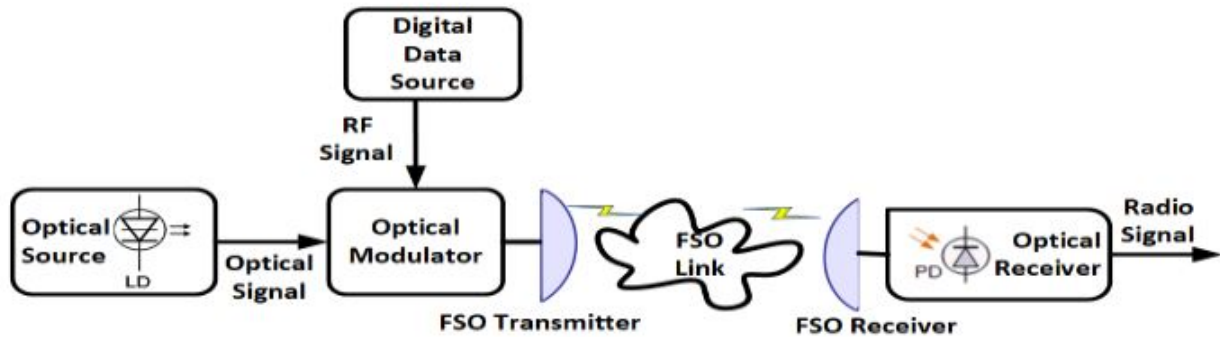


**Figure 1.4:** simplified block diagram of RoFSO communication system. [Jahid *et al.* (2022)]

As a versatile platform for heterogeneous wireless services, RoFSO empowers FSO networks to efficiently transmit multiple high-speed RF signals. This capability is precious in addressing the challenges of various wireless services, each necessitating distinct configurations and dedicated networks. By doing so, RoFSO mitigates high costs and accelerates the deployment of new wireless services, contributing to the evolution of wireless communication networks [Gao *et al.* (2019)].

Figure 1.5 provides an overview of the features characterizing the RoFSO communication system. RoFSO technology is a reliable backup for RoF systems, especially when fiber networks encounter failures or are absent. RoFSO facilitates the transmission of RF signals in scenarios where physical connections via optical fiber cables are economically impractical, offering a capacity similar to RoF but without the reliance on fiber medium. It seamlessly combines the advantages of high transmission capacity associated with optical device technologies with the deployment convenience inherent in wireless links [Kazaura *et al.* (2010)]. The primary goal of the RoFSO link is to achieve comparable capacity to support a diverse range of wireless services akin to RoF. RoFSO transceivers are versatile devices capable of transmitting optical signals from the atmosphere and transmitting them into fiber cores and directly sending RoF signals from optical fibers into free space. This broad range of capabilities underscores the technology's significance in shaping future networks.

## 1.4 Applications of FSOC

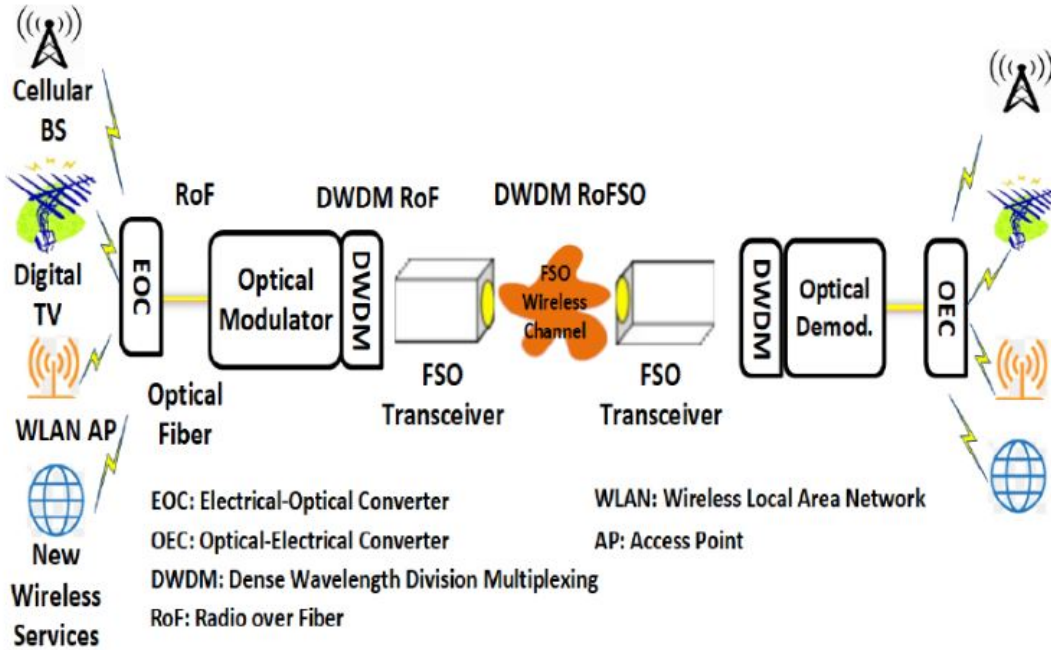


Figure 1.5: RoFSO communication system [Jahid *et al.* (2022)]

FSO systems have gained significant attention due to their efficient resolution of the last-mile connectivity challenge. They offer a promising alternative when deploying buried optical fiber connections is cost-prohibitive or impractical. Various applications of FSO systems are outlined in Figure 1.6 and briefly described below:

- **Inter-building Connectivity:** FSO offers cost-effective, high-speed data connections between diverse infrastructures like school campuses, offices, and corporate setups. It enables enterprise connectivity and facilitates applications like ship-to-ship and community-to-community communications across geographically separated buildings.
- **Video Surveillance and Disaster Monitoring:** FSO systems are ideal for wireless video monitoring, serving military, commercial, and public safety needs with superior throughput compared to conventional methods. They ensure the transmission of high-quality video even in critical scenarios.
- **Video Broadcasting:** FSO systems excel in live event broadcasting, including sports, high-definition services, news coverage, and remote zone reporting. They facilitate the high-quality transmission of camera signals to central nodes and end users.

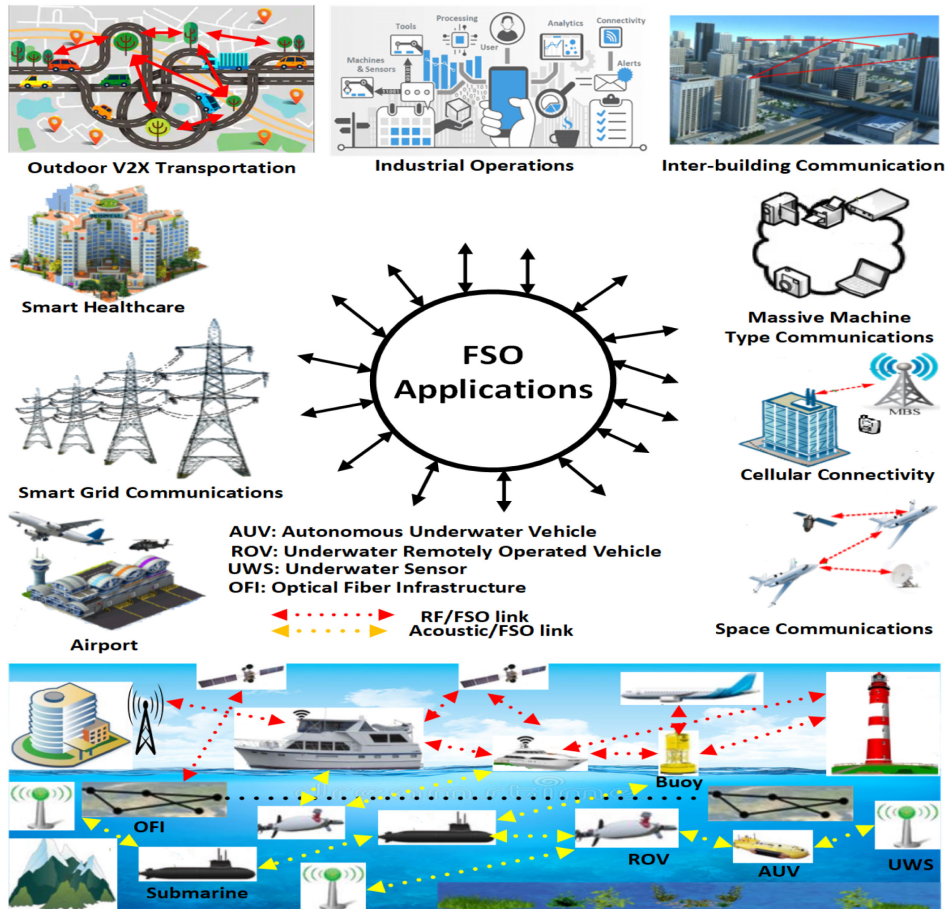


Figure 1.6: Few applications of FSO systems [Jahid *et al.* (2022)]

- Security: With growing concerns about cybersecurity and quantum computing, FSO systems offer enhanced security for applications like secure electronic money transfers. FSO signals are highly secure and cannot penetrate obstacles.
- Last Mile Solution: FSO communication is an essential last-mile solution, particularly for remote end users lacking access to optical fiber infrastructure. It provides high-speed Gbps connectivity over long distances, making broadband internet services accessible in hard-to-reach areas.
- IoT and 5G: FSO technology plays a pivotal role in supporting the extensive deployment of IoT devices, ensuring high bandwidth, low latency, and secure data transmission. When integrated with 5G, FSO links enhance coverage and overall system performance, meeting the demands of global IoT.

- Satellite Communications: FSO technology finds applications in space-related endeavours, including radio astronomy and remote sensing. It offers power-efficient, long-distance inter-satellite orbital links with superior receive sensitivity. Orbital angular momentum (OAM) beams enhance data-carrying capacity, making FSO an excellent choice for deep-space communications.

## 1.5 Prior work

FSOC system is expeditiously becoming a part of the ever-growing technology. Given its advantages, including high security, high bandwidth, license-free spectrum, and cost-effectiveness compared to the long-established RF communication systems. FSO has applications such as terrestrial, deep space, inter-satellite, and inter-orbital links [Kaushal and Kaddoum (2016), Khalighi and Uysal (2014)]. FSO is also helpful in many cases, such as in unmanned aerial vehicles (UAVs), high-speed trains, satellites, building-to-building, indoor and outdoor local area networks (LANs), wide area networks (WANs), and deep-space communications [Chan (2006)].

Multiple input multiple output (MIMO) in RoFSO has become an effective mitigation technique to alleviate the turbulence effect and augment the data rate as extensively investigated in a series of studies [Dabiri *et al.* (2017), Krishnan and Kumar (2014), Kumar and Khandelwal (2019)] and [Bhatnagar and Ghassemlooy (2016)]. These papers have used diverse turbulence modeling such as log-normal, gamma-gamma, or Malaga (M) distribution model. Additionally, [Saeed and Abbas (2018)] conducts a simulation-based analysis of the MIMO FSO system. In contrast, [Pham *et al.* (2018)] delves into the examination of the average achievable rate of MIMO FSO communication over correlated gamma-gamma turbulence channels, considering combining techniques such as Equal Gain Combining (EGC) and Maximal Ratio Combining (MRC). Furthermore, [Safi *et al.* (2019)] scrutinises the influence of factors such as beam wander and non-zero boresight pointing errors on MIMO FSO systems.

RoFSO communication has employed various modulation schemes to mitigate the impact of atmospheric turbulence. These include Pulse Position Modulation (PPM), on-off keying (OOK), Digital Pulse Interval Modulation (DPIM), and Pulse Width Modulation (PWM). OOK modulation is the most prevalent due to its simplicity and cost-effectiveness, as noted in [Zedini and Alouini (2015)]. However, it necessitates using a carefully adjusted adaptive threshold for optimal performance. PPM modulation, as explored in [Pham *et al.* (2014)], has been applied in FSOC but is associated

with relatively low spectral efficiency. PWM, in contrast, requires lower peak power for transmission than PPM and boasts superior spectral efficiency, as elucidated in [Fan and Green (2007)]. Nonetheless, it demands higher average power compared to PPM. DPIM, categorised as an asynchronous modulation scheme due to its variable symbol length [Ghassemlooy *et al.* (1998)], carries an elevated risk of error propagation during signal demodulation at the receiver. Additionally, Subcarrier Intensity Modulation (SIM) has found utility in FSO systems, albeit with limitations in power efficiency [Hassan *et al.* (2019)]. To address these limitations, Orthogonal Frequency Division Multiplexing (OFDM) has emerged as a promising solution, a topic explored in our research. Furthermore, the integration of Binary Phase-Shift Keying (BPSK) with other modulation schemes has been shown to yield enhanced performance, as documented in [Tang *et al.* (2010)] and [Balaji and Prabu (2018a)].

To bring signals parallelly together in OFDM, mutually orthogonal sub-carriers are separated at a specific frequency in the frequency domain. This orthogonalisation of sub-carriers is achieved through Fast Fourier Transformation at the transmitter terminal. Adopting OFDM within RoFSO links, as highlighted in [Sharma and Kaur (2013)], eliminates the adverse effects of co-channel and inter-symbol interference. Furthermore, research, such as that found in [Nistazakis *et al.* (2014)], delves into the investigation of bit error rate (BER) performance in OFDM-based RoFSO, employing Quadrature Amplitude Modulation (QAM) as a critical aspect of their analysis. The study also takes into account the impact of pointing errors. To enhance the data-carrying capacity of FSO links, researchers have explored multiplexing techniques in areas like intensity [Naila *et al.* (2011)], phase [Kanno *et al.* (2011)], code [Al-Khafaji *et al.* (2013)], polarisation [Tang *et al.* (2012)], and wavelength [Zhou *et al.* (2014)]. Additionally, in [Gupta *et al.* (2019)], the performance of a Bose-Chaudhuri-Hocquenghem (BCH) coded FSO link under a Gamma-Gamma turbulence model is thoroughly investigated. Meanwhile, [Ajewole *et al.* (2019)] scrutinises the BER performance of a convolutional coded OFDM-based FSO system operating over a Gamma-Gamma turbulence channel. In recent developments related to 5G New Radio applications, there has been a preference for BPSK-based modulation schemes over higher-order alternatives like Quadrature Phase Shift Keying (QPSK) and 16-QAM. The emergence of a novel modulation scheme,  $\pi/2$ -BPSK, has been proposed and widely adopted in 5G New Radio applications, particularly for uplink data channel and control channel transmissions, as discussed in [Khan *et al.* (2020), Borges *et al.*

(2021)], and [Choi *et al.* (2021)].

In RoFSO communication, Reflecting Intelligent Surfaces (RIS) represent electromagnetic devices that possess electronically controllable attributes. Notably, RIS modules demand less power compared to conventional relays. These modules are constructed with multiple mirrors configured in a planar array, as expounded upon in [Zeng *et al.* (2020)]. Numerous studies have embraced the concept of RIS within FSO systems, including works such as [Ndjiongue *et al.* (2021d,c), Játiva *et al.* (2020), Abdelhady *et al.* (2020), Najafi and Schober (2019), Najafi *et al.* (2021), Jia *et al.* (2020)] and [Ajam *et al.* (2021a)]. In specific instances, like [Ndjiongue *et al.* (2021d)] and [Ndjiongue *et al.* (2021c)], RIS modules were harnessed to amplify incoming optical signals. On a related note, [Abdelhady *et al.* (2020)] explored two types of indoor Visible Light Communication (VLC) RIS structures.

To further illustrate the versatility of RIS-assisted FSO systems, consider the investigation in [Ndjiongue *et al.* (2021b)]. This study scrutinised an RIS-enhanced FSO system, meticulously considering the Gamma-Gamma channel model while varying distances and jitter ratios. Research efforts such as [Najafi *et al.* (2021)] and [Ajam *et al.* (2022)] contemplated RIS-empowered FSO channels. In [Wang *et al.* (2021)], a multi-branch RIS-assisted FSO system was proposed, capitalising on multiple optical RIS infrastructures based on the Gamma function.

Indeed, various inquiries have probed the fundamental characteristics and channel modelling of optical wireless systems featuring RIS across a spectrum of physical scenarios, as evident in [Najafi and Schober (2019), Najafi *et al.* (2021, 2020), Ajam *et al.* (2021b)], and [Yang *et al.* (2020a)]. Furthermore, [Odeyemi *et al.* (2021)] examined RIS's effectiveness within dual-hop decode-and-forward (DF) relay-enabled asymmetric RF/FSO systems. The comprehensive analysis in [Stefanovic *et al.* (2021)] explored RIS-facilitated FSO communication, incorporating the complexities of atmospheric turbulence modelled through the Fisher-Snedecor distribution. This scrutiny accounted for first- and second-order effects, encompassing varying degrees of turbulence-induced fading strength.

However, it's noteworthy that most existing research has primarily centred on single RIS-assisted FSO systems. The idea of deploying multiple RIS in FSOC to establish links between transmitters and receivers has remained relatively underexplored. In the innovative exploration documented in [Chapala and Zafaruddin (2021)], researchers probed the potential of employing multiple RIS elements within a hybrid

FSO and RF system. This innovative approach aimed to enable line of sight (LOS) communication and foster reliable connectivity, particularly in multi-hop transmission within vehicular communications.

## **1.6 Problem statement, Objectives and Thesis contributions**

### **1.6.1 Problem statement**

To analyse the impact of weather conditions, turbulence conditions and pointing error on RoFSO system performance and enhance its performance using various mitigation techniques.

### **1.6.2 Objectives**

This research primarily focuses on analysing the performance of RoFSO communication systems with different mitigation techniques.

1. To enhance the performance of the RoFSO communication system with spatial diversity and MIMO configuration having optimal combining and equal gain combining.
2. To improve the performance of the RoFSO communication system with BCH and Reed-Solomon (RS) error-correcting codes.
3. To analyse the performance of RIS-aided RoFSO communication system for mitigating skip zone problem.
4. To analyse the performance of RoFSO communication system using multiple RIS for vehicular communication.

### **1.6.3 Main Contribution of the thesis**

The following are the contributions of the research work presented in this thesis.

- We proposed the Differential Phase Shift Keying (DPSK) based M-distributed RoFSO system with different configurations, such as single-input single-output (SISO), single-input multiple-output (SIMO), multiple-input single-output (MISO), and MIMO, along with combining techniques, optimal combining (OC) and EGC. Novel closed-form expressions for average bit error rate (ABER) have been estimated.

- We proposed RS and BCH-coded BPSK OFDM-based RoFSO system. We introduced RS and BCH coding techniques in the proposed RoFSO system. The novel ABER expressions are obtained as a closed-form equation.
- RIS-aided RoFSO system over M-distributed turbulence with two binary modulations and M-QAM modulation has been proposed for mitigating the skip zone problem. The closed-form expressions of probability density function (PDF), cumulative distribution function (CDF), outage probability (OP), ergodic channel capacity (ECC) and ABER for the proposed system have been derived.
- To better understand the system performance, we provide a comparative analysis of various metrics for two different scenarios as outlined below:
 

Scenario 1: The performance of a single RIS-aided RoFSO communication system is analysed.

Scenario 2: The multi-RIS-assisted RoFSO system performance is analysed.
- To assess the system's performance, we conducted ABER performance analysis for the first two proposed systems, and for the latter two proposed systems, we conducted ABER, OP and ECC analysis.

## 1.7 Organisation of the Thesis

This thesis comprises seven chapters, structured as follows:

**Chapter 1 :** This chapter outlines the motivation for researching the RoFSO domain and introduces the components and limiting factors of RoFSO communication. It also reviews prior work in this field and presents the problem statement, research objectives, and main contributions.

**Chapter 2 :** This chapter furnishes an overview of the FSO communication channel, elucidating various factors influencing communication. Furthermore, it delves into the mathematical modelling of these effects, focusing on atmospheric attenuation, atmospheric turbulence, and pointing error, providing comprehensive insight into their mathematical representations.

**Chapter 3 :** This chapter analyses the proposed RoFSO system employing DPSK modulation, exploring various configurations, including SISO, SIMO, MISO, and MIMO.

**Chapter 4 :** This chapter investigates the ABER performance of the BPSK RoFSO system with two coding techniques, BCH and RS. It compares the performance of coded and uncoded RoFSO systems.

**Chapter 5 :** This chapter is dedicated to the performance analysis of the RIS-assisted RoFSO system, wherein three modulation techniques, namely non-coherent binary frequency shift keying (NBFSK), coherent binary phase-shift keying (CBPSK), and M-ary quadrature amplitude modulation (M-QAM) are considered.

**Chapter 6 :** This chapter thoroughly analyses the utilisation of multiple RIS elements in RoFSO communication for vehicular communication. This study involves a comparative assessment of two distinct scenarios: one involving a single RIS and the other incorporating multiple RIS elements. The comparative evaluation is performed across three key performance metrics: ABER, OP, and ECC.

**Chapter 7 :** This chapter summarizes the thesis and presents future research directions that can be undertaken.

# Chapter 2

## Free Space Optical Communication Systems

The atmospheric channel is a complex environment comprising various gases and particles, including aerosols, dust, smoke, and precipitation like rain, haze, snow, and fog, all suspended in the atmosphere. These elements collectively contribute to the attenuation of optical signal power. This attenuation occurs mainly through processes such as the absorption of light by gas molecules and different types of scattering, such as Rayleigh or Mie scattering. These atmospheric effects can be categorized into static and dynamic losses. Static losses arise from molecular absorption and scattering within the atmosphere. In contrast, dynamic losses result from the ever-changing atmospheric conditions, including variations in aerosol content like fog, rain, and snow. Dynamic losses also encompass phenomena like scintillation, scattering, and absorption.

Furthermore, the challenges in FSO communication extend to pointing or misalignment errors, which can arise from wind, earthquakes, and building vibrations. Additionally, the necessity for a clear LOS in communication can be challenging when a skip zone problem exists, i.e. obstructions exist between the transmitter and receiver. To address this skip zone problem, RIS has been introduced. This chapter provides an in-depth exploration of these effects, accompanied by a discussion of mitigation techniques employed to alleviate the impacts of atmospheric attenuation, turbulence, and pointing errors while also highlighting the significance and utilization of RIS technology.

### 2.1 Atmospheric Attenuation

Attenuation is a critical propagation effect that makes the transmitted optical signal power unstable as it propagates to longer distances. [Ghassemlooy *et al.* (2019)].

### 2.1.1 Absorption

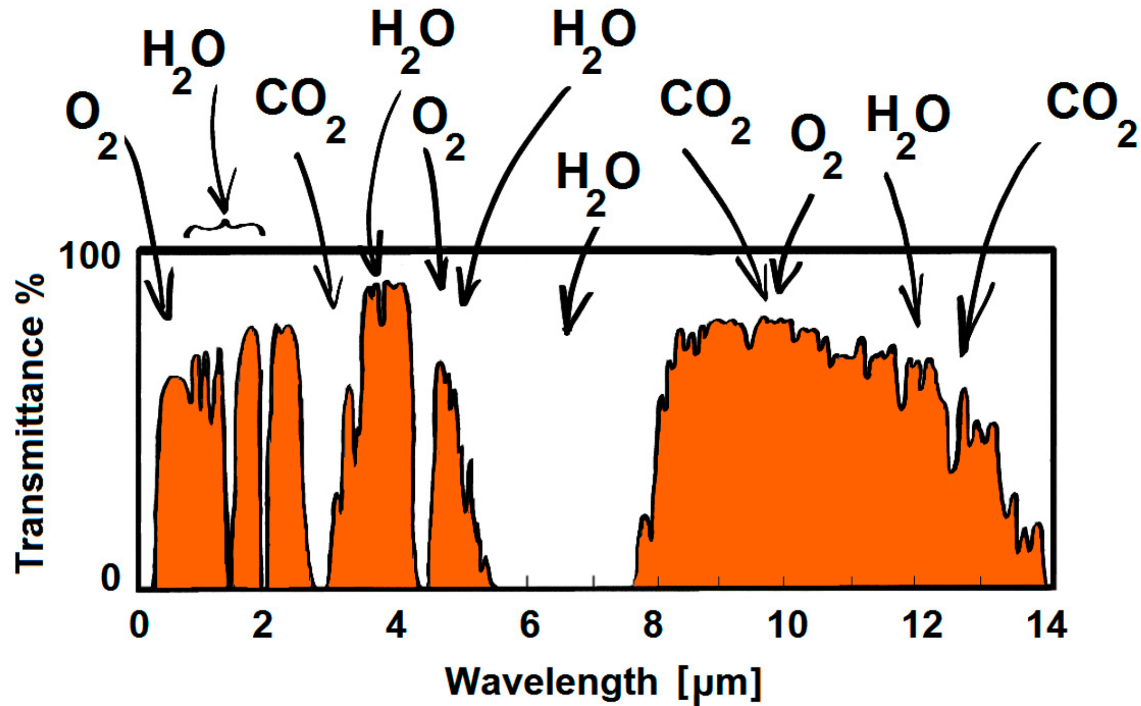


**Figure 2.1:** The atmospheric transmission spectrum, extending to 14  $\mu\text{m}$ , delineates wavelength bands in which specific molecules absorb electromagnetic waves. [Garlinska *et al.* (2020)]

Absorption of the optical signal is influenced by the wavelength-dependent nature of extinction in the atmosphere. Notably, atmospheric gases like  $O_2$ ,  $CO_2$  and water molecules cause broad absorption bands, each comprising numerous fine absorption lines. The spectral distribution of these bands allows for the computation of atmospheric optical transmission windows, ensuring minimal signal losses for the propagating beam. The atmospheric transmission windows, characterized by low radiation absorption, are prominent within specific spectral ranges, as shown in Figure 2.1. Typically, FSO systems exploit the transmission window spanning approximately 0.8 to 1.5  $\mu\text{m}$ , where absorption is relatively low.

### 2.1.2 Scattering

Scattering phenomena occur when light interacts with particles in the medium, resulting in the radiation beam dispersion in various directions or alteration of its path.

Like absorption, scattering significantly impacts FSO systems' performance and is wavelength-dependent. When the particles involved are smaller than the wavelength of the light beam, it is termed Rayleigh scattering. This type of scattering is particularly notable in FSO communication within the visible or ultraviolet range, typically wavelengths below 1  $\mu\text{m}$ .

However, it becomes less significant at longer wavelengths, particularly in the near-IR range. When atmospheric particles are comparable in size to the optical wavelength, Mie scattering becomes dominant, especially in the near-IR wavelength range or beyond. Significant sources of Mie scattering include aerosol particles, fog, and haze. When atmospheric particles such as rain, snow, and haze greatly exceed the optical wavelength, scattering is more accurately described by the geometrical optics model.

**Table 2.1:** Attenuation coefficient for 1550 nm wavelength [(Balaji and Prabu, 2018b)].

<b>Weather condition</b>	$\sigma$ (dB/km)
Very clear air	0.0647
Drizzle	0.2208
Haze	0.7360
Mean rain	0.8793
Strong rain	0.5554
Light Fog	4.2850
Moderate fog	25.5160

Attenuation in the atmosphere is governed by the Beer-Lambert law, which depends on distance and involves the attenuation coefficient, encompassing absorption and scattering coefficients. The atmosphere contains gases like oxygen, methane, carbon dioxide, nitrous oxide, ozone, aerosols, and varying precipitation levels like fog, haze, and rain. Interaction with these atmospheric components causes power loss when an optical signal traverses the atmosphere. This phenomenon is described by the general Beer-Lambert law [Andrews and Phillips (2005)].

$$h_l = \exp(-\sigma L) \tag{2.1}$$

$\sigma$  denotes the attenuation coefficient characterizing the atmospheric channel, while  $L$  signifies the distance separating the source and the destination. The specific values

for the attenuation coefficient in the atmospheric channel can be found in the table [2.1](#).

## 2.2 Atmospheric turbulence

Atmospheric turbulence is a stochastic phenomenon and essentially a result of the varying environmental conditions, that is, air temperature and pressure along the transmission path, leading to the formation of turbulent cells with varying refractive indices referred to as eddies. The intensity of turbulence is quantified by the refractive index structure coefficient denoted as  $C_n^2$ . In case of weak turbulence, its value can be as low as  $10^{-17} m^{-3/2}$ , whereas in scenarios of strong turbulence, it can reach as high as  $10^{-13} m^{-3/2}$ . This turbulence introduces three significant effects on a laser beam: scintillation, beam wandering, and beam spreading.

Scintillation corresponds to the random fluctuations in the intensity of the propagating wave caused by eddies. These eddies, acting like optical elements, induce interference patterns that cause fluctuations in the intensity and phase of received signals. Scintillation is quantified by the scintillation index (SI), categorized as weak ( $SI \ll 1$ ), moderate ( $SI \approx 1$ ), strong ( $SI > 1$ ), and extremely strong ( $SI \gg 1$ ).

Beam wandering occurs when the size of refractive index fluctuations in the atmosphere surpasses the size of the propagating beam. This random fluctuation leads to deviations in the beam's propagation direction, impacting signal quality. Beam wandering becomes more pronounced as the distance increases.

Beam spreading describes the dispersion of the optical beam in the atmosphere, typically occurring when the beam diffracts near the receiver's aperture. Beam spreading due to atmospheric turbulence becomes noticeable when the size of the beam exceeds that of the eddy cells.

Several turbulent channel models have been developed to characterize irradiance fluctuations through PDFs. These models encompass the K-distribution, Negative Exponential, Double Generalized Gamma distributions, and others like lognormal, Malaga, and gamma-gamma. In this context, we will focus on the Malaga and gamma-gamma distribution models due to their applicability across all three turbulence regimes: weak, moderate, and strong.

### 2.2.1 Gamma-Gamma turbulence channel model

The gamma-gamma model encompasses both small-scale and large-scale atmospheric fluctuations, expressing the irradiance as the result of two independent stochastic

processes, each following a gamma PDF with distinct parameters  $\alpha$  and  $\beta$  representing the Rytov variance functions and a geometric factor. This formulation of the PDF for the gamma-gamma turbulence channel model can be described as follows [Andrews and Phillips (2005)]:

$$f_{h_s}(h_s) = \frac{2(\alpha\beta)^{(\alpha+\beta)/2}}{\Gamma(\alpha)\Gamma(\beta)} h_s^{\frac{(\alpha+\beta)}{2}-1} K_{(\alpha-\beta)}\left(2\sqrt{\alpha\beta h_s}\right) \quad (2.2)$$

Here, the expression includes the Gamma function denoted as  $\Gamma(\cdot)$  and the modified Bessel function of the second kind with order  $(\alpha - \beta)$ , represented as  $K_{(\alpha-\beta)}$ . The parameters  $\alpha$  and  $\beta$  correspond to the effective quantities of small-scale and large-scale eddies. Notably, these effective numbers differ when considering a plane wave versus a spherical wave configuration.

### 2.2.2 Malaga turbulence channel model

Over time, several irradiance PDF models have been developed with varying levels of efficacy. The Malaga distribution is a comprehensive statistical model that integrates numerous statistical channel models proposed in multiple studies to describe atmospheric-induced turbulence fading in FSO systems, spanning from weak to strong turbulence conditions. Some notable instances of the Malaga distribution include log-normal, gamma-gamma, Rice-Nakagami, K-distribution, and exponential models.

In the Malaga turbulence channel model, the small-scale fluctuations in the optical signal arising from diffractive effects can be segmented into three distinct components. The first component pertains to the LOS contribution. The second component involves scattering by eddies along the propagation axis, which is interconnected with the LOS component. Conversely, the third contribution accounts for the energy dispersed to the receiver by off-axis eddies, operating independently from the other two components. In contrast, the large-scale fluctuations in the optical signal are presumed to adhere to a gamma distribution.

The Malaga turbulence channel PDF is given as [Jurado-Navas *et al.* (2012b)]

$$f_{h_s}(h_s) = A \sum_{m=1}^{\beta} a_m h_s K_{\alpha-m} \left( 2\sqrt{\frac{\alpha \beta h_s}{g \beta + \Omega'}} \right), \quad (2.3)$$

Where

$$A \triangleq \frac{2 \alpha^{\alpha/2}}{g^{1+\alpha/2} \Gamma(\alpha)} \left( \frac{g \beta}{g \beta + \Omega'} \right)^{\beta+\alpha/2},$$

$$a_m \triangleq \binom{\beta - 1}{m - 1} \frac{(g \beta + \Omega')^{1-m/2}}{(m - 1)!} \left( \frac{\Omega'}{g} \right)^{m-1} \left( \frac{\alpha}{\beta} \right)^{m/2}.$$

### 2.3 Pointing error

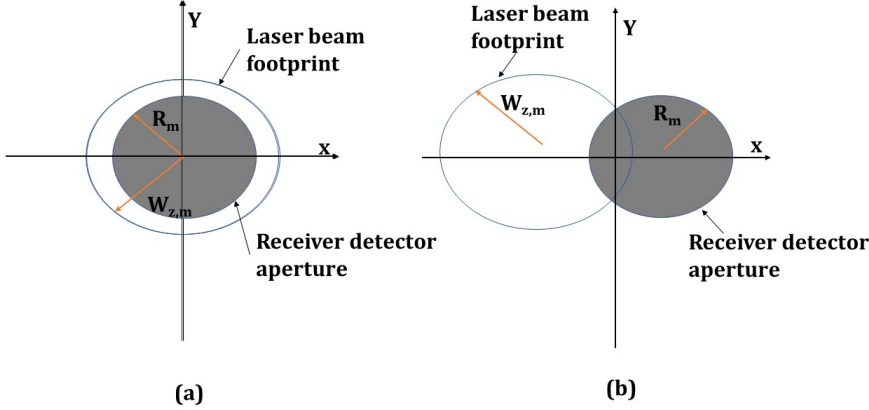


**Figure 2.2:** FSO Link (a) without Pointing error (b) with pointing error

In FSO, the optical beam is highly directional with an exceptionally narrow beam divergence. Additionally, FSO link receivers have a limited Field of View (FOV). Ensuring the continuous availability of the FSO link requires maintaining a consistent LOS connection between the transmitter and receiver. Nevertheless, the structures upon which FSO transceivers are mounted experience continuous motion due to various factors, including vibrations, high wind speeds, or thermal expansion. This dynamic environment can result in FSO link failure due to misalignment or building sway, posing a formidable challenge for transceiver alignment. Figure 2.2 (a) depicts the FSO link without pointing error. However, in Figure 2.2 (b), the alignment between the receiving laser beam footprint and the receiver aperture is imperfect, resulting in pointing error.

We consider a circular detection aperture characterized by its radius and Gaussian beam. The PDF for pointing error is expressed as follows:

$$f_{h_p}(h_p) = \frac{g^2}{A_0^{g^2}} h_p^{g^2-1}, \quad 0 \leq h_p \leq A_0 \quad (2.4)$$

Where  $A_0 = [\text{erf}(v)]^2$  represents the fraction of the power collected at  $r = 0$ .  $\text{erf}(\cdot)$  represents the gauss error function defined as  $\text{erf}(x) = \frac{2}{\sqrt{\pi}} \int_0^x e^{-t^2} dt$ . The parameter  $r$  represents the radial distance, while  $g$  signifies the ratio between the equivalent beam radius and the standard deviation of the pointing error displacement (jitter) at the receiver.

## 2.4 Mitigation techniques

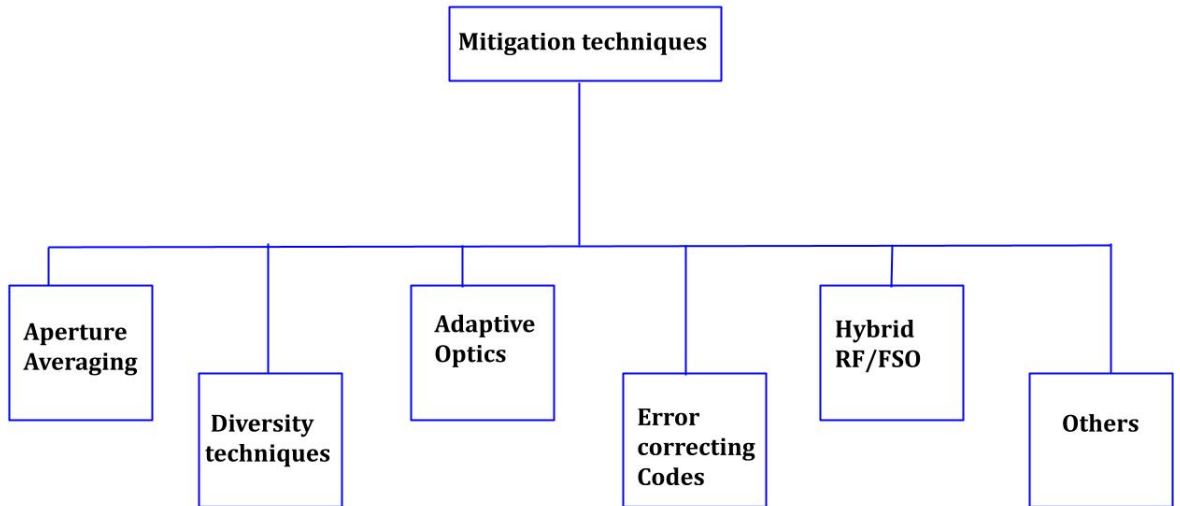


**Figure 2.3:** Different mitigation techniques

FSOC system performance is vulnerable to degradation caused by atmospheric factors such as absorption, scattering, and turbulence. Atmospheric turbulence causes fluctuations in irradiance and beam wander effects in the received signal, resulting in increased BER and deep signal fades, lasting from 1 to 100  $\mu$  sec [Lee and Chan (2004)]. For instance, at a 1 Gbps link rate, this could lead to the loss of up to  $10^5$  consecutive bits, introducing burst errors that degrade FSO link performance and reduce system availability. The outage performance of the system also deteriorates due to signal fading, especially in long-distance and mobile platform communications.

Hence, developing mitigation strategies for a dependable and robust FSO communication system is crucial. In Figure 2.3, various mitigation techniques are illustrated. In the following subsections, we'll explore a range of approaches designed to mitigate the signal fading induced by atmospheric turbulence in FSO systems.

### 2.4.1 Aperture Averaging

As the optical beam propagates, it undergoes natural divergence due to geometric attenuation, resulting in incomplete light collection at the receiver's termination point. To address this inherent limitation, the technique known as "aperture averaging" is employed, wherein the dimensions of the receiver's aperture are deliberately enlarged to encompass a more significant portion of the incoming optical beam [Soni and Malhotra (2011)]. This method represents a widely adopted strategy for mitigating signal fluctuations induced by the vagaries of atmospheric turbulence.

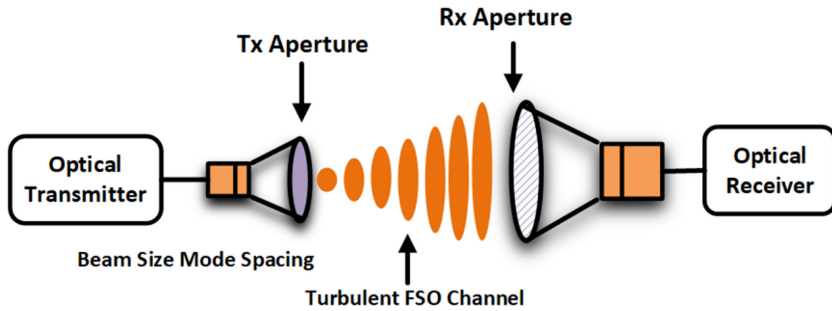


Figure 2.4: Aperture averaging of FSO transceiver [Jahid *et al.* (2022)]

The specific size of the aperture is determined by many factors, including the transmission distance and the prevailing conditions affecting signal quality. The deliberate expansion of the receiver aperture dimensions serves the dual purpose of reducing channel fading and the rapid fluctuations brought about by atmospheric eddies. It is imperative to underscore that with the augmentation of the receiver aperture size; there is a concomitant increase in background noise levels. Consequently, the judicious selection of an optimal aperture radius assumes paramount importance, as it significantly contributes to the enhanced power efficiency of the FSO link. This concept is visually depicted in Figure 2.4, illustrating aperture averaging within an FSO transceiver, where the dimensions of the receiver's aperture surpass those of the transmitter, thereby minimizing the detrimental effects of beam wandering.

## 2.4.2 Diversity techniques

Diversity techniques employed to mitigate the impact of atmospheric turbulence offer versatile solutions by operating within four distinct domains: time, frequency, space, and polarization. Instead of relying on a single large aperture, these approaches utilize an array of smaller receiver apertures, facilitating the transmission of multiple, mutually uncorrelated signal copies across these four domains. The adoption of diversity techniques is widely acknowledged for its capacity to reduce the necessity for active tracking during misalignment, ultimately enhancing BER performance while achieving the desired QoS.

Spatial diversity techniques involve multiple identical transmissions connecting source and receiver entities. This approach necessitates the deployment of an array of at least two transmitters and/or two receivers, each associated with mutually uncorrelated signal paths. To optimize the advantages conferred by spatial diversity, it is imperative that the separation between antennas, whether at the transmitter or receiver, equals or exceeds the coherence length of the atmosphere. This criterion ensures a high degree of independence or, at the very least, low correlation among the various paths. When these diverse paths exhibit low correlation, each path undergoes independent fading, which enhances the overall system performance. This enhancement is particularly pronounced in scenarios characterized by high turbulence levels, where the gains are substantial compared to situations featuring lower turbulence levels. FSO MIMO shares striking similarities with RF MIMO, resulting in a linearly scaled increase in channel capacity as additional transmitting antennas are incorporated.

Time diversity is used primarily in channels exhibiting time-selective fading, where repetitive symbols are transmitted across distinct coherence time intervals. When the length of the data frame exceeds the channel's coherence time, diversity can be introduced through coding or interleaving techniques. Investigations have shown that convolutional codes are well-suited for addressing the challenges of weak atmospheric turbulence. At the same time, Turbo-codes deliver substantial coding gains in the presence of strong turbulence conditions.

The laser signal undergoes polarisation splitting via a polarisation beam splitter (PBS) in the polarisation diversity. Subsequently, the same data signal is superimposed onto two orthogonal polarisation states. To maintain coherence within coherent optical receivers, careful alignment of the state of polarisation (SOP) of the local os-

cillator laser (LOL) with that of the received optical signal is imperative.

Within the domain of wavelength diversity, multiple copies of the same signal are transmitted across different wavelength channels. Given that the effects of turbulence arising from random refractive index variations exhibit variations across wavelengths, the resulting fading characteristics, including intensity fluctuations at the receiver, differ significantly among these wavelengths.

### 2.4.3 Adaptive optics

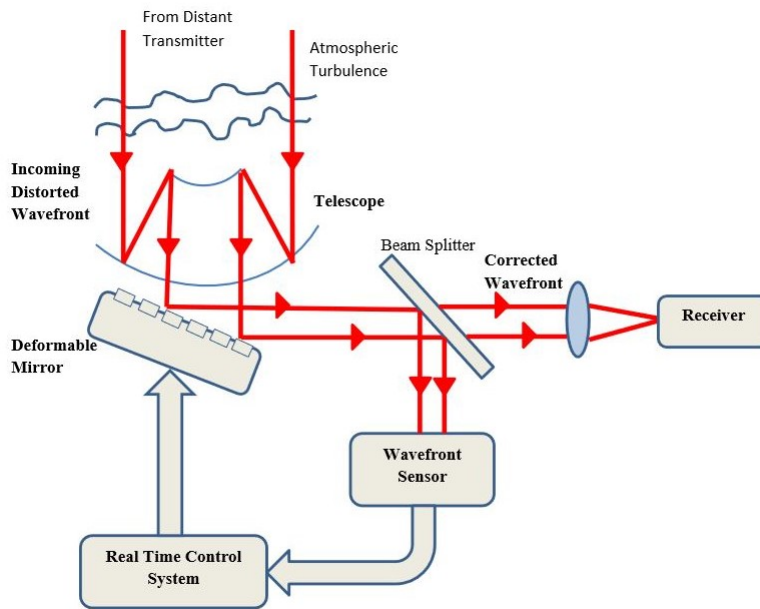


**Figure 2.5:** Visualization of conventional adaptive optics system. [Kaushal and Kad-doum (2016)]

Adaptive optics (AO) operates on the closed-loop control principle to counter the impact of atmospheric turbulence, facilitating the transmission of an undistorted optical beam through the atmosphere. While enhancing the FSO system’s performance can be achieved by increasing transmit power or employing diversity techniques, AO offers an avenue for further improving SNR while reducing the required transmit power. The AO system comprises critical components such as a wavefront sensor, wavefront corrector, and deformable mirrors, which can be situated at the transmitter or receiver optics to compensate for wavefront fluctuations. In this setup, a portion of the

received signal is directed to the wavefront sensor, generating a control signal for the wavefront corrector’s actuators, as illustrated in Figure 2.5. Nevertheless, implementing real-time wavefront control using traditional AO methods becomes challenging under highly turbulent conditions [Wilson *et al.* (1997)]. A non-conventional AO approach is considered in such scenarios, centred on optimizing received SNR or other pertinent performance metrics within the system [Vorontsov *et al.* (1997)].

#### 2.4.4 Error correcting Codes

Fluctuations in signal intensity resulting from atmospheric turbulence-induced channel fading can significantly deteriorate system performance. The atmospheric optical channel exhibits prolonged memory, causing extensive errors that impact consecutive received channel bits during channel fades. Error control coding methods enhance FSO link performance by employing various Forward Error Correction (FEC) schemes, including RS codes, BCH codes, turbo codes, convolutional codes, trellis-coded modulation (TCM) , and low-density parity-check (LDPC) codes. These codes introduce redundant information into the transmitted data, enabling the detection and correction of errors caused by channel fading at the receiver.

Earlier research on coded FSO systems has explored convolutional codes with binary modulation schemes like OOK in the atmospheric optical communication channel [Chan (1982)]. Turbo codes, TCM, or LDPC codes are preferable in scenarios characterized by strong atmospheric turbulence. Convolutional codes offer a suitable compromise between complexity and performance and can be effective across various turbulence conditions.

#### 2.4.5 Hybrid RF/FSO

Given the complementary aspects of radio and FSO communications, encompassing both capacity and coverage considerations, combining these mediums for data transmission offers substantial advantages over utilizing a single medium [Hou and O’Brien (2006)]. FSO links experience severe attenuation in foggy conditions. At the same time, RF frequencies encounter significant attenuation in rainy conditions, owing to the correlation between raindrop size and the wavelength of millimeter-wave transmissions (especially for frequencies exceeding 10 GHz) [Ghosh (2004)]. For instance, when an optical link operating at multi-gigabit per second speeds encounters an obstruction, a backup RF channel using hundreds of kilobits per second can provide continued connectivity [Juarez *et al.* (2006)]. Optical wireless links, known for their high data rates

relative to RF links, can be advantageous during brief periods requiring substantial throughput, especially in applications with lenient latency requirements [Muhammad *et al.* (2007)].

Incorporating hybrid RF/FSO systems enhances link reliability and facilitates load balancing across diverse scenarios [Torabi *et al.* (2022)]. RF systems extend coverage areas for end-users, addressing potential communication blockages. At the same time, FSO technology provides high data rates, allowing both to operate harmoniously in the same environment without causing interference.

## 2.4.6 Other Mitigation techniques

### 2.4.6.1 Pointing, Acquisition, and Tracking (PAT)

The deployment and operation of FSO links have necessitated the implementation of PAT schemes. A prominent characteristic of lasers is their capability to generate highly directional beams. FSO systems are meticulously engineered to maintain divergence of few milliradians, or even less, in order to focus optical energy precisely onto a designated receiver. These receivers feature a limited FOV in small angular degrees. This exceptionally narrow beam property imbues optical space links with reduced interference, heightened energy efficiency, and enhanced security. However, it concurrently renders establishing FSO links between two endpoints challenging. Furthermore, even following the successful establishment of a communication link, the availability of this link remains contingent upon various factors, including the impact of atmospheric turbulence, wind-induced effects, temperature loading on mounting equipment, and building sway, resulting in intermittent connectivity.

The pointing process initiates with identifying potential nodes within three-dimensional free space for establishing a connection, setting the stage for the subsequent connection procedure. In the acquisition mechanism, the focus pertains to signal modulation and detection techniques. Given the possibility of multiple optical beams intersecting a receiver aperture, it becomes imperative for the receiver to discern the desired signal warranting decoding. Simultaneously, tracking mechanisms are deployed to mitigate challenges arising from the narrow-beam characteristic. Even in scenarios involving stationary transceivers, the need for signal-tracking mechanisms remains pertinent; this stems from the stringent requirement of precise pointing accuracy within FSO links, where any optical beam misalignment can result in reduced available capacity and heightened outage probability.

#### 2.4.6.2 Background noise rejection

In the context of FSOC, the primary sources of background noise encompass (a) diffused extended noise originating from the atmosphere, (b) noise stemming from celestial bodies like the Sun and other point sources, and (c) light scattered and collected by the receiver. Integrating spatial filters alongside an adaptive modulation technique characterized by a high peak-to-average power ratio (PAPR) emerges as a viable solution to address these challenges. In this context, critical design parameters such as Doppler shift, signal arrival angles, and the spectral width of the laser source must be meticulously considered for spatial filter development. Within FSO links, M-PPM is a superior choice due to its enhanced energy efficiency and adeptness at substantially reducing background radiation noise.

#### 2.4.6.3 Reconfigurable Intelligent Surface (RIS)

Despite mitigation techniques, LOS connectivity remains a significant challenge for implementing FSO systems practically. Buildings, trees, or terrain features like hills can obstruct LOS links. In situations where a LOS link is unavailable, a potential solution involves deploying a relay node that possesses a clear LOS path to both the transmitter (Tx) and receiver (Rx) [Li *et al.* (2019)]. However, such a relay node must have either a partial or complete FSO transceiver chain. For instance, a decode-and-forward relay node necessitates components like a laser source (LS), lens, photodetector (PD), tracking system, and signal processing units, substantially increasing system complexity. To address this challenge, the concept of optical RIS has been proposed to relax the stringent LOS requirements of FSO systems. Unlike traditional relays, RIS offers energy and cost efficiency as they comprise passive elements and can be conveniently installed on existing infrastructure, such as building walls, as depicted in Figure 2.6 (a).

RIS consists of planar arrays featuring resonant sub-wavelength artificial structures capable of manipulating incident beams' wavefronts to achieve desired reflection directions. This manipulation of the beam's phase across the RIS surface results in the realization of the generalized Snell's law of reflection [Najafi *et al.* (2020)], as illustrated in Figure 2.6 (b).

The optical signal transmitted from the transmitter to the RIS is considered to be reflected from the surface of RIS and then received at the receiver, mathematically can

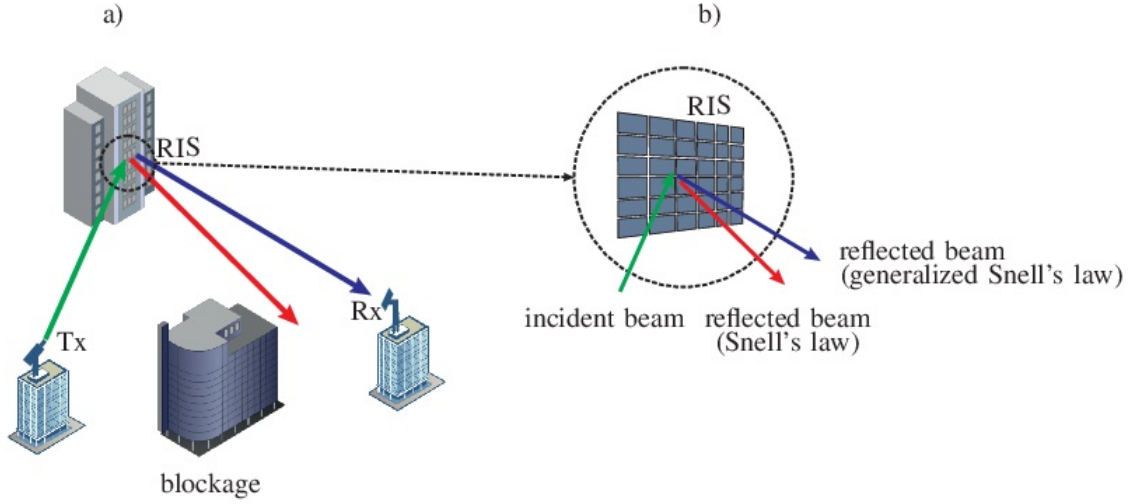


**Figure 2.6:** (a)RIS offer a solution for mitigating the stringent LOS constraints in FSO systems (b) RIS allows the redirection of optical beams as desired. [Najafi *et al.* (2021)]

be given as  $y = \sqrt{E_s}(h\mu e^{j\theta}g)x + n$ , where  $E_s$  denotes the symbol energy,  $h$  and  $g$  are complex channel vectors from transmitter to the RIS and from the RIS to the receiver, respectively,  $\mu$  and  $\theta$  are amplitude reflection coefficient, and phase introduced by the RIS module respectively. Here,  $x$  and  $y$  correspond to the transmitted and received symbols, respectively, and  $n$  is the additive white Gaussian noise.

## 2.5 Summary

Throughout this chapter, we have introduced the FSO channel in-depth, delving into its various influential factors, including atmospheric attenuation, atmospheric turbulence, and pointing errors. Our comprehensive discussion has encompassed a wide array of mitigation techniques strategically employed to counteract the detrimental impacts of these atmospheric phenomena and pointing errors in the performance of FSO systems. Additionally, we have extensively covered the concept of RIS, shedding light on its pivotal role in mitigating issues related to skip zones in FSO communication.

# Chapter 3

## ABER Performance Enhancement of RoFSO Communication System with MIMO configuration

### 3.1 Introduction

The rapid expansion of multimedia usage generates an unprecedented volume of data, necessitating high data rate wireless connectivity solutions. The advent of 5G communication promises to deliver numerous new services characterized by ultra-low latency, extensive device connectivity, enhanced security, reduced energy consumption, and exceptionally high quality of experience [Shafi *et al.* (2017)]. The RF spectrum, traditionally employed for communication, is becoming increasingly constrained due to the scarcity of available spectrum resources in wireless networks [Obeed *et al.* (2018)]. In response, RoFSO communication has emerged as a compelling option for achieving high data rate communication in areas where fiber optic cables have not been deployed or are not feasible. RoFSO technology offers data rates nearly on par with fiber optic cables, making it a viable alternative [Prabu *et al.* (2014)].

FSO technology, at the core of RoFSO communication, boasts essential features such as heightened security, immunity to electromagnetic interference, and superior energy efficiency [Arnon *et al.* (2012)]. FSO systems find applications in backhauling, last-mile access, and as a viable alternative to traditional fiber optics.

However, RoFSO faces limitations due to atmospheric effects like scattering, turbulence, and attenuation, all affecting performance. Pointing error significantly degrades signals [Arnon (2003)]. Atmospheric turbulence and adverse weather worsen RoFSO performance. Optical signals can be modulated using intensity, phase, and polarization parameters. DPSK modulation is preferred for its superior performance over

OOK and Phase Shift Keying (PSK) [Khare and Sahayam (2012)]. DPSK is favoured over BPSK due to its more straightforward implementation [Mishra and Giri (2018)].

Various mitigation techniques have been developed to address the challenges posed by atmospheric-induced fading, stemming from scattering and turbulence. These techniques include aperture averaging, diversity techniques, and error control coding [Yang *et al.* (2014)]. Diverse diversity techniques have been deployed to enhance the performance of FSO systems, encompassing wavelength diversity, temporal diversity, and spatial diversity [Tsiftsis *et al.* (2009)]. While the turbulence effect remains relatively consistent across the various wavelengths used in optical communication, temporal diversity is associated with extended processing times. Consequently, spatial diversity techniques have gained favour, permitting multiple receivers and transmitters.

### 3.1.1 Contributions

In this chapter, we propose various system configurations, encompassing SISO, SIMO, MISO, and MIMO. Additionally, we perform a comprehensive comparative analysis of two signal-combining methods: OC and EGC. Our turbulence modelling leverages the Malaga distribution, a versatile model proficient in capturing turbulence effects [Palliyembil *et al.* (2018)]. Furthermore, we incorporate pointing errors into our model, representing them through Beckmann and modified Rayleigh distributions [Ninos *et al.* (2019)]. Our research introduces novel closed-form expressions for the ABER under both combining schemes, employing the Meijer G function. We illustrate our findings using two- and three-dimensional graphical representations.

## 3.2 System model

As depicted in Figure 3.1, we present a fundamental block diagram illustrating the RoFSO link incorporating DPSK modulation. TT signifies the transmitting telescope in Figure 3.1, while RT designates the receiving telescope. One prominent feature of this RoFSO system is incorporating spatial diversity as a mitigation technique to lessen the detrimental impact of atmospheric conditions. In this context, spatial diversity entails strategically deploying multiple transmitters and receivers. In Figure 3.1, red pathways represent the optical signal transmission, while the black pathways symbolize the electrical signal flow within the system.

Figure 3.2 illustrates that the investigated RoFSO communication system incorporates spatial diversity at transmission and reception points. Specifically, this system employs  $M$  transmitters and  $N$  receivers strategically positioned at a separation dis-

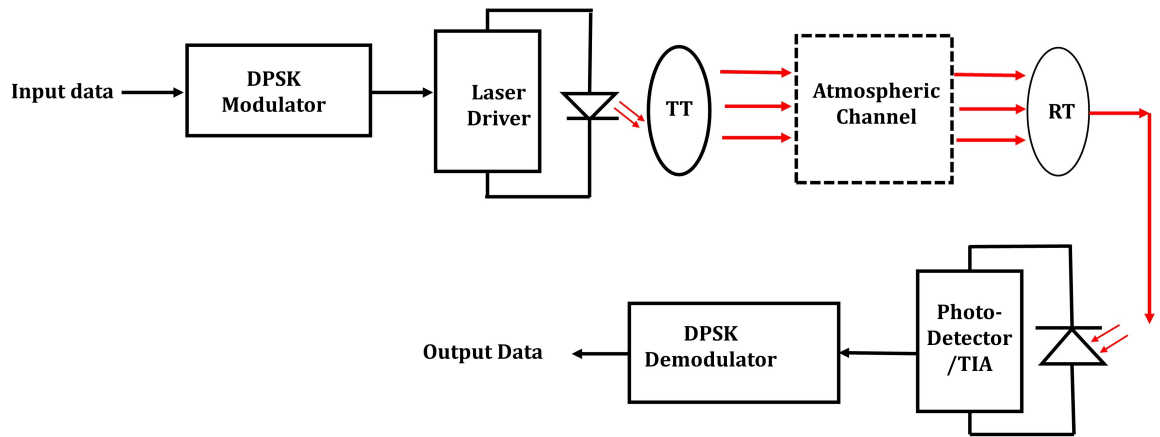


Figure 3.1: RoFSO system with DPSK modulation

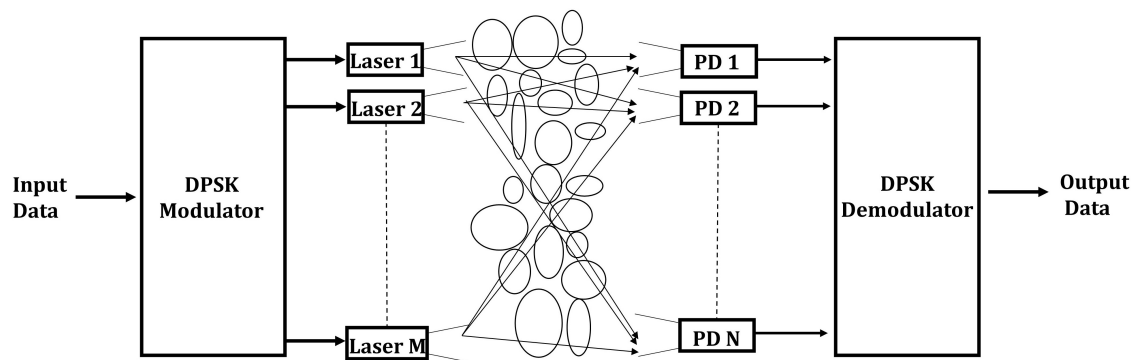


Figure 3.2: RoFSO system model with spatial diversity and MIMO configuration

tance that is notably greater than the atmospheric coherence length. This spatial arrangement ensures that the optical channels between the transmitters and receivers remain uncorrelated. Within the diagram, the component denoted as PD represents the photodetector. The RoFSO system configuration adopts an intensity modulation direct detection (IM/DD) approach. Furthermore, in the context of this RoFSO system, channel state information is available at both the transmitting and receiving ends.

The RoFSO channel under examination is characterized as a discrete-time ergodic channel, and it is subjected to additive white Gaussian noise. The transmitting data undergoes modulation within this channel using a DPSK subcarrier intensity modulation scheme.

At the receiving end of this RoFSO system, the electrical signal acquired from the  $n^{\text{th}}$  receiver can be mathematically described as follows [Prabu *et al.* (2014)]

$$r_n = xR \sum_{m=1}^M h_{mn} + v_n, \quad n = 1, 2, \dots, N \quad (3.1)$$

Here,  $x$  represents the electrical signal transmitted through the RoFSO channel.  $R$  stands for the photodetector sensitivity. The optical channel model, denoted by  $h_{mn}$ , represents the link between the  $m^{\text{th}}$  transmitter and the  $n^{\text{th}}$  receiver, and it encompasses various phenomena. These phenomena include the effects of fluctuation, attenuation due to atmospheric losses, turbulence-induced variations, and signal fading. Here,  $v_n$  represents the Additive White Gaussian Noise (AWGN) encountered at the  $n^{\text{th}}$  receiver. This noise source has a zero mean and a variance denoted by  $\sigma_v = N_0/2$ .

### 3.3 Channel Model

The optical channel model, denoted as  $h_{mn}$ , is pivotal in understanding the dynamics of the RoFSO communication system. It is a product of three distinct components, each contributing to the overall optical channel characteristics. This crucial relationship, as defined in [Farid and Hranilovic (2007)], is represented by Eq. (3.2)

$$h_{mn} = h_{l_{mn}} h_{s_{mn}} h_{p_{mn}} \quad (3.2)$$

Here  $h_{l_{mn}}$  models the signal attenuation due to path loss,  $h_{s_{mn}}$  models turbulence effects and  $h_{p_{mn}}$  models the pointing error in between  $m^{\text{th}}$  transmitter to  $n^{\text{th}}$  receiver.

**Table 3.1:** Different attenuation coefficients at 1550 nm [Kumar and Krishnan (2020b)]

Weather condition	Attenuation $\sigma$ (dB/KM)
Very clear air	0.0647
Haze	0.7360
Light fog	4.2850

The modelling of atmospheric loss within the RoFSO system plays a pivotal role in characterizing the signal’s behaviour as it traverses through the Earth’s atmosphere. Beer-Lambert’s law rigorously describes this phenomenon, a fundamental concept well-documented in [Wang *et al.* (2016)]. The relationship governing atmospheric loss, denoted as  $h_{l_{mn}}$ , is expressed as follows:

$$h_{l_{mn}} = \exp(-\sigma L) \quad (3.3)$$

In this Eq. (3.3),  $L$  symbolizes the link length, the physical distance the optical signal travels. The parameter  $\sigma$  is the attenuation coefficient, and its value is contingent on the prevailing weather conditions and the specific wavelength of the optical signal. This study focuses on an optical signal with a wavelength of 1550 nm, a common choice in optical communication systems. Of notable significance is the variance in  $\sigma$  corresponding to different weather conditions, as shown in Table 3.1.

For this investigation, a specific link length of 1 km has been considered, representing real-world scenarios. The utilization of this standard link length enables the study to draw valuable insights into the implications of atmospheric loss on RoFSO communication for practical applications.

In this work, the atmospheric turbulence in the RoFSO channel has been modelled by M distribution. In this model at the receiver, there are three components: first is LOS contribution  $U_L$ , second is the quasi-forward scattered component, which is coupled to LOS contributions  $U_S^C$  and last one  $U_S^G$ , is scattered energy due to off-axis eddies [Jurado-Navas *et al.* (2012a)] as shown in Figure 3.3. The  $U_L$  component has the power  $\Omega$ ,  $U_S^C$  component has the power  $2\rho b_0$  and  $U_S^G$  component have the power  $2(1 - \rho)b_0$ . Here, the symbol  $\rho$  symbolizes the power coupling between the Line of Sight (LOS) and scattered components. When  $\rho$  equals 0, it signifies minimal coupling, while increasing the value of  $\rho$  up to 1 reflects a scenario of maximum coupling.

For the M-distribution turbulence the PDF of the irradiance  $h_{s_{mn}}$  is given by [Wang

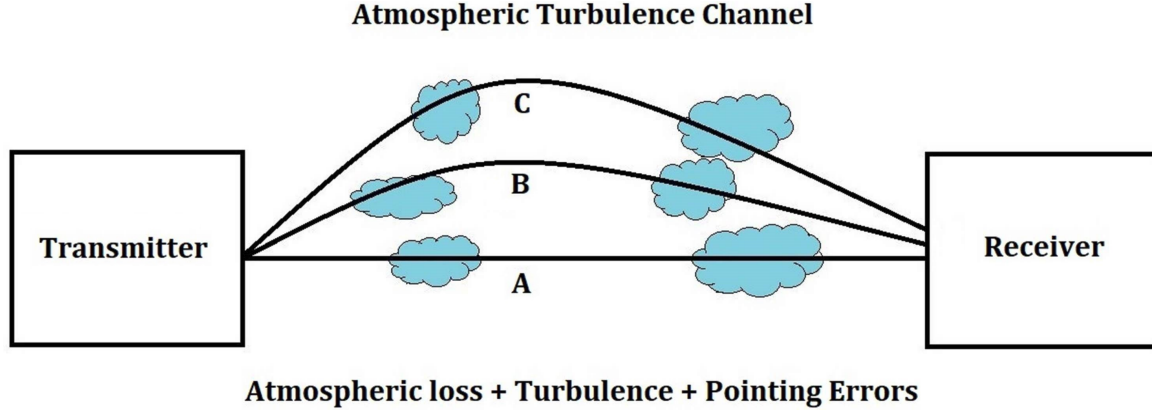


**Figure 3.3:** Optical beam propagation in M distribution model.

*et al.* (2016)]

$$f_{h_{s_{mn}}}(h_{s_{mn}}) = A_{mn} \sum_{k=1}^{\beta_{mn}} a_{k_{mn}} h_{s_{mn}}^{\frac{\alpha_{mn}+k}{2}-1} K_{\alpha_{mn}-k} \left( 2\sqrt{\frac{\alpha_{mn}\beta_{mn}h_{s_{mn}}}{\gamma'\beta_{mn} + \Omega}} \right) \quad (3.4)$$

where

$$A_{mn} = \frac{2\alpha_{mn}^{\frac{\alpha_{mn}}{2}}}{\gamma'^{1+\frac{\alpha_{mn}}{2}} \Gamma(\alpha_{mn})} \left( \frac{\gamma'\beta_{mn}}{\gamma'\beta_{mn} + \Omega'} \right)^{\beta_{mn} + \frac{\alpha_{mn}}{2}}$$

$$a_{k_{mn}} = \binom{\beta_{mn}-1}{k-1} \frac{(\gamma'\beta_{mn} + \Omega')^{1-\frac{k}{2}}}{k-1!} \left( \frac{\Omega'}{\gamma'} \right)^{k-1} \left( \frac{\alpha_{mn}}{\beta_{mn}} \right)^{\frac{k}{2}}$$

and  $\gamma' = 2(1 - \rho)b_0$

Here, the representation of large-scale turbulent eddies employs the parameter  $\alpha_{mn}$ , characterized as a positive value. Small-scale turbulent eddies are defined by the parameter  $\beta_{mn}$  as a natural number. The probability density function (pdf) described above offers a closed-form solution due to the natural number status of  $\beta_{mn}$  [Jurado-Navas *et al.* (2011a)]. It's worth noting that considering  $\beta_{mn}$  as a real number for a generalized expression with an infinite summation is not deemed acceptable due to the high degree of freedom [Jurado-Navas *et al.* (2012a)]. The function  $K_v(\cdot)$  refers to the second kind of modified Bessel function of order  $v$ . The total power received by the coherent contributions is denoted as  $\Omega' = \Omega + 2\rho b_0 + 2\sqrt{2b_0\Omega\rho} \cos(\phi_A - \phi_B)$ . In this equation,  $\phi_A$  represents the phase of the Line of Sight (LOS) component, while  $\phi_B$  signifies the phase of components coupled to LOS scattering. The phase difference between  $\phi_A$  and  $\phi_B$  is set to  $90^\circ$ .

In addition to atmospheric turbulence, the RoFSO link contends with pointing errors stemming from various factors like wind loads, building sway, minor seismic activity, and thermal expansion [Farid and Hranilovic (2007)]. Integrating the MIMO technique can enhance the performance of the RoFSO communication system significantly. However, it's crucial to acknowledge that pointing errors greatly influence the system's overall performance, thus warranting a comprehensive investigation. To model these pointing errors, Beckmann and Rayleigh distribution has been employed. The PDF of this distribution is expressed as [Krishnan *et al.* (2018)].

$$f_{h_{pmn}} = \frac{g^2}{A_0^{g^2}} (h_{pmn})^{g^2} \quad \text{for } 0 \leq h_p \leq A_0 \quad (3.5)$$

The parameter  $A_0$ , which represents a portion of the total received optical power, can be defined as  $A_0 = [\text{erf}(\nu)]^2$ . Here  $\nu$  is given as  $\nu = \sqrt{\frac{\pi}{2}} \frac{a}{w_z}$ , where  $a$  signifies the radius of the receiver, and  $w_z$  denotes the beam width of the transmitted optical signal at a distance  $L$ . The variable  $g$  is introduced as the ratio between the effective beam width, denoted as  $w_{zeq}$ , and the standard deviation of jitter symbolized as  $\sigma_s$  and is expressed as  $g = \frac{w_{zeq}}{2\sigma_s}$ .

The overall channel model for  $h_{mn}$  is given as [Wang *et al.* (2016)]

$$f_{h_{mn}}(h_{mn}) = \int f_{h_{mn}/h_{smn}}(h_{mn}/h_{smn}) f_{h_{smn}}(h_{smn}) dh_{smn} \quad (3.6)$$

Here  $f_{h_{mn}/h_{smn}}(h_{mn}/h_{smn})$  is conditional probability for considered turbulence state  $h_{smn}$ . It is given as

$$\begin{aligned} f_{h_{mn}/h_{smn}}(h_{mn}/h_{smn}) &= \frac{1}{h_{smn} h_{l_{mn}}} f_{h_{pmn}} \left( \frac{h_{mn}}{h_{smn} h_{l_{mn}}} \right) \\ &= \frac{g^2}{A_0^{g^2} h_{smn} h_{l_{mn}}} \left( \frac{h_{mn}}{h_{smn} h_{l_{mn}}} \right)^{g^2-1} \end{aligned} \quad (3.7)$$

$$\text{for } 0 \leq h_{mn} \leq A_0 h_{smn} h_{l_{mn}}$$

By substituting Eqns. (3.4) and (3.7) in Eq. (3.6) we have

$$\begin{aligned}
f_{h_{mn}}(h_{mn}) &= \frac{g^2 A_{mn}}{(A_0 h_{l_{mn}})^{g^2}} (h_{mn})^{g^2-1} \times \\
&\sum_{k=1}^{\beta} a_{k_{mn}} \int_{h_{mn}/h_{l_{mn}} A_0}^{\infty} h_{s_{mn}}^{\frac{\alpha_{mn}+k}{2}-1-g^2} \\
&K_{\alpha_{mn}-k} \left( 2 \sqrt{\frac{\alpha_{mn} \beta_{mn} h_{s_{mn}}}{\gamma' \beta_{mn} + \Omega}} \right) dh_{s_{mn}}
\end{aligned} \tag{3.8}$$

Overall channel model  $f_{h_{mn}}(h_{mn})$  obtained finally as below [Wang *et al.* (2016)]

$$\begin{aligned}
f_{h_{mn}}(h_{mn}) &= \frac{g^2 A_{mn} h_{mn}^{-1}}{2} \sum_{k=1}^{\beta_{mn}} \left( a_{k_{mn}} B_{mn}^{\frac{\alpha_{mn}+k}{2}} \right) \\
&G_{1,3}^{3,0} \left( \frac{h_{mn}}{B_{mn} A_0 h_{l_{mn}}} \middle| \begin{matrix} 1+g^2 \\ g^2, \alpha_{mn}, k \end{matrix} \right)
\end{aligned} \tag{3.9}$$

where  $B_{mn} = \frac{\Omega' + \gamma'_{mn} \beta}{\alpha_{mn} \beta_{mn}}$  and  $G_{p,q}^{m,n}[\cdot]$  is the meijer G function.

### 3.4 Analysis of SISO RoFSO system

DPSK-based SIM RoFSO system has been considered, whose probability of conditional BER is expressed as following [Prabu *et al.* (2014)]

$$P_{ec,SISO}(h) = \frac{1}{2} \exp\left(-\frac{1}{2} SNR\right) = \frac{1}{2} \exp\left(-\frac{R^2 A^2 h^2}{4\sigma^2}\right) \tag{3.10}$$

Where  $\sigma^2$  is the variance of channel noise, A is the peak amplitude of the transmitted signal, and R is the photodetector responsivity. The ABER,  $P_e$  for considered RoFSO system over atmospheric turbulence channel, is given by [Prabu *et al.* (2014)]

$$P_{e,SISO} = \int_0^{\infty} P_{ec,SISO}(h) f_h(h) dh \tag{3.11}$$

For the SISO channel model calculation,  $m=n=1$  has to be taken. By using Eqs. (3.9) and (3.10) in Eq. (3.11) the ABER is calculated as

$$P_{e,SISO} = \frac{g^2 A}{2} \sum_{k=1}^{\beta} a_k B^{\frac{\alpha+k}{2}} \int_0^{\infty} 0.5 \exp\left(-\frac{R^2 A^2 h^2}{4\sigma^2}\right) h^{-1} G_{1,3}^{3,0}\left(\frac{h}{BA_0 h_l} \middle| 1+g^2, \alpha, k\right) dh \quad (3.12)$$

An exponential function in the above Eq. (3.12) can be transformed into Meijer G function [Adamchik and Marichev (1990) Eq. (11)]. By using [Adamchik and Marichev (1990) Eq.(21)] the ABER of DPSK-SIM can be obtained as

$$P_{e,SISO} = \frac{g^2 A}{4} \sum_{k=1}^{\beta} a_k B^{\frac{\alpha+k}{2}} \frac{2\alpha + k - 2}{2\pi} G_{6,3}^{1,6}\left(z \middle| \eta, \chi\right) \quad (3.13)$$

Where,  $z = SNR_{av} \times 8B^2 A_0^2 h_l^2$

$$\eta = \frac{1-g^2}{2}, \frac{2-g^2}{2}, \frac{1-\alpha^2}{2}, \frac{2-\alpha^2}{2}, \frac{1-k}{2}, \frac{2-k}{2}$$

$$\chi = 0, \frac{-g^2}{2}, \frac{1-g^2}{2}$$

### 3.5 Analysis of MIMO RoFSO system

The ABER for MIMO RoFSO link is given as [Tsiftsis *et al.* (2009)]

$$P_{e,MIMO} = \int_0^{\infty} f_h(h) \frac{1}{2} \exp\left(-\frac{R^2 A^2}{4\sigma^2} \sum_{n=1}^N \left(\sum_{m=1}^M h_{MN}\right)^2\right) dh \quad (3.14)$$

where  $f_h(h)$  is the joint PDF of vector  $h = (h_{11}, h_{12}, \dots, h_{MN})$  of length MN By using Eq. (3.9) in Eq. (3.14) we obtained the ABER as

$$\begin{aligned}
P_{e,MIMO} &= \frac{g^2 A_{mn}}{2} \sum_{k=1}^{\beta_{mn}} \left[ a_{k_{mn}} B_{mn}^{\frac{\alpha_{mn}+k}{2}} \right. \\
&\quad \int_0^\infty 0.5 \exp\left(-\frac{R^2 A_{mn}^2}{4\sigma^2} \sum_{n=1}^N \left(\sum_{m=1}^M h_{mn}\right)^2\right) h_{mn}^{-1} \\
&\quad \left. G_{1,3}^{3,0}\left(\frac{h_{mn}}{BA_0 h_l} \middle| 1+g^2\right) \right] \quad (3.15)
\end{aligned}$$

The exponential function is expressed in Meijer G function [Adamchik and Marichev (1990), Eq.(11)], and used [Adamchik and Marichev (1990), Eq. (21)] to get closed form expression of ABER of DPSK-SIM MIMO RoFSO System.

$$\begin{aligned}
P_{e,MIMO} &= \prod_{n=1}^N \prod_{m=1}^M \frac{g_{mn}^2 A_{mn}}{4} \sum_{k=1}^{\beta_{mn}} a_{k_{mn}} B_{mn}^{\frac{\alpha_{mn}+k}{2}} \\
&\quad \frac{2^{\alpha_{mn}+k}-2}{2\pi} G_{6,3}^{1,6}\left(z \middle| \eta\right) \quad (3.16) \\
&\quad \chi
\end{aligned}$$

Where,  $z = SNR_{av} \times 8B_{mn}^2 A_0^2 h_{l_{mn}}^2$

$$\begin{aligned}
\eta &= \frac{1-g_{mn}^2}{2}, \frac{2-g_{mn}^2}{2}, \frac{1-\alpha_{mn}^2}{2}, \frac{2-\alpha_{mn}^2}{2}, \frac{1-k}{2}, \frac{2-k}{2} \\
\chi &= 0, \frac{-g_{mn}^2}{2}, \frac{1-g_{mn}^2}{2}
\end{aligned}$$

## 3.6 Different Combining Techniques

### 3.6.1 Optimal Combining

Optimal combining assigns appropriate weights to signals received from multiple diversity branches based on their respective signal strengths, ensuring that these signals are aligned in phase before being combined. This technique maximizes the overall received signal quality by mitigating the impact of noise and interference. The conditional BER of the proposed RoFSO system with Optimal Combining is given as [Prabu *et al.* (2014)]

$$P_{e,OC}(h) = Q\left(\frac{RA}{\sqrt{2N}\sigma^2} \sqrt{\sum_{n=1}^N h_n^2}\right) \quad (3.17)$$

The ABER of SIMO RoFSO with OC diversity at the receiver can be written as

$$P_{e,OC} = \int_0^\infty Q \left( \frac{RA}{\sqrt{2N\sigma^2}} \sqrt{\sum_{n=1}^N h_n^2} \right) f_h(h) dh \quad (3.18)$$

In the integral of the Eq. (3.18) we have approximated Q function as in [Chiani *et al.* (2003) Eq.(14)]

$$\begin{aligned} P_{e,OC} &\approx \frac{1}{12} \prod_{n=1}^N \int_0^\infty e^{-\left(\frac{R^2 A^2 h_n^2}{4N\sigma^2}\right)} f_{h_n}(h_n) dh_n \\ &\quad + \frac{1}{4} \prod_{n=1}^N \int_0^\infty e^{-\left(\frac{R^2 A^2 h_n^2}{3N\sigma^2}\right)} f_{h_n}(h_n) dh_n \end{aligned} \quad (3.19)$$

By using Eq.(3.9) in the above expression (3.19) and transforming the exponential function as Meijer G function [Adamchik and Marichev (1990) Eq.(11)], the ABER of DPSK-SIM can be calculated using [Adamchik and Marichev (1990) Eq.(21)]as

$$\begin{aligned} P_{e,OC} &\approx \frac{1}{12} \prod_{n=1}^N \frac{g_n^2 A_n}{2} \sum_{k=1}^{\beta_n} a_{k_n} B_n^{\frac{\alpha_n+k}{2}} \frac{2^{\alpha_n+k-2}}{2\pi} G_{6,3}^{1,6} \left( z \middle| \eta \right) \\ &\quad + \frac{1}{4} \prod_{n=1}^N \frac{g_n^2 A_n}{2} \sum_{k=1}^{\beta_n} a_{k_n} B_n^{\frac{\alpha_n+k}{2}} \frac{2^{\alpha_n+k-2}}{2\pi} \\ &\quad G_{6,3}^{1,6} \left( \frac{31}{6} z \middle| \eta \right) \end{aligned} \quad (3.20)$$

Where,  $z = SNR_{av} \times 8B_n^2 A_0^2 h_{t_n}^2$

$$\begin{aligned} \eta &= \frac{1-g_n^2}{2}, \frac{2-g_n^2}{2}, \frac{1-\alpha_n^2}{2}, \frac{2-\alpha_n^2}{2}, \frac{1-k}{2}, \frac{2-k}{2} \\ \chi &= 0, \frac{-g_n^2}{2}, \frac{1-g_n^2}{2} \end{aligned}$$

### 3.6.2 Equal Gain Combining

In the EGC diversity combining technique, N number of photodetectors output is combined and demodulated. For the considered RoFSO system with EGC, the probability of conditional BER is expressed as Prabu *et al.* (2014)

$$P_{e_c,EGC}(h) = \frac{1}{2} \text{erfc} \left( \sqrt{\frac{R^2 A^2}{4N\sigma^2} \sum_{n=1}^N h_n^2} \right) \quad (3.21)$$

The ABER of the SIMO RoFSO system, which is using EGC combining technique, can be calculated from Eq. (3.11) as

$$P_{e,EGC} = \frac{1}{2} \int_0^\infty \text{erfc} \left( \sqrt{\frac{R^2 A^2}{4N\sigma^2} \sum_{n=1}^N h_n^2} \right) f_h(h) dh \quad (3.22)$$

Integral in the Eq. (3.22) has been evaluated by expressing complementary error function as Meijer G function [Brychkov *et al.* (1986)(8.4.14.2)] and using [Adamchik and Marichev (1990), Eq. (21)]

$$P_{e,EGC} = \frac{1}{2\sqrt{\pi}} \prod_{n=1}^N \frac{g_n^2 A_n}{2} \sum_{k=1}^{\beta_n} a_{k_n} B_n^{\frac{\alpha_n+k}{2}} \frac{2^{\alpha_n+k-2}}{2\pi} G_{7,4}^{2,6} \left( \nu \middle| \begin{matrix} \tau \\ \psi \end{matrix} \right) \quad (3.23)$$

Where,  $\nu = SNR_{av} \times 8B_n^2 A_0^2 h_{l_n}^2$   
 $\tau = \frac{1-g_n^2}{2}, \frac{2-g_n^2}{2}, \frac{1-\alpha_n^2}{2}, \frac{2-\alpha_n^2}{2}, \frac{1-k}{2}, \frac{2-k}{2}, 1$   
 $\psi = 0, \frac{1-g_n^2}{2}, \frac{1-g_n^2}{2}$

### 3.7 Results and Discussion

This section provides an analysis based on the ABER expressions derived. These results shed light on how various parameters impact the performance of the MIMO system under consideration. In our numerical assessment, specific values have been employed for multiple RoFSO parameters, including a photodetector responsivity of 0.5 A/W, a jitter standard deviation of  $\sigma_s = 30$  cm, and a beam radius of  $\Omega_l = 2.5$  m at a distance of 1 km. For this research, we have selected the 1550 nm optical wavelength.

In Figure 3.4, the plot illustrates the relationship between average SNR and ABER for various scenarios, including SISO, MIMO, and different spatial diversity combining techniques at the receiver. In this case, the channel modelling assumes strong turbulence with  $\rho = 0.7$ . The analysis considers a scenario with N=4 for utilising both EGC and OC combining techniques. The observations from Figure 3.4 highlight several key findings. Firstly, the system's performance exhibits enhancement with the increased number of receiving apertures and the application of different combining techniques.

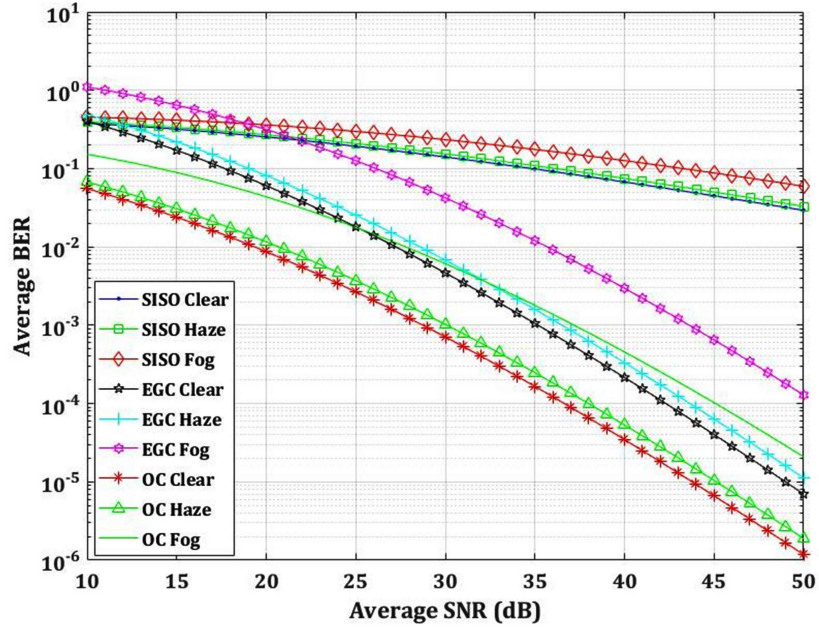


**Figure 3.4:** Average BER versus Average SNR for SISO and SIMO having EGC and OC combining techniques with different weather conditions (Strong turbulence,  $\rho = 0.7$ ,  $g = 4.167$ ).

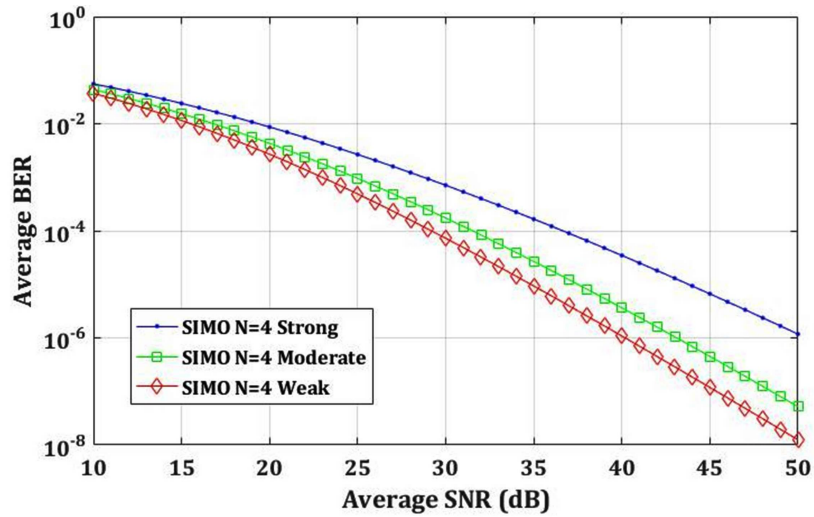


**Figure 3.5:** Average BER against Average SNR for SIMO OC with different turbulence conditions (Very clear air weather condition,  $\rho = 0.7$ ,  $g = 4.167$ ).

Furthermore, it's evident that adverse atmospheric conditions, such as fog, substantially negatively impact the RoFSO system's performance. Lastly, comparing the two combining methods, OC and EGC, reveals that OC outperforms EGC in this context.

For plotting Figure 3.5, we assumed ideal weather conditions with very clear air,

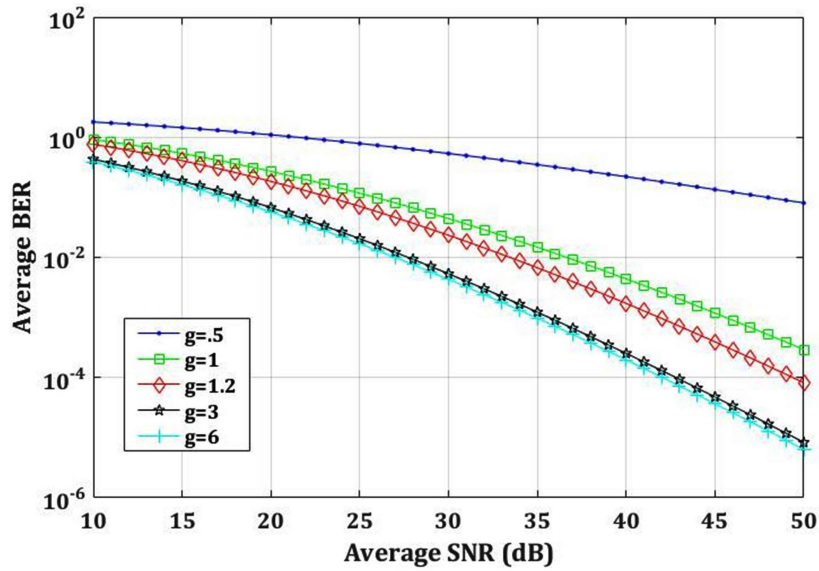


**Figure 3.6:** Average BER against Average SNR for SIMO OC with different pointing error conditions (Very clear air weather condition and strong turbulence).

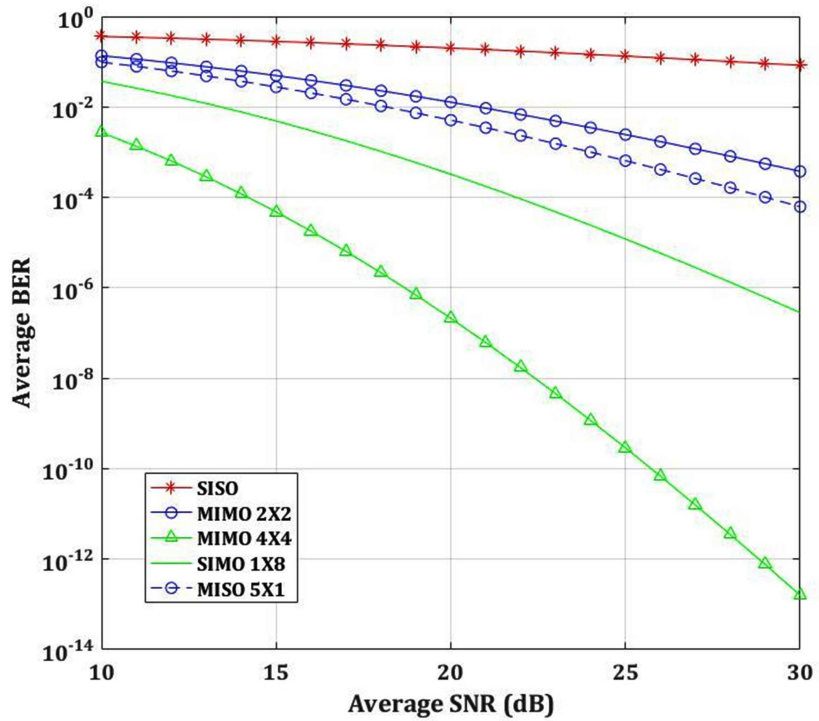


**Figure 3.7:** Average BER against Average SNR for SIMO OC with different diversity schemes (Very clear air weather condition and weak turbulence).

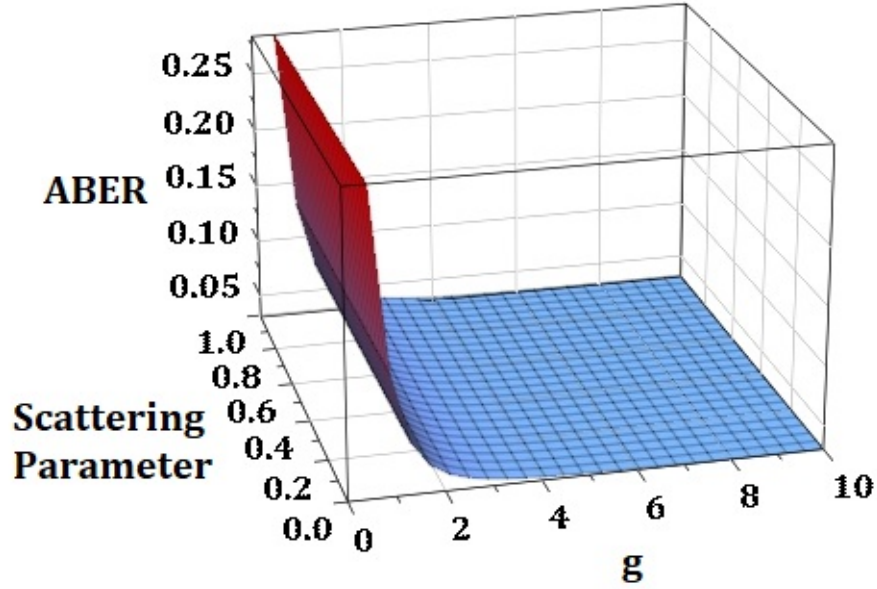


**Figure 3.8:** 3D Plot for ABER variation(z-axis) with scattering parameter ( $\rho$ ) (y-axis) and g variation(x-axis) (Very clear air weather condition and strong turbulence).

and a scattering parameter of  $\rho = 0.7$  was considered. The findings in Figure 3.5 underscore the substantial impact of atmospheric turbulence strength on the system's performance. Specifically, it's evident that achieving an ABER of  $10^{-4}$  necessitates different SNR under varying turbulence conditions, such as 29 dB SNR required to attain this ABER in weak turbulence. In comparison, moderate turbulence calls for 31 dB SNR, and strong turbulence necessitates a 37 dB SNR.

In Figure 3.6, we have depicted the system's performance under very clear air weather and strong turbulence (with a scattering parameter  $\rho = 0.7$ ). This visualisation allows us to observe how changes in the pointing error parameter, denoted as "g," influence system performance. Notably, g is inversely related to the jitter standard deviation, meaning that as we increase the g value, the impact of pointing errors decreases, resulting in improved system performance.

Specific conditions were considered for the computations leading to Figure 3.7, including very clear air weather, weak turbulence, and  $\rho = 0.7$ . Figure 3.7 illustrates the sensitivity of the system's performance to variations in the number of transmitters and receivers. A noteworthy observation is that to maximise the performance of the RoFSO system, both the number of transmitters and receivers should increase simultaneously.

In the context of strong turbulence conditions, a 3D plot in Figure 3.8 explores the relationship between the ABER, the pointing error parameter ( $g$ ), and the scattering parameter ( $\rho$ ). The plot elucidates that when  $\rho = 0$ , scattering is at its maximum, and as the value of  $\rho$  increases, scattering decreases, reaching a minimum at  $\rho = 1$ . Regarding the pointing error parameter ( $g$ ), it becomes evident that as the value of  $g$  increases, the detrimental effects of pointing errors diminish.

### 3.8 Summary

We have tabulated one of the results in Table 3.2, showing that at different weather conditions, the required average SNR for maintaining  $10^{-4}$  ABER differs for various configurations. MIMO with OC combined performs better than other configurations in all three weather conditions.

Performance Metrics.	SISO	MIMO with OC	MIMO with EGC
$10^{-4}$ ABER (Clear)	>50 dB	37 dB	42 dB
$10^{-4}$ ABER (Haze)	>50 dB	38 dB	43 dB
$10^{-4}$ ABER (FOG)	>50 dB	45 dB	50 dB

**Table 3.2:** ABER performance comparison at different weather conditions

This research work comprehensively analysed the ABER performance of a DPSK-based RoFSO system. We explored various system configurations, including SISO, SIMO, MISO, and MIMO. We employed OC and EGC techniques to enhance the system’s performance. Our investigation encompassed a range of environmental conditions, including different weather scenarios, turbulence levels, scattering effects, and pointing error conditions. The results from our extensive analysis indicate that the 4x4 MIMO configuration consistently outperforms other configurations. Specifically, it achieves an impressive level of performance with a requirement of 25 dB average SNR to attain an ABER of  $10^{-9}$ .

# Chapter 4

## RoFSO communication system's performance enhancement with BCH and RS error correcting codes

### 4.1 Introduction

One of the most critical research areas in wireless communication is RoFSO communication. It offers an enormous data rate (100Mb/s-10Gb/s) of communication over shorter ranges (few Kms) [Chadha (2013)]. Other features include license-free spectrum, large bandwidth, electromagnetic interference immunity, and less power requirement [Arnon *et al.* (2015)]. Remote sensing, deep space networking, backhaul for wireless cellular networks, and disaster recovery are all major RoFSO applications. The research has recently focused on utilizing the RoFSO link as a resort for the last-mile problem, especially in urban and semi-urban areas.

The message signal is transmitted via the atmosphere in the RoFSO communication system. Thus, it led to different types of distortions in the optical signal. There are broadly three adverse effects on the RoFSO Communication system: attenuation, scintillation, and scattering. Atmospheric attenuation mainly depends on the weather conditions. The scintillation effect is also known as turbulence-induced fading. Variation of pressure and temperature happens randomly in the atmosphere, so air masses known as turbulent eddies are formed. The optical beam that passes through the atmosphere comes in contact with these air masses, and random fluctuations are introduced to it; this phenomenon is called the scintillation effect, which degrades the system to a large extent [Ghassemlooy and Popoola (2010)]. Another aggravating factor is pointing error, which occurs when the transmitter and receiver in the system

are misaligned.

The atmospheric turbulence effect has been defined using a variety of statistical models, including Lognormal, Negative exponential, GammaGamma [Ghassemlooy *et al.* (2019)], K-distribution, and M-distribution [Kashani *et al.* (2015)]. We have considered the M-distribution for atmospheric turbulence modelling in this work.

Different mitigation methods, such as diversity, relay, multiple input multiple output, aperture averaging, modulation techniques, and error-correcting codes, are used to mitigate atmospheric turbulence and pointing error [Kaushal *et al.* (2017)].

### 4.1.1 Contribution

Our research focused on the OFDM-based RoFSO communication system. This system employs BPSK modulation, bolstered by incorporating Error-Correcting Codes to enhance performance. The core of our investigation revolved around comparing the ABER performance of two distinct coding strategies: the BCH code and the RS code, both of which were applied to RoFSO communication links. To comprehensively assess the impact of these coding techniques, we contrasted their performance against that of uncoded RoFSO links, thus providing valuable insights into the role of coding in mitigating the challenges posed by diverse environmental conditions encompassing weather variations, turbulence effects, scattering phenomena, and pointing errors. This multifaceted analysis allows us to draw informed conclusions about the efficacy of BCH and RS coding under various operational scenarios, offering a deeper understanding of their respective benefits in RoFSO communication.

## 4.2 System Model

OFDM is a multicarrier modulation scheme that breaks large data streams into smaller ones and transmits them synchronously over narrowband subcarriers in the OFDM-FSO communication system. OFDM leverages various baseband modulation schemes, such as QPSK, BPSK, and QAM, to name a few, and operates at high frequencies. In our investigation, we opted for integrating BPSK modulation with the OFDM-based RoFSO communication system, while enhancing the system's robustness by incorporating coding techniques. Figure 4.1 shows the system model block diagram. In this figure, RoFSO transmitter optics include Laser diode, Mach-Zehnder modulator for electrical to optical (E/O) conversion, and transmit aperture. RoFSO receiver optics include receiving aperture and photodetector. We have considered the BCH and RS codes as error-correcting codes for RoFSO communication. After

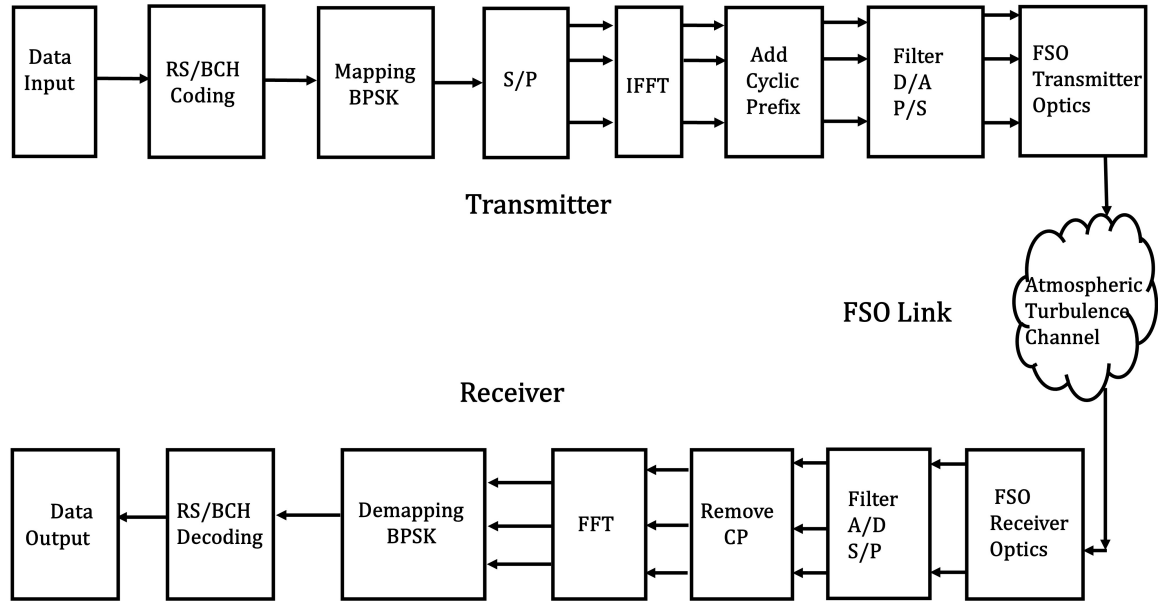


**Figure 4.1:** RoFSO link with Bpsk modulation and RS/BCH coding

conversion at the transmitter, the OFDM signal can be expressed as [Wang *et al.* (2015)].

$$S_{OFDM}(t) = \sum_{j=0}^{N-1} X_j e^{i(w_n + 2\pi f_c)t} \quad (4.1)$$

Here,  $w_n$  denotes the frequency of the OFDM signal, with  $N$  representing the total count of subcarriers. Meanwhile,  $f_c$  signifies the carrier frequency, and  $X_j$  represents the complex data symbol in the transmission process. The duration of the OFDM signal is defined by  $T$ .

The M-distributed RoFSO channel serves as the conduit for the OFDM signal, denoted as  $S_{OFDM}$ . Given the transmission through free space, the optical signal experiences attenuation and encounters additional noise inherent to its traversal through the medium. The received power is given as [Bekkali *et al.* (2010)] Eq. (4.2) at the receiving end.

$$P_r(t) = P_t(t)I + n(t) \quad (4.2)$$

Here,  $I$  denotes the channel attenuation due to path loss, atmospheric turbulence, and misalignment fading.  $n(t)$  is the AWGN.

The instantaneous CNDR for a specific OFDM subcarrier is measured at the receiver's output as follows. [Bekkali *et al.* (2010)],

$$CNDR_n(I) = \frac{(m_n \rho P_0 I)^2}{2(N_0/T + \sigma_{n,IMD}^2)} \quad (4.3)$$

Here  $m_n$  represents the optical modulation index for each OFDM subcarrier, and  $\rho$  is the photodetector responsivity.

Considering the Inter-Modulation Distortion (IMD) noise as Gaussian distributed [Bekkali *et al.* (2010)] then Eq.(4.3) can be expressed as

$$CNDR_n(I) \approx \frac{m_n^2 \rho^2 P_0^2 I^2}{2[(N_0/T)_{AV} + (\sigma_{n,IMD}^2)_{AV}]} \quad (4.4)$$

Here the AV stands for the average value. From Eq. (4.4) the expected value of  $CNDR_n$  can be expressed as

$$CNDR_n(I) \approx \frac{m_n^2 \rho^2 P_0^2 (E[I])^2}{2[(N_0/T)_{AV} + (\sigma_{n,IMD}^2)_{AV}]} \quad (4.5)$$

Here  $E[I]$  is the expected value of  $I$ .

### 4.3 Channel Model

We have considered the overall channel  $I$ , which includes the atmospheric path loss  $I_l$ , atmospheric turbulence  $I_a$ , and pointing error  $I_p$ .

The overall channel model  $I$  is given by [Wang *et al.* (2016)]

$$I = I_l I_a I_p \quad (4.6)$$

Beer-Lambert's law [Wang *et al.* (2016)] is used to model Atmospheric loss, and it is given by

$$I_l = \exp(-\sigma L) \quad (4.7)$$

$L$  is the link length, and  $\sigma$  represents the attenuation coefficient.  $\sigma$  takes different values depending on weather conditions and optical wavelength. We've used a 1550 nm wavelength optical signal in this work. Table 3.1 shows the various attenuation coefficient values for different weather conditions. The length of the link is considered to be 1 km.

In this work, atmospheric turbulence in the RoFSO channel is considered M-

distributed. According to this model at the receiver, there are three components: LOS contribution  $U_L$ , coupled to LOS contributions quasi-forward scattered component  $U_S^C$ , and scattered energy due to off-axis eddies  $U_S^G$  [Jurado-Navas *et al.* (2012a)]. The power of components  $U_L$ ,  $U_S^C$  and  $U_S^G$  are  $\Omega$ ,  $2\rho b_0$  and  $2(1 - \rho)b_0$  respectively. Here,  $\rho$  represents the power coupling between the scattered and LOS components. At  $\rho = 0$ , the power coupling is minimum, and at  $\rho = 1$ , it is maximum.

For the M-distribution turbulence model, the PDF of the irradiance  $I_a$  is given by [Wang *et al.* (2016)]

$$f_{I_a}(I_a) = A \sum_{k=1}^b a_k I_a^{\frac{\alpha+k}{2}-1} K_{\alpha-k} \left( 2\sqrt{\frac{\alpha\beta I_a}{\gamma'\beta + \Omega'}} \right) \quad (4.8)$$

where

$$A = \frac{2\alpha^{\frac{\alpha}{2}}}{\gamma'^{1+\frac{\alpha}{2}}\Gamma(\alpha)} \left( \frac{\gamma'\beta}{\gamma'\beta + \Omega'} \right)^{\beta+\frac{\alpha}{2}}$$

$$a_k = \binom{\beta-1}{k-1} \frac{(\gamma'\beta + \Omega')^{1-\frac{k}{2}}}{k-1!} \left( \frac{\Omega'}{\gamma'} \right)^{k-1} \left( \frac{\alpha}{\beta} \right)^{\frac{k}{2}}$$

and  $\gamma' = 2(1 - \rho)b_0$

Here,  $\alpha$  is a scattering process positive parameter associated with the effective number of large-scale cells.  $\beta$  is a natural number, allowing PDF to follow the actual observed data, resulting in a closed-form representation [Jurado-Navas *et al.* (2011a)].

The parameter  $\Omega' = \Omega + 2\rho b_0 + 2\sqrt{2b_0\Omega\rho} \cos(\phi_A - \phi_B)$ , which is the average power from the coherent contributions.  $\phi_A$  represents the phase of the LOS component, and  $\phi_B$  represents the phase of coupled-to-LOS scatter components. The difference between  $\phi_A$  and  $\phi_B$  has been considered to be  $90^\circ$ .

RoFSO is a LOS communication; as a result, the transmitter and receiver must be aligned. The performance of the RoFSO communication system is strongly affected by this alignment. Building sway, thermal expansion, and wind loads are some of the reasons for the misalignment between transmitter and receiver in this system [Farid and Hranilovic (2007), Sandalidis *et al.* (2009)]. Beckmann and Rayleigh's distributions have been used to model the pointing errors. For pointing error, the irradiance PDF distribution is given as [Krishnan *et al.* (2018)]

$$f_{I_p} = \frac{g^2}{A_0^{g^2}} I_p^{g^2}, \quad \text{for } 0 \leq I_p \leq A_0 \quad (4.9)$$

Where  $A_0 = [erf(\nu)]^2$  is the fraction of total received optical power.  $\nu$  is given by,  $\nu = \sqrt{\frac{\pi}{2}} \frac{a}{w_z}$ . Here,  $a$  is the radius of the receiver aperture. We have considered the receiver aperture diameter of 10 cm and the transmitter aperture diameter of 8 cm. The transmitted optical signal has a beam width of  $w_z$  at the distance  $L$ .

Effective beam width at the receiver is given by

$$w_{zeq} = \left[ \frac{\sqrt{\pi} erf(\nu) w_z^2}{2\nu e^{-\nu^2}} \right]^{\frac{1}{2}} \quad (4.10)$$

Here  $g = \frac{w_{zeq}}{2\sigma}$  is the ratio between the effective beam width and the jitter standard deviation  $\sigma$ .

The overall channel model for I is given as [Wang *et al.* (2016)]

$$f_I(I) = \int f_{I/I_a}(I/I_a) f_{I_a}(I_a) dI_a \quad (4.11)$$

Here  $f_{I/I_a}(I/I_a)$  is conditional probability for considered turbulence state  $I_a$ . It is given as

$$\begin{aligned} f_{I/I_a}(I/I_a) &= \frac{1}{I_a I_l} f_{I_p} \left( \frac{I}{I_a I_l} \right) \\ &= \frac{g^2}{A_0^{g^2} I_a I_l} \left( \frac{I}{I_a I_l} \right)^{g^2-1} \end{aligned} \quad (4.12)$$

$$\text{for } 0 \leq I \leq A_0 I_a I_l$$

By substituting Eqs. (4.8) and (4.12) in Eq. (4.11) we have

$$\begin{aligned} f_I(I) &= \frac{g^2 A}{(A_0 I_l)^{g^2}} (I)^{g^2-1} \times \\ &\sum_{k=1}^b a_k \int_{I/I_l A_0}^{\infty} I_a^{\frac{\alpha+k}{2}-1-g^2} \\ &K_{\alpha-k} \left( 2\sqrt{\frac{\alpha\beta I_a}{\gamma'\beta + \Omega}} \right) dI_a \end{aligned} \quad (4.13)$$

Overall channel model  $f_I(I)$  obtained as below [Wang *et al.* (2016)]

$$f_I(I) = \frac{g^2 AI^{-1}}{2} \sum_{k=1}^{\beta} \left( a_k B^{\frac{\alpha+k}{2}} \right) G_{1,3}^{3,0} \left( \frac{I}{BA_0 I_l} \middle| 1 + g^2, g^2, \alpha, k \right) \quad (4.14)$$

where  $B = \frac{\Omega + \gamma' \beta}{\alpha \beta}$  and  $G_{p,q}^{m,n}[\cdot]$  is meijer G function

## 4.4 BCH Code

BCH codes are classified as binary cyclic error-correcting codes formulated within the Galois field (GF) mathematical domain. These codes are capable of rectifying multiple bits afflicted by errors, as corroborated in [Ding (2015)].

It is a linear block code that increases the signal's redundancy. In this case,  $k$  information bits are converted into an  $n$ -bit code word with  $n-k$  redundant bits. The code rate (R), given by  $k/n$ , defines redundancy. We used a code rate of less than one-third in our work. We used the BCH code  $n = 31$ ,  $k = 11$ . These BCH codes are error-correcting codes with  $t$  bits. These codes have a bit length of  $n = 2^m - 1$  in the GF ( $2^m$ ), where  $m$  is a positive integer ( $m \geq 3$ ). The field components are represented by  $\{0, 1, \alpha, \alpha^2, \dots, \alpha^{2^m-2}\}$ . Here  $\alpha$  is the basic element in the field GF( $2^m$ ) [Lin and Costello (2001), MacWilliams and Sloane (1977)]. There are different conjugacy classes in which these elements are segregated. A minimal polynomial is associated with every conjugacy class. A BCH code's generator polynomial is realized by finding the least common multiple of the minimal polynomials associated with the elements  $\alpha^b, \alpha^{b+1}, \dots, \alpha^{b+\delta-2}$ , where  $b$  is an integer  $\geq 1$ , and  $\delta$  is design distance, which equals  $2t+1$ . The generator polynomial is computed as follows,

$$g(x) = LCM \{M_b(x), M_{b+1}(x), \dots, M_{b+\delta-2}(x)\} \quad (4.15)$$

Here  $M_i(x)$  represents the minimal polynomial of the  $i^{th}$  conjugacy class. Components of a particular conjugacy class have the same minimal polynomial. Various conjugacy classes consist of different minimal polynomials, presented in Table 4.1 [Ramavath *et al.* (2020a)]. By computing the product of the minimal polynomial, we get

**Table 4.1:** Minimal Polynomial of  $\text{GF}(2^5)$  for  $t = 4$  [Ramavath *et al.* (2020a)]

Conjugacy Class	Minimal Polynomial
$\{\alpha, \alpha^2, \alpha^4, \alpha^8, \alpha^{16}\}$	$M_1(x) = 1 + x^2 + x^5$
$\{\alpha^3, \alpha^6, \alpha^{12}, \alpha^{24}, \alpha^{17}\}$	$M_3(x) = 1 + x^2 + x^3 + x^4 + x^5$
$\{\alpha^5, \alpha^{10}, \alpha^{20}, \alpha^9, \alpha^{18}\}$	$M_1(x) = 1 + x + x^2 + x^4 + x^5$
$\{\alpha^7, \alpha^{14}, \alpha^{28}, \alpha^{25}, \alpha^{19}\}$	$M_1(x) = 1 + x + x^2 + x^3 + x^5$

the generator polynomial as

$$g(x) = 1 + x^2 + x^4 + x^6 + x^7 + x^9 + x^{10} + x^{13} + x^{17} + x^{18} + x^{20} \quad (4.16)$$

Using the generator polynomial  $g(x)$ , the generator matrix ( $G_{11 \times 31}$ ) is estimated. The operation  $c_{1 \times 31} = s_{1 \times 11} G_{11 \times 31}$  is used to encrypt the data. This BCH-encoded data is modulated with an optical signal before being sent through the atmosphere.

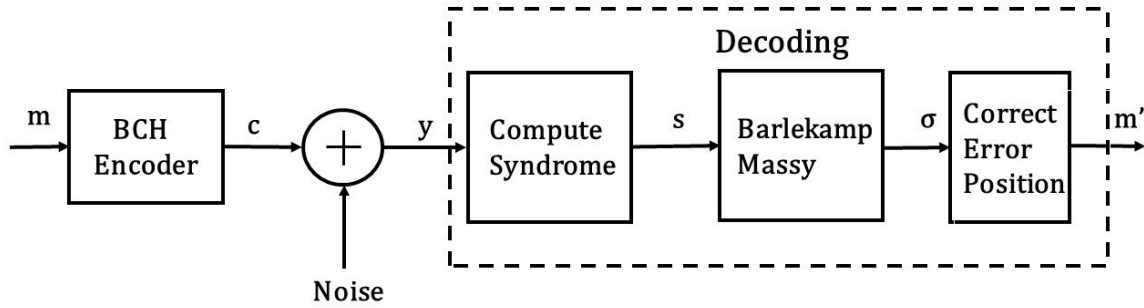


**Figure 4.2:** Block diagram of BCH encoder/decoder

The BCH encoder/decoder is shown in Figure 4.2. The message bits are encoded using the BCH encoder and sent via the RoFSO channel as  $m$ . The BCH decoder receives the received message bits  $y$  and evaluates them as  $m'$ . As shown in Figure 4.2 [Gupta *et al.* (2019)], there are three steps involved in decoding BCH code. The syndrome is computed first, and then the error position polynomial from the syndrome polynomial is developed using the Berlekamp-Massey algorithm. We get the error locations by finding the roots of the error location polynomial. After correcting the errors, an estimated information word is generated [Ding (2015)].

## 4.5 RS Code

The RS code exhibits exceptional burst error-correction capabilities, as confirmed in previous research [Ramavath *et al.* (2020b)]. In the context of FSO, occasional encounters with burst errors have been documented [Zhang *et al.* (2017)]. Therefore, the utilization of RS error-correcting codes has been proposed to enhance the reliability and robustness of information transmission in such scenarios.

The generator polynomial of an RS code with a length of 'n' over the Galois Field GF(q), possessing error-correcting capabilities for 't' symbols, is mathematically defined as  $g(x) = (x - \alpha^b)(x - \alpha^{b+1})\dots(x - \alpha^{b+\delta-2})$ . In this expression,  $\alpha$  represents a primitive element of the GF( $P^m$ ), 'b' is any real positive integer with  $b \geq 0$ , and  $\delta$  is defined as  $\delta = 2t + 1$ . The code-word of length 'n' can be represented as a polynomial, denoted as  $c(x) = c_0 + c_1x + c_2x^2 + \dots + c_{n-1}x^{n-1}$ , and this polynomial maintains a one-to-one correspondence with the message polynomial  $s(x) = s_0 + s_1x + s_2x^2 + \dots + s_{k-1}x^{k-1}$ .

This study employed RS codes with n=63 and k=51 over the GF( $2^6$ ) field for error detection and correction. Every symbol within the polynomial code word was transformed into six tuples of binary bits, subsequently transmitted through the FSO channel. The received bits were converted into 6-bit characters within the GF( $2^6$ ) field. To pinpoint the locations of any errors introduced, we harnessed the Berlekamp-Massey and Chien algorithm. To determine the magnitudes of these errors, we utilized Forney's algorithm.

## 4.6 Analytical ABER Evaluation

The ABER for the BPSK OFDM RoFSO system is given as [Kaur *et al.* (2014)]

$$ABER = \int_0^{\infty} P_I(I) f_I(I) dI \quad (4.17)$$

Conditional BER for BPSK OFDM system is given by [Selvi and Murugesan (2012)]

$$P_I(I) = \frac{1}{2} \operatorname{erfc} \left( \sqrt{\frac{E_b}{N_0}} \right) \quad (4.18)$$

Eq. (4.18) can be approximated as [Ajewole *et al.* (2019)]

$$P_I(I) = \frac{N^{-1}}{\log_a(2)} \sum_{j=0}^{N-1} \text{erfc} \left( \sqrt{CNDR_j(I)} \sin \left( \frac{\pi}{2} \right) \right) \quad (4.19)$$

Here  $N$  is the number of subcarriers,  $CNDR_j$  is the carrier to noise plus distortion ratio, and  $E_b/N_0$  is the bit energy to noise ratio. After substituting Eq. (4.14) and Eq. (4.19) in Eq. (4.17), we get ABER as

$$\begin{aligned} ABER &= \frac{N^{-1}}{\log_a(2)} \sum_{j=0}^{N-1} \int_0^\infty \left[ \text{erfc} \left( \sqrt{CNDR_j(I)} \right) \right] \times \\ &\quad \frac{g^2 A}{2} \sum_{k=1}^{\beta} I^{-1} \left( a_k B^{\frac{\alpha+k}{2}} \right) \times \\ &\quad G_{1,3}^{3,0} \left( \frac{I}{BA_0 I_l} \middle| 1+g^2 \right) dI \end{aligned} \quad (4.20)$$

In Eq. (4.20), replace the  $\text{erfc}(\cdot)$  with the suitable Meijer G function as given in [Ajewole *et al.* (2019)]. After solving finally, we get ABER as

$$ABER = \frac{N^{-1}}{\log_a(2)} \sum_{j=0}^{N-1} \frac{1}{\sqrt{\pi}} \frac{g^2 A}{2} \sum_{k=1}^{\beta} \left( a_k B^{\frac{\alpha+k}{2}} \right) Z \quad (4.21)$$

Where

$$Z = G_{4,3}^{2,3} \left( \sqrt{CNDR_j} BA_0 I_l \middle| 1-g^2, 1-\alpha, 1-k, 1 \right)_{0, 1/2, -g^2}$$

#### 4.6.1 ABER Evaluation for BCH Coded RoFSO system

The upper bound on the probability of decoding error  $p_d$  with a  $(n,k,t)$  BCH code over  $\text{GF}(2^m)$  having  $t$  symbol error correcting capability is given by [Ramavath *et al.* (2020a)].

$$P_d \leq \sum_{i=t+1}^n \binom{n}{i} P^i (1-P)^{n-i} \quad (4.22)$$

Where  $n$  is the block length, and  $P$  is the binary symmetric channel transition probability.

#### 4.6.2 ABER Evaluation for RS Coded RoFSO system

An error occurs when the decoded code word differs from the transmitted code word. The probability of error for the RS code is given by [Ramavath *et al.* (2020b)]

$$P_d \leq \sum_{i=t+1}^n \binom{n}{i} P_s^i (1 - P_s)^{n-i} \quad (4.23)$$

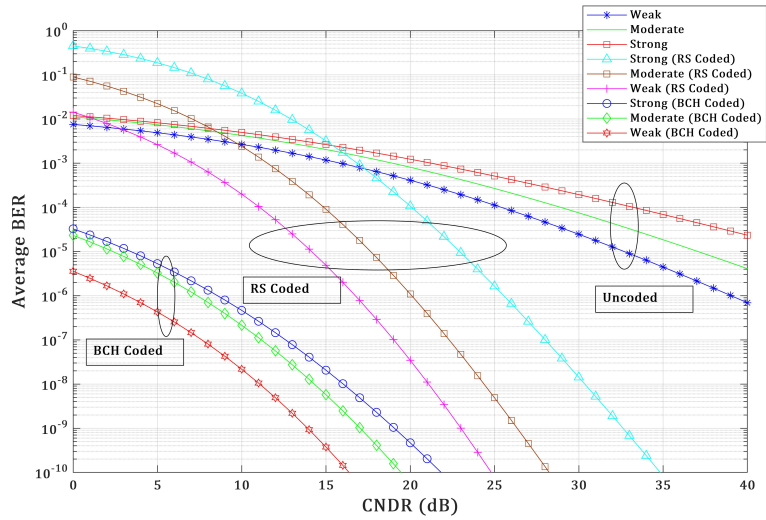
Here  $P_d$  is the upper bound BER associated with non-binary RS code, and  $t$  is the symbol error correcting capability.  $P_s$  is symbol error probability and code rate  $r=k/n$ .

### 4.7 Result and Discussion

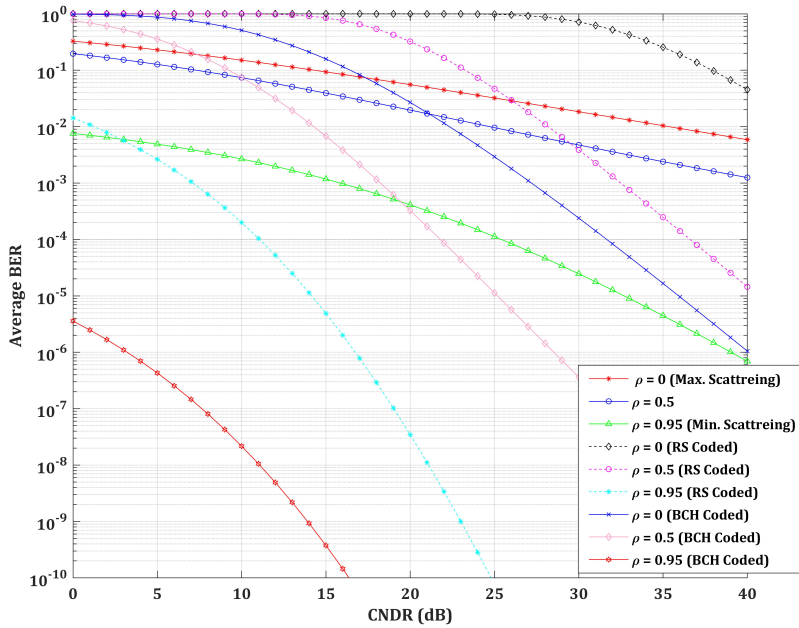
This section presents the analytical ABER results for the OFDM RoFSO system as a function of the CNDR. The optical signal operates at a wavelength of  $1.55 \mu\text{m}$ , and the receiver's aperture radius is 5 cm. Various values of the refractive index structure parameter ( $C_n^2$ ) are considered to account for different turbulence conditions. Specifically, for weak turbulence,  $C_n^2$  is assigned a value of  $2 \times 10^{-14} m^{-2/3}$ , for moderate turbulence, it's set to  $4 \times 10^{-14} m^{-2/3}$ , and for strong turbulence, it's adjusted to  $8 \times 10^{-14} m^{-2/3}$  [Ninos *et al.* (2019)]. Misalignment scenarios are also incorporated, as detailed in [Kumar and Krishnan (2020a)]. For this research, we have selected the 1550 nm optical wavelength.

Figure 4.3 compares ABER performance among three RoFSO systems: uncoded, BCH-coded, and RS-coded, under varying turbulence conditions. A very clear air environment was assumed when generating Figure 4.3 data. Across all turbulence conditions, the superiority of the BCH-coded RoFSO system is evident. To achieve a ABER of  $10^{-6}$ , the BCH-coded system demands less than 5 dB CNDR in weak turbulence. In contrast, the uncoded system necessitates over 35 dB CNDR, and the RS-coded system calls for nearly 17 dB CNDR. As Figure 4.3 illustrates, the RS-coded RoFSO system outperforms the uncoded system in the case of weak turbulence. However, in scenarios characterized by strong turbulence, the RS-coded system exhibits inferior performance compared to the uncoded system.

Figure 4.4 provides a detailed analysis of the ABER performance in different scat-



**Figure 4.3:** Average BER performance comparison of BCH and RS coded with uncoded OFDM ROFSO communication with different turbulence conditions.



**Figure 4.4:** Average BER performance comparison of BCH and RS coded with uncoded OFDM ROFSO communication with different scattering conditions (different  $\rho$  values).

tering conditions for uncoded, BCH-coded, and RS-coded RoFSO systems. It's important to note that when creating the data for Figure 4.4, we considered scenarios involving very clear air and weak turbulence. The results are enlightening; they showcase the superior performance of the BCH-coded RoFSO system compared to the uncoded and RS-coded systems in conditions characterized by moderate ( $\rho = 0.5$ ) and minimal scattering ( $\rho = 0.95$ ). However, in conditions with the maximum scattering ( $\rho = 0$ ), the BCH-coded RoFSO system's performance lags behind the uncoded system when the CNDR is less than 15 dB. Nonetheless, for CNDR values exceeding 15 dB, the BCH-coded system outperforms the uncoded one. An intriguing observation from Figure 4.4 is that under moderate scattering ( $\rho = 0.5$ ) and maximum scattering ( $\rho = 0$ ) conditions, the RS-coded RoFSO system exhibits inferior performance when compared to the uncoded system. Remarkably, the RS-coded system only outperforms the uncoded system under conditions of minimal scattering ( $\rho = 0.95$ ).

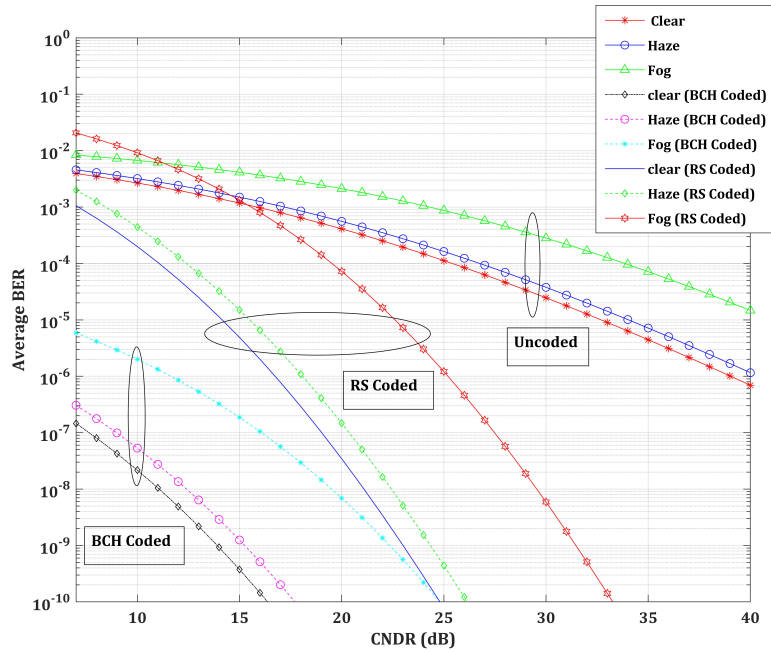


**Figure 4.5:** Average BER performance comparison of BCH and RS coded with uncoded OFDM ROFSO communication with different weather conditions

Figure 4.5 comprehensively analyses the ABER performance under various weather conditions for uncoded, BCH-coded, and RS-coded RoFSO systems. Notably, we specifically considered weak turbulence for the data presented in Figure 4.5. The results highlight the superior performance of the BCH-coded RoFSO system compared

to the uncoded and RS-coded systems across all three weather conditions. To attain ABER of  $10^{-6}$  in foggy weather, the BCH-coded RoFSO system necessitates a CNDR of approximately 12 dB, while the uncoded system mandates more than 40 dB CNDR, and the RS-coded system requires 25 dB CNDR. The findings from Figure 4.5 conclude that the RS-coded RoFSO system outperforms the uncoded system under clear and hazy weather conditions. Specifically, the RS-coded system surpasses the uncoded one for foggy weather conditions when the CNDR exceeds 12 dB.

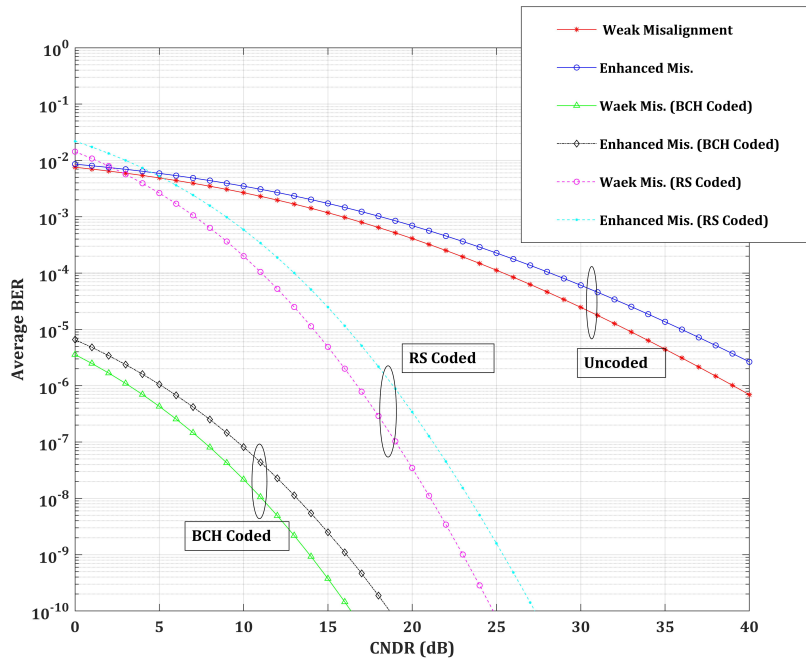


**Figure 4.6:** Average BER performance comparison of BCH and RS coded with uncoded OFDM ROFSO communication with different pointing errors.

Figure 4.6 compares ABER performance among uncoded, BCH-coded, and RS-coded RoFSO systems under two distinct Pointing error conditions: weak and enhanced misalignment. This analysis was conducted within weak turbulence and clear air weather conditions. In Figure 4.6, it's worth noting that 'weak misalignment' denotes instances of minor pointing errors, while 'enhanced misalignment' signifies significant and pronounced pointing errors. The outcomes presented in Figure 4.5 unequivocally reveal the superior performance of the BCH-coded RoFSO system in contrast to the uncoded and RS-coded systems for both weak and enhanced misalignment scenarios. The BCH-coded RoFSO system attains a ABER of  $10^{-7}$  for enhanced misalignment with a CNDR of approximately 9 dB. In contrast, it accomplishes the

same ABER with about 7.5 dB CNDR for weak misalignment. This signifies that achieving an equivalent ABER performance demands an additional 2.5 dB of power for enhanced misalignment conditions.

## 4.8 Summary

We have tabulated one of the results in Table 4.2, showing that at different atmospheric turbulence conditions, the required CNDR for maintaining  $10^{-6}$  ABER differs for various configurations. BCH coded system performs better than other configurations in all three turbulence conditions.

Performance Metrics	Uncoded	RS Coded	BCH Coded
$10^{-6}$ ABER (Weak)	39 dB	17 dB	3 dB
$10^{-6}$ ABER (Moderate)	>40 dB	20 dB	7 dB
$10^{-6}$ ABER (Strong)	>40 dB	26 dB	9 dB

**Table 4.2:** ABER performance comparison at different turbulence conditions

In this study, we conducted an in-depth examination of the ABER performance within a BPSK RoFSO system, integrating two distinct coding techniques: BCH and RS. Our endeavour culminated in deriving a novel ABER expression formulated as a closed-form equation employing the Meijer-G function. Under weak turbulence conditions, the advantages of using BCH coding became evident. Achieving ABER of  $10^{-6}$  mandated a minimal CNDR of less than 5 dB in the BCH-coded RoFSO system. In contrast, the RS-coded system necessitated 17 dB CNDR to reach the same ABER level. The uncoded RoFSO system demanded a substantially higher CNDR of over 35 dB to achieve a comparable ABER.

Conversely, it was apparent that BCH coding held a significant advantage in scenarios characterised by enhanced misalignment. To attain a ABER of  $10^{-7}$ , the BCH-coded RoFSO system required a modest 9 dB CNDR. In stark contrast, the RS-coded system had a substantially higher requirement of 19 dB CNDR to reach this ABER level. In contrast, the uncoded system demanded a notably elevated CNDR, exceeding 40 dB. Our analysis establishes BCH coding as the superior choice for the BPSK OFDM-based RoFSO system. It is imperative to underscore that our comparative evaluation encompassed a broad spectrum of weather and turbulence conditions.



# Chapter 5

## RIS-aided RoFSO communication system for mitigating skip zone problem

### 5.1 Introduction

RoFSO represents a LOS communication method tailored for high data rates, ensuring secure transmission between optical transmitters and receivers. The RoFSO domain has garnered considerable attention due to its distinct advantages over traditional RF communication, especially within point-to-point network configurations. Critical benefits of RoFSO encompass its substantial bandwidth, augmented channel capacity, and cost-effectiveness, underpinned by the unlicensed status of optical wavelengths [Ansari *et al.* (2015)]. This unique attribute alleviates the bandwidth constraints associated with RF technology. The applications of RoFSO are manifold, spanning from facilitating high-bandwidth access to optical fiber networks to enabling satellite-to-satellite communication and last-mile connectivity [Khalighi and Uysal (2014)]. Given the extensive interest within the RoFSO realm, many research endeavours have enriched the literature. For instance, [Pati and Krishnan (2019)] introduces an analytical model tailored for transmitting PSK modulated signals using OFDM over FSO links. [Singh and Malhotra (2020)] offers a comparative analysis of the performance of 4-QAM and 4-PSK schemes within an OFDM-RoFSO transmission link subject to atmospheric turbulence, with results favouring the 4-QAM scheme. In [Kumar and Krishnan (2020a)], a QAM-OFDM RoFSO system is explored, focusing on its applicability within 5G and smart city contexts. This study integrates spatial diversity to enhance performance.

Further investigations include the scrutiny of OFDM-based RoFSO communica-

tion systems under varying weather conditions and urban scenarios, with performance enhancements attained through coding techniques [Balaji and Prabu (2018a)]. [Kim *et al.* (2022)] explores the integration of WLAN-based RF transmission with multi-wavelength FSO transmission, achieving a remarkable 20 Gbps data rate while examining the feasibility of wavelength multiplexing. In [Kaur and Nain (2022)], the authors propose a novel configuration rooted in Multiple Beams Multiple Detectors (MBMD) to augment RoFSO network performance by leveraging multiple optical beams and an array of photodetectors.

Within the FSO domain, optical signals traverse the atmosphere, contending with the impacts of atmospheric turbulence, pointing errors, and attenuation. Moreover, the potential obstruction of these signals by physical impediments such as mountains, buildings, or large trees can pose a perplexing challenge where the transmitted signal fails to reach its intended destination. This phenomenon is often called a skip zone or dead zone issue. To address this concern, the concept of a RIS has emerged as a viable solution [Wang *et al.* (2020a)]. Previously, RIS technology has been effectively deployed to mitigate dead zone complications within wireless communications, heralding the advent of intelligent communication paradigms [ElMossallamy *et al.* (2020)].

RIS technology has emerged as a compelling solution to mitigate the skip or dead zone challenges while concurrently elevating the SNR within wireless communication systems [Wu *et al.* (2021), Basar and Poor (2021)]. Beyond its remedial role in addressing the skip zone issue, RIS introduces the concept of channel reconfigurability to wireless systems [Wu *et al.* (2021)]. In the context of RoFSO communication, RIS units are electronic devices endowed with the capability to manipulate electromagnetic characteristics electronically. Notably, RIS exhibits a superior power-efficiency profile compared to traditional relay systems. The core structure of an RIS module is constituted by an arrangement of multiple mirrors configured in a planar array format [Zeng *et al.* (2020)].

Due to the susceptibility of RoFSO communication to various impairments like atmospheric attenuation, pointing errors, and turbulence-induced fading, the scientific community has endeavoured to develop mathematical models to represent atmospheric turbulence accurately. These models encompass the negative exponential, log-normal, k-distribution, Gamma–Gamma, and M distributions, as outlined in a study by Kashani and Barati [Kashani *et al.* (2015)]. In particular, the M-distribution stands out as a comprehensive model, as elucidated by Jurado *et al.* in [Jurado-Navas

*et al.* (2011b)]. This model captures the irradiance fluctuations exhibited by spherical or planar waves transmitted through atmospheres characterized by turbulent conditions. Jurado further substantiated the efficacy of the M distribution by conducting a comparative analysis between simulated data and experimental results, as presented in [Jurado-Navas *et al.* (2012b)]. The M distribution’s significance lies in its role as a generalized model, as it encompasses several other models as special cases, a fact highlighted in a study by Kumar *et al.* [Kumar and Krishnan (2020a)]. We have harnessed the M-distributed atmospheric turbulence model in the present investigation and employed heterodyne detection (HD). It’s worth noting that HD offers robustness against turbulence-induced effects and is known for its sophistication when compared to the more straightforward Intensity Modulation Direct Detection (IM/DD) scheme, as noted by Tsiftsis and Krikidis in [Tsiftsis (2008)]. Our modulation scheme includes two binary approaches, NBFSK and CBPSK, alongside M-ary quadrature amplitude modulation (M-QAM).

### 5.1.1 Contribution

The contributions of our work are as follows:

- RIS-aided RoFSO system over M-distributed turbulence with two binary modulations and M-QAM modulation for smart city applications has been proposed.
- The novel closed-form expressions of PDF, CDF, OP, ECC, and ABER for the proposed system has been derived.
- OP and ECC have been evaluated for the proposed system with different link lengths and turbulence scenarios.
- The ABER performance of the proposed system under different turbulence regimes, link lengths, and scattering errors have been investigated.

## 5.2 System model

The conceptual design of the RIS-assisted RoFSO system is visually represented in Figure 5.1. Here, the source and the destination are not in direct LOS due to an obstruction, a tall building. To overcome this obstruction, a single light ray is emitted from the source and redirected towards the destination through reflection from RIS

elements. The RIS is strategically positioned on the top floor of the obstructing building, functioning as a reflective surface to redirect the incoming optical signal in the direction of the destination. This setup assumes identical atmospheric channel conditions for both subchannels: the path from the source to the RIS and the path from the RIS to the detector. Complex channel vectors, denoted as "h" and "g," describe the transmission processes along these two paths. Additionally, the pointing error at each receiving point is assumed to remain consistent. The model's versatility renders it suitable for deployment in smart city contexts.

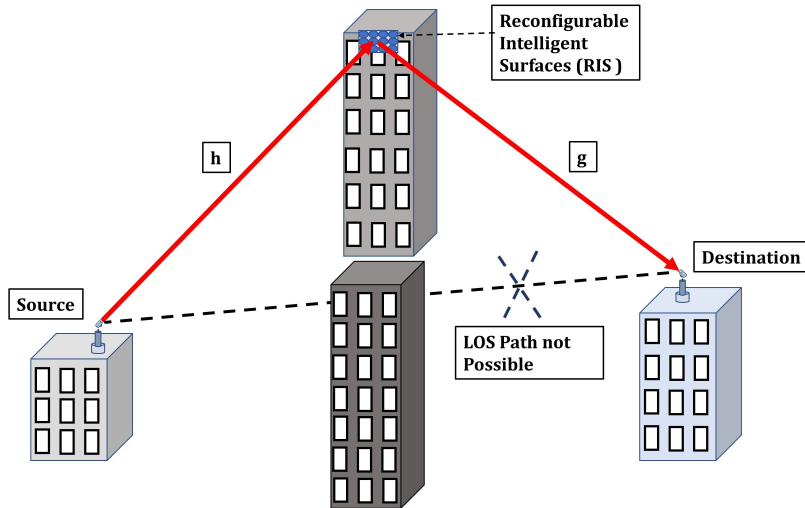


**Figure 5.1:** RIS-aided RoFSO system.

The fundamental block diagram of a RoFSO system is depicted in Figure 5.2. Within the RoFSO system, the information or message signal is first modulated onto an optical carrier. This optical signal is transmitted through the atmospheric medium to reach the receiver. At the receiver, the received optical signal is transformed back into an electrical signal, allowing for the estimation of the conveyed information or message.

### 5.3 Channel model

The RoFSO link is influenced by three primary factors contributing to its degradation: attenuation, atmospheric turbulence, and pointing error, all of which impact the

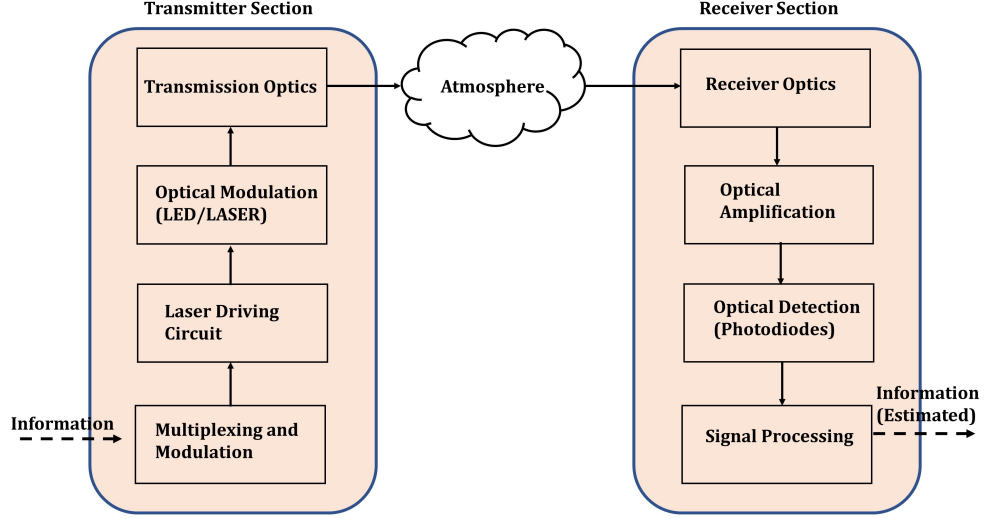


**Figure 5.2:** Block diagram of RoFSO system.

transmitted optical signals. The comprehensive channel model  $I$  can be effectively characterized as the product of three constituent elements, denoted as  $I = I_a I_l I_p$ , Where  $I_a$ ,  $I_p$ , and  $I_l$ , representing the influence of atmospheric turbulence, pointing error, and attenuation, respectively, on the received signal, as previously noted [Kumar and Krishnan (2020a)].

The M distribution model describes the impact of atmospheric turbulence, considering the scattering effects. Consequently, the optical beam comprises three components: the first component represents the LOS with an average power of  $\Omega$ , the second accounts for the scattered component coupled to LOS with an average power of  $2\rho b_0$ , and the third component signifies the scattered component not coupled to LOS with an average power  $g' = 2(1 - \rho)b_0$ , where  $\rho$  characterizes the coupling between the LOS and scattered constituents of the transmitted optical signal. Consequently, the PDF of  $I_a$  is given by [Wang *et al.* (2016)].

$$f_{I_a}(I_a) = A \sum_{m=1}^{\beta} a_m I_a^{\frac{\alpha+m}{2}-1} K_{\alpha-m} \left( 2\sqrt{\frac{\alpha\beta I_a}{g'\beta + \Omega}} \right) \quad (5.1)$$

where

$$A = \frac{2\alpha^{\frac{\alpha}{2}}}{g'^{1+\frac{\alpha}{2}}\Gamma(\alpha)} \left( \frac{g'\beta}{g'\beta + \Omega'} \right)^{\beta+\frac{\alpha}{2}}$$

$$a_m = \binom{\beta-1}{m-1} \frac{(g'\beta + \Omega')^{1-\frac{m}{2}}}{m-1!} \left( \frac{\Omega'}{g'} \right)^{m-1} \left( \frac{\alpha}{\beta} \right)^{\frac{m}{2}}$$

The parameter  $\alpha$  signifies the effective count of large-scale cells involved in the scattering phenomenon. At the same time,  $\beta$  is a natural number tailored to align the PDF with the actual observed data, allowing for a concise mathematical representation [Jurado-Navas *et al.* (2011a)]. The average power resulting from coherent contributions can be mathematically defined as  $(\Omega' = \Omega + 2\rho b_0 + 2\sqrt{2b_0\Omega\rho} \cos(\phi_A - \phi_B))$ . In this equation,  $\phi_A$  characterizes the phase associated with the LOS component, while  $\phi_B$  represents the phase linked to the component coupled to LOS. The angular disparity between  $\phi_A$  and  $\phi_B$  is considered to be  $90^\circ$ .

The PDF describing the pointing error is as follows [Ansari *et al.* (2015), Boluda-Ruiz *et al.* (2017)]:

[Ansari *et al.* (2015), Boluda-Ruiz *et al.* (2017)]

$$f_{I_p}(I_p) = \frac{\xi^2}{A_0^{\xi^2}} (I_p)^{\xi^2} \quad \text{for } 0 \leq I_p \leq A_0. \quad (5.2)$$

Where  $\xi$  represents the ratio of the equivalent beam radius at the receiver to the jitter standard deviation.  $A_0 = [erf(\nu)]^2$ , here  $erf(\cdot)$  is error function and  $\nu = \frac{r\sqrt{\pi}}{\sqrt{2}w_z}$ .  $r$  and  $w_z$  represent the radii of the receiver aperture and the beam waist, respectively.

Ultimately, the path loss, denoted as  $I_l$ , remains relatively constant for specific weather conditions and link distances [Ansari *et al.* (2015)]. It is established through the Beer-Lambert law, which can be expressed as  $I_l = e^{-\delta L}$ . Here,  $\delta$  signifies the attenuation factor, and  $L$  represents the link's length.

The overall channel model for  $I$  is given as [Wang *et al.* (2016)]

$$f_I(I) = \int f_{I/I_a}(I/I_a) f_{I_a}(I_a) dI_a \quad (5.3)$$

Here,  $f_{I/I_a}(I/I_a)$  denotes the conditional probability for a given turbulence state  $I_a$ .

It is defined as

$$\begin{aligned} f_{I/I_a}(I/I_a) &= \frac{1}{I_a I_l} f_{I_p} \left( \frac{I}{I_a I_l} \right) \\ &= \frac{g^2}{A_0^{g^2} I_a I_l} \left( \frac{I}{I_a I_l} \right)^{g^2-1} \end{aligned} \quad (5.4)$$

for  $0 \leq I \leq A_0 I_a I_l$ .

Eqs. (5.1) and (5.4) are substituted in Eq. (5.3) to get  $f_I(I)$  as

$$\begin{aligned} f_I(I) &= \frac{g^2 A}{(A_0 I_l)^{g^2}} (I)^{g^2-1} \times \\ &\sum_{k=1}^b a_k \int_{I/I_l A_0}^{\infty} I_a^{\frac{\alpha+k}{2}-1-g^2} K_{\alpha-k} \left( 2\sqrt{\frac{\alpha\beta I_a}{\gamma\beta + \Omega}} \right) dI_a \end{aligned} \quad (5.5)$$

Final  $f_I(I)$  can be obtained as [Wang *et al.* (2016)]

$$f_I(I) = \frac{\xi^2 A I^{-1}}{2} \sum_{m=1}^{\beta} \left[ b_m G_{1,3}^{3,0} \left( \frac{\alpha\beta I}{(g\beta + \Omega') A_0 I_l} \middle| \begin{matrix} 1 + \xi^2 \\ \xi^2, \alpha, k \end{matrix} \right) \right] \quad (5.6)$$

where  $b_m = a_m \left[ \frac{\alpha\beta}{(g\beta + \Omega')} \right]^{-(\alpha+m)/2}$  and  $G_{p,q}^{m,n}[\cdot]$  is meijer G function.

In the context of HD, where the effective photoelectric conversion ratio is denoted as  $\eta_e$ , the average SNR can be expressed as  $\bar{\gamma} = \eta_e E_l[I]/N_0$ , where,  $N_0$  represents the AWGN sample, and  $E_l[I]$  is the average received irradiance. Upon employing a straightforward random variable transformation, the SNR PDF for HD is given as:

$$f_{\gamma}(\gamma) = \frac{\xi^2 A}{2\gamma} \sum_{m=1}^{\beta} \left[ b_m G_{1,3}^{3,0} \left( B \frac{\gamma}{\bar{\gamma}} \middle| \begin{matrix} 1 + \xi^2 \\ \xi^2, \alpha, m \end{matrix} \right) \right] \quad (5.7)$$

Where  $B = \xi^2 \alpha \beta (g + \Omega') / [(\xi^2 + 1)(g\beta + \Omega')]$  and  $\bar{\gamma}$  is the average SNR.

## 5.4 Closed form Statistical Analysis

In this section, we have developed closed-form analytical expressions for both the end-to-end PDF and the CDF.

### 5.4.1 End to End SNR

The optical signal transmitted from the source to the RIS is considered to be solely reflected from the RIS surface. It is also assumed that there is perfect knowledge of the channel phases at both the RIS and the destination. The received signal at the detector is mathematically expressed as  $y = \sqrt{E_s}(h\mu e^{j\theta}g)x + n$  [Ndjiongue *et al.* (2021a)], where  $E_s$  represents the symbol energy and  $h$  and  $g$  are complex channel vectors denoting the transmission from the source to the RIS and from the RIS to the destination, respectively. Parameters  $\mu$  and  $\theta$  characterize the RIS element, where  $\mu$  signifies the amplitude reflection coefficient, and  $\theta$  represents the phase introduced by the RIS module [Basar (2020), Yigit *et al.* (2020)]. Here,  $x$  and  $y$  correspond to the transmitted and received symbols, respectively, and  $n$  is the additive white Gaussian noise. At the RIS, the primary goal is to optimize the signal's reflection towards the destination, aiming for the highest SNR possible. This optimization involves maximizing the end-to-end SNR, which can be defined as  $\gamma = \bar{\gamma}|h\mu e^{j\theta}g|^2$ .

### 5.4.2 PDF in terms of End to End SNR

The proposed system gain is given by  $h\mu e^{j\theta}g$ , which comprise the deterministic component  $\mu e^{j\theta}$ , alongside the random variables  $h$  and  $g$ . This work focuses on HD.

Thus the SNR's, PDF  $f_\gamma(\gamma)$  is calculated as [Yang *et al.* (2020c)]

$$f_\gamma(\gamma) = \int_0^\infty f_{\gamma_h}(t)f_{\gamma_g}\left(\frac{\gamma}{t}\right)\frac{1}{t}dt \quad (5.8)$$

Here,  $\gamma_h$  and  $\gamma_g$  are the SNR of the sub-channels Source to RIS and RIS to the destination, respectively, and  $f_{\gamma_g}(\cdot)$  and  $f_{\gamma_h}(\cdot)$  are the PDF's of the respective sub-channels. We have assumed constant weather conditions so both sub-channels can be modelled with the same turbulence levels and pointing errors; this will result in a unified PDF defined as [Ansari *et al.* (2015)]

$$f_{\gamma_i}(\gamma_i) = \frac{\xi^2 A}{2\gamma_i} \sum_{m=1}^{\beta} b_m G_{1,3}^{3,0} \left[ B \left( \frac{\gamma_i}{\bar{\gamma}_i} \right) \left| \begin{matrix} \xi^2 + 1 \\ \xi^2, \alpha, m \end{matrix} \right. \right] \quad (5.9)$$

We can now substitute successively  $\gamma_i$  with  $t$  and  $\gamma/t$  in Eq. (5.9) and get  $f_{\gamma_h}(t)$

and  $f_{\gamma_g} \left( \frac{\gamma}{t} \right)$  as

$$f_{\gamma_h}(t) = \frac{\xi^2 A}{2t} \sum_{m=1}^{\beta} b_m G_{1,3}^{3,0} \left[ B \left( \frac{t}{\bar{\gamma}_h} \right) \middle| \begin{matrix} \xi^2 + 1 \\ \xi^2, \alpha, m \end{matrix} \right] \quad (5.10)$$

and

$$f_{\gamma_g} \left( \frac{\gamma}{t} \right) = \frac{\xi^2 A t}{2\gamma} \sum_{m=1}^{\beta} b_m G_{1,3}^{3,0} \left[ B \left( \frac{\gamma}{t \bar{\gamma}_g} \right) \middle| \begin{matrix} \xi^2 + 1 \\ \xi^2, \alpha, m \end{matrix} \right] \quad (5.11)$$

where  $\bar{\gamma}_h$  and  $\bar{\gamma}_g$  are the averages of SNRs  $\gamma_h$  and  $\gamma_g$  respectively.

The reflection property of the Meijer- G function, given by [Karp *et al.* (2016)]

$$G_{p,q}^{m,n} \left[ z \middle| \begin{matrix} A_p \\ B_q \end{matrix} \right] = G_{q,p}^{m,m} \left[ z^{-1} \middle| \begin{matrix} 1 - B_q \\ 1 - A_p \end{matrix} \right] \quad (5.12)$$

After using the reflection property of the Meijer G-function, as given in Eq. (5.12), Eq. (5.11) can be written as

$$f_{\gamma_g} \left( \frac{\gamma}{t} \right) = \frac{\xi^2 A t}{2\gamma} \sum_{m=1}^{\beta} b_m G_{3,1}^{0,3} \left[ \left( \frac{t \bar{\gamma}_g}{B \gamma} \right) \middle| \begin{matrix} 1 - \xi^2, 1 - \alpha, 1 - m \\ -\xi^2 \end{matrix} \right] \quad (5.13)$$

Substituting  $f_{\gamma_h}(t)$  and  $f_{\gamma_g} \left( \frac{\gamma}{t} \right)$  from Eqs. (5.10) and (5.13), in the Eq. (5.8), and after solving with help of [Adamchik and Marichev (1990), Eq. (21)], end-to-end PDF is given as

$$f_{\gamma}(\gamma) = \frac{\xi^2 A}{2} \sum_{m=1}^{\beta} b_m \frac{\xi^2 A}{2\gamma} \sum_{m=1}^{\beta} b_m \times G_{6,2}^{0,6} \left[ \left( \frac{\bar{\gamma}}{B^2 \gamma} \right) \middle| \begin{matrix} 1 - \xi^2, 1 - \alpha, 1 - m, 1 - \xi^2, 1 - \alpha, 1 - m \\ -\xi^2, -\xi^2 \end{matrix} \right] \quad (5.14)$$

Here,  $\bar{\gamma} = \bar{\gamma}_g \bar{\gamma}_h$ , Apply the identity from Eq.(5.12), we get PDF of end to end SNR as

$$f_\gamma(\gamma) = \frac{\xi^2 A}{2} \sum_{m=1}^{\beta} b_m \frac{\xi^2 A}{2\gamma} \sum_{m=1}^{\beta} b_m \times G_{2,6}^{6,0} \left[ \left( \frac{B^2 \gamma}{\bar{\gamma}} \right) \middle| \begin{matrix} 1 + \xi^2, 1 + \xi^2 \\ \xi^2, \alpha, m, \xi^2, \alpha, m \end{matrix} \right] \quad (5.15)$$

### 5.4.3 CDF in terms of End to End SNR

The CDF of end to end SNR  $F_\gamma(\gamma)$  is calculated as

$$F_\gamma(\gamma) = \int_0^\infty f_\gamma(\gamma) d\gamma \quad (5.16)$$

After the substitution of the  $f_\gamma(\gamma)$  from Eq. (5.15) in Eq. (5.16) and permuting the variables  $\gamma$ ,  $x$  and  $\infty$  we get

$$F_\gamma(\gamma) = \frac{\xi^2 A}{2} \sum_{m=1}^{\beta} b_m \frac{\xi^2 A}{2} \sum_{m=1}^{\beta} b_m \times \int_0^\gamma \frac{1}{x} G_{2,6}^{6,0} \left[ \left( \frac{B^2 x}{\bar{\gamma}} \right) \middle| \begin{matrix} 1 + \xi^2, 1 + \xi^2 \\ \xi^2, \alpha, m, \xi^2, \alpha, m \end{matrix} \right] d\gamma \quad (5.17)$$

After solving the above Eq. (5.17) with help of [wolfram (2001a), Eq. (07.34.21.0084.01)] the CDF is given by

$$F_\gamma(\gamma) = \frac{\xi^2 A}{2} \sum_{m=1}^{\beta} b_m \frac{\xi^2 A}{2} \sum_{m=1}^{\beta} b_m \times G_{3,7}^{6,1} \left[ \left( \frac{B^2 \gamma}{\bar{\gamma}} \right) \middle| \begin{matrix} 1, 1 + \xi^2, 1 + \xi^2 \\ \xi^2, \alpha, m, \xi^2, \alpha, m, 0 \end{matrix} \right] \quad (5.18)$$

## 5.5 Performance Analysis

This study evaluates the performance of the RIS-assisted RoFSO system using key metrics, including OP, ECC, and ABER. These metrics are assessed for both binary and M-QAM modulation schemes.

### 5.5.1 Outage Probability

OP serves as a metric for assessing the reliability of the RoFSO system. Outage happens when the end-to-end SNR drops below a predetermined threshold value, which is pre-defined to ensure a specific quality of service. Outage probability is defined as

$$P_{out} = Pr(\gamma \leq \gamma_{th}) = F_{\gamma}(\gamma_{th}) \quad (5.19)$$

Thus the OP,  $P_{out}$  of the proposed RIS-assisted RoFSO system is given by calculating  $F_{\gamma}(\gamma_{th})$  from Eq. (5.18),

$$P_{out} = \frac{\xi^2 A}{2} \sum_{m=1}^{\beta} b_m \frac{\xi^2 A}{2} \sum_{m=1}^{\beta} b_m \times G_{3,7}^{6,1} \left[ \left( \frac{B^2 \gamma_{th}}{\bar{\gamma}} \right) \middle| \begin{matrix} 1, 1 + \xi^2, 1 + \xi^2 \\ \xi^2, \alpha, m, \xi^2, \alpha, m, 0 \end{matrix} \right] \quad (5.20)$$

Where,  $\gamma_{th}$  is the threshold SNR.

### 5.5.2 Ergodic channel capacity

In our proposed system, channel state information is inaccessible to the transmitter, and data is transmitted without feedback. This approach is based on the observation that the overall statistical characteristics of the channel can be assessed while transmitting a single symbol. This is feasible due to the slow-fading nature of atmospheric turbulence, which remains relatively constant throughout symbol transmission. The ergodic channel capacity for HD is given by

$$\bar{C} = \frac{1}{\ln(2)} \int_0^{\infty} \ln(1 + \gamma) f_{\gamma}(\gamma) d\gamma \quad (5.21)$$

After representing  $\ln(1 + \gamma)$  in Meijer G function [[Adamchik and Marichev \(1990\)](#), Eq. (11)] and substituting Eq. (5.15) in Eq. (5.21)  $\bar{C}$  becomes,

$$\begin{aligned} \bar{C} &= \frac{1}{\ln(2)} \int_0^\infty G_{2,2}^{1,2} \left[ \gamma \left| \begin{matrix} 1, 1 \\ 1, 0 \end{matrix} \right. \right] \frac{\xi^2 A}{2} \sum_{m=1}^{\beta} b_m \frac{\xi^2 A}{2\gamma} \sum_{m=1}^{\beta} b_m \times \\ &G_{2,6}^{6,0} \left[ \left( \frac{B^2 \gamma}{\bar{\gamma}} \right) \left| \begin{matrix} 1 + \xi^2, 1 + \xi^2 \\ \xi^2, \alpha, m, \xi^2, \alpha, m \end{matrix} \right. \right] d\gamma. \end{aligned} \quad (5.22)$$

After solving the above Eq. (5.22) using [Adamchik and Marichev (1990), Eq. (21)], we get the closed-form expression of  $\bar{C}$  as

$$\begin{aligned} \bar{C} &= \frac{1}{\ln(2)} \frac{\xi^2 A}{2} \sum_{m=1}^{\beta} b_m \frac{\xi^2 A}{2} \sum_{m=1}^{\beta} b_m \times \\ &G_{4,8}^{8,1} \left[ \left( \frac{B^2}{\bar{\gamma}} \right) \left| \begin{matrix} 1 + \xi^2, 1 + \xi^2, 0, 1 \\ \xi^2, \alpha, m, \xi^2, \alpha, m, 0, 0 \end{matrix} \right. \right]. \end{aligned} \quad (5.23)$$

### 5.5.3 ABER for selected binary schemes and M-QAM

In the FSO data transmission, assessing BER is a pivotal metric for gauging system performance. To begin our analysis, we employ two binary modulation schemes: NBFSK and CBPSK to modulate the data before it's transmitted. The ABER can be quantified utilizing the approach described in [Yang *et al.* (2020b)].

$$\bar{P}_b = \frac{q^p}{2\Gamma(p)} \int_0^\infty e^{-q\gamma} \gamma^{p-1} F_\gamma(\gamma) d\gamma. \quad (5.24)$$

In the Eq. (5.24) for NBFSK,  $p=1$  and  $q=0.5$ , and for CBPSK,  $p=0.5$  and  $q=1$  has been taken. After representing the exponential in Meijer G function [Gradshteyn and Ryzhik (2014)]

$$e^{-x} = G_{0,1}^{1,0} \left[ X \left| \begin{matrix} \cdot \\ 0 \end{matrix} \right. \right], \quad (5.25)$$

The ABER for a system employing NBFSK modulation will be

$$\begin{aligned} \bar{P}_b &= \frac{0.5}{2} \int_0^\infty G_{0,1}^{1,0} \left[ 0.5\gamma \middle| \cdot \right] \frac{\xi^2 A}{2} \sum_{m=1}^{\beta} b_m \frac{\xi^2 A}{2} \sum_{m=1}^{\beta} b_m \times \\ &G_{3,7}^{6,1} \left[ \left( \frac{B^2 \gamma}{\bar{\gamma}} \right) \middle| \begin{matrix} 1, 1 + \xi^2, 1 + \xi^2 \\ \xi^2, \alpha, m, \xi^2, \alpha, m, 0 \end{matrix} \right] d\gamma. \end{aligned} \quad (5.26)$$

After solving the above Eq.(5.26) using [Adamchik and Marichev (1990), Eq.(21)], we get the ABER for NBFSK in closed form expression as

$$\begin{aligned} \bar{P}_b &= \frac{\xi^2 A}{8} \sum_{m=1}^{\beta} b_m \frac{\xi^2 A}{2} \sum_{m=1}^{\beta} \frac{b_m}{2} \times \\ &G_{4,7}^{6,2} \left[ \left( \frac{2B^2}{\bar{\gamma}} \right) \middle| \begin{matrix} 1, 1 + \xi^2, 1 + \xi^2, 0 \\ \xi^2, \alpha, m, \xi^2, \alpha, m, 0 \end{matrix} \right]. \end{aligned} \quad (5.27)$$

After representing the exponential in the Meijer G function, the ABER for CBPSK employing system is expressed as

$$\begin{aligned} \bar{P}_b &= \frac{1}{2\sqrt{\pi}} \int_0^\infty \gamma^{-0.5} G_{0,1}^{1,0} \left[ \gamma \middle| \cdot \right] \frac{\xi^2 A}{2} \sum_{m=1}^{\beta} b_m \frac{\xi^2 A}{2} \sum_{m=1}^{\beta} b_m \times \\ &G_{3,7}^{6,1} \left[ \left( \frac{B^2 \gamma}{\bar{\gamma}} \right) \middle| \begin{matrix} 1, 1 + \xi^2, 1 + \xi^2 \\ \xi^2, \alpha, m, \xi^2, \alpha, m, 0 \end{matrix} \right] d\gamma. \end{aligned} \quad (5.28)$$

After solving the above Eq. (5.28) with help of [Adamchik and Marichev (1990), Eq. (21)], we get the ABER for CBPSK in closed-form expression as

$$\begin{aligned} \bar{P}_b &= \frac{\xi^2 A}{4\sqrt{\pi}} \sum_{m=1}^{\beta} b_m \frac{\xi^2 A}{2} \sum_{m=1}^{\beta} b_m \times \\ &G_{4,7}^{6,2} \left[ \left( \frac{B^2}{\bar{\gamma}} \right) \middle| \begin{matrix} 1, 1 + \xi^2, 1 + \xi^2, 0.5 \\ \xi^2, \alpha, m, \xi^2, \alpha, m, 0 \end{matrix} \right]. \end{aligned} \quad (5.29)$$

M-QAM modulation is also investigated for the proposed RIS-assisted RoFSO

system. The ABER for the M-QAM modulation is given by [Singh and Sappal (2019)]

$$\overline{P}_e = \frac{1 - \frac{1}{\sqrt{M}}}{\log_2 M} \int_0^\infty \text{erfc} \left( \sqrt{\frac{3 \log_2 M \gamma}{4(M-1)}} \right) f_\gamma(\gamma) d\gamma. \quad (5.30)$$

Here  $\text{erfc}(\cdot)$  is complementary error function.

Using the complementary error function equivalent of the Meijer G function [wolfram (2001b), Eq. (06.27.26.0006.01)] ABER for the considered M-QAM modulation scheme is calculated as

$$\begin{aligned} \overline{P}_e = & \frac{1 - \frac{1}{\sqrt{M}}}{\log_2 M \sqrt{\pi}} \int_0^\infty G_{1,2}^{2,0} \left[ \left( \frac{3 \log_2 M \gamma}{4(M-1)} \right) \middle| \begin{matrix} 1 \\ 0, \frac{1}{2} \end{matrix} \right] \frac{\xi^2 A}{2} \sum_{m=1}^{\beta} b_m \frac{\xi^2 A}{2\gamma} \sum_{m=1}^{\beta} b_m \times \\ & G_{2,6}^{6,0} \left[ \left( \frac{B^2 \gamma}{\bar{\gamma}} \right) \middle| \begin{matrix} 1 + \xi^2, 1 + \xi^2 \\ \xi^2, \alpha, m, \xi^2, \alpha, m \end{matrix} \right] d\gamma. \end{aligned} \quad (5.31)$$

After solving the above Eq. (5.31) with help of [Adamchik and Marichev (1990), Eq. (21)] we get the closed-form expression of ABER for M-QAM as

$$\begin{aligned} \overline{P}_e = & \frac{1 - \frac{1}{\sqrt{M}}}{\log_2 M \sqrt{\pi}} \frac{\xi^2 A}{2} \sum_{m=1}^{\beta} b_m \frac{\xi^2 A}{2} \sum_{m=1}^{\beta} b_m \times \\ & G_{4,7}^{6,2} \left[ \left( \frac{4B^2(M-1)}{\bar{\gamma} 3 \log_2 M} \right) \middle| \begin{matrix} 1 + \xi^2, 1 + \xi^2, 1, 1/2 \\ \xi^2, \alpha, m, \xi^2, \alpha, m, 0 \end{matrix} \right]. \end{aligned} \quad (5.32)$$

## 5.6 Results and discussion

This section provides numerical results to elucidate the system's performance. Our research focuses on the RIS-aided RoFSO system. Notably, the source and destination are equidistant from the RIS, positioned at a distance denoted as L km. 1550 nm optical wavelength is considered in this work. Additionally, both subchannels within the system exhibit equivalent refractive structure and index  $c_n^2$ , maintaining constancy throughout a single-symbol transmission.

For different turbulence conditions, the following values for  $c_n^2$ , are considered:  $(5 \times 10^{-13}) m^{-\frac{2}{3}}$  for strong turbulence,  $(2.5 \times 10^{-13}) m^{-\frac{2}{3}}$ , for moderate turbulence, and  $10 \times 10^{-14}) m^{-\frac{2}{3}}$  for weak turbulence, respectively. Within the proposed RIS-

assisted RoFSO system, the RIS elements and the receiver aperture are assumed to have a uniform diameter of  $D = 1$  mm.

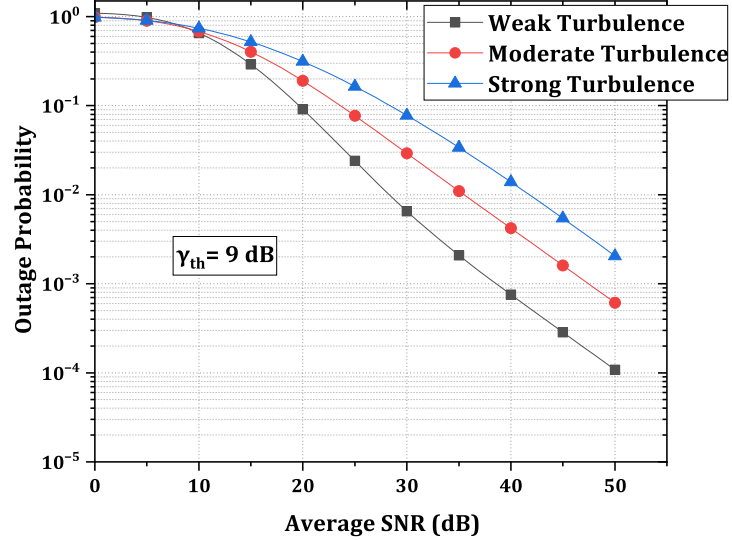


**Figure 5.3:** OP results showing the performance of the RIS-assisted RoFSO system with different turbulence conditions in terms of the SNR.

Figure 5.3 illustrates the OP at a predefined threshold SNR of 9 dB across various turbulence conditions. The link spans a distance of 1 km, and the scattering parameter is set at 0.596. A notable trend in Figure 5.3 is the elevation in OP with increasing turbulence strength, signifying a deterioration in system performance. To uphold an OP of  $10^{-2}$ , the system mandates approximately 28 dB SNR in weak turbulence conditions, 35 dB SNR in moderate turbulence conditions, and 42 dB SNR in strong turbulence conditions.

Figure 5.4 presents the ECC across varying link lengths. The system assumes moderate atmospheric turbulence conditions with a scattering parameter  $\rho$  set to 0.596. The graph illustrates that the channel's capacity diminishes as the link length extends. To sustain a 10 bits/sec/Hz ECC, a 0.5 km link requires a 22 dB SNR. In contrast, the same ECC requires 35 dB SNR for a 1 km link and 37 dB SNR for a 1.5 km one. This implies that with increasing distance, channel capacity decreases. Notably, this decrease is more pronounced at approximately 0.5 km than at distances beyond 1 km within the proposed system.

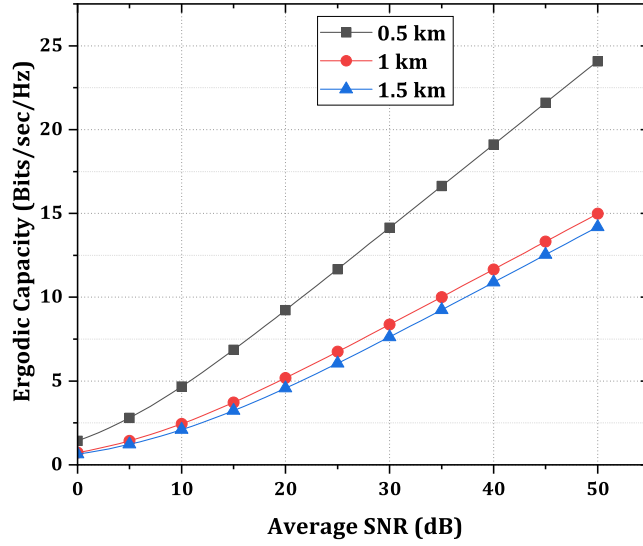


Figure 5.4: ECC against SNR for different link lengths of the channel.

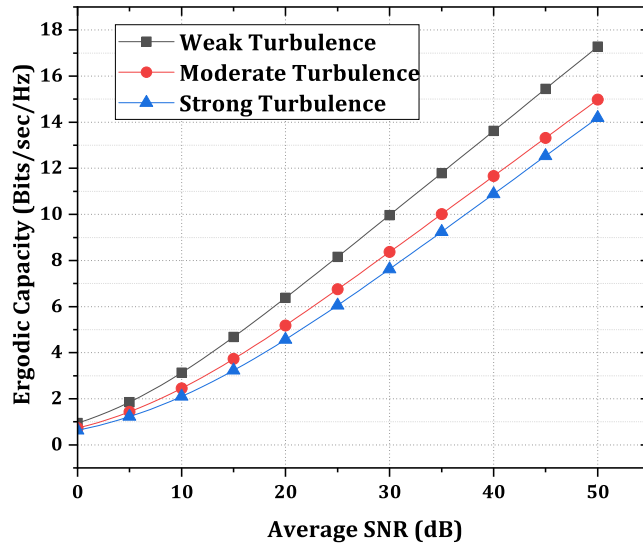
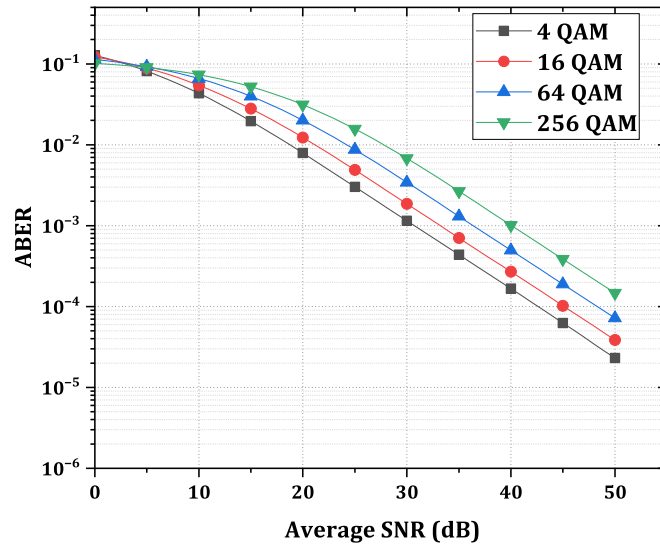


Figure 5.5: ECC against SNR for different turbulence conditions.

Figure 5.5 illustrates the ECC under varying turbulence conditions. The link length is fixed at 1 km, and the scattering parameter  $\rho$  is set to 0.596. The graph demonstrates that the channel's capacity diminishes as the turbulence strength rises. To attain a 10 bits/sec/Hz ECC, weak turbulence demands only 30 dB SNR, moderate turbulence necessitates 35 dB SNR, and strong turbulence requires 37 dB SNR.



**Figure 5.6:** ABER against SNR with various QAM and moderate turbulence in the proposed RIS-assisted RoFSO system.

In Figure 5.6, a link length of 1 km and moderate turbulence conditions were assumed. The figure indicates that the data transmitted over the link also increases with the increase in the order of QAM. Consequently, both spectral efficiency and ABER increase. This illustrates a trade-off between communication reliability and efficiency. When extremely high spectral efficiency is not required, 16-QAM outperforms higher-QAM formats. As a result, this work adopts 16-QAM modulation. Examining the graph, it's evident that to maintain an ABER of  $10^{-4}$ , 4-QAM requires 43 dB SNR, 16-QAM requires 45 dB SNR, 64-QAM requires 48 dB SNR, and 256-QAM demands over 50 dB SNR.

In Figure 5.7, the ABER performance of RIS-assisted RoFSO communication is compared across three different modulation schemes and various link lengths. These comparisons are conducted under moderate turbulence conditions with a scattering parameter  $\rho$  0.596. The graph distinctly reveals that the system's performance degrades

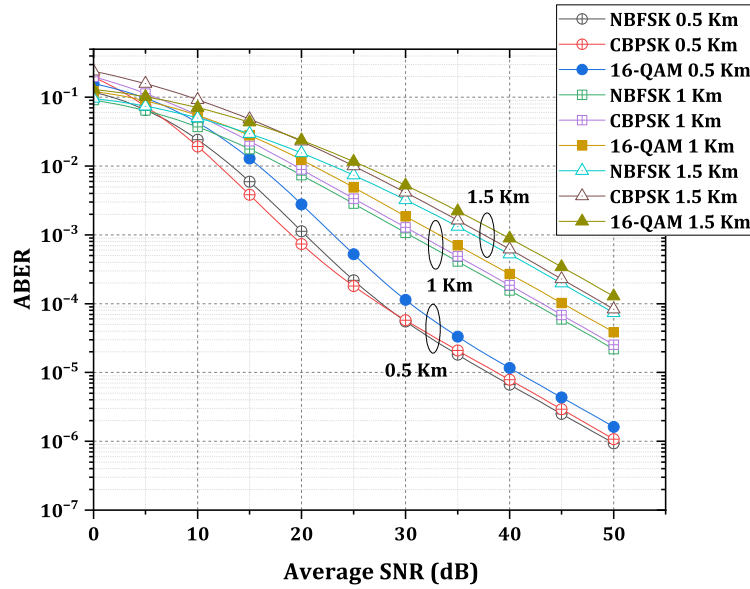
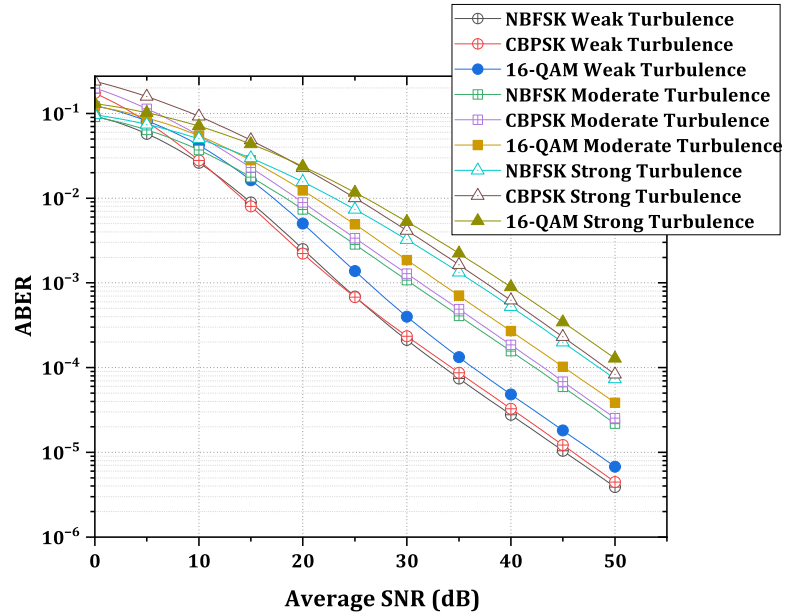


**Figure 5.7:** ABER against SNR with different lengths of communication and different modulation schemes in the proposed RIS-assisted RoFSO system.

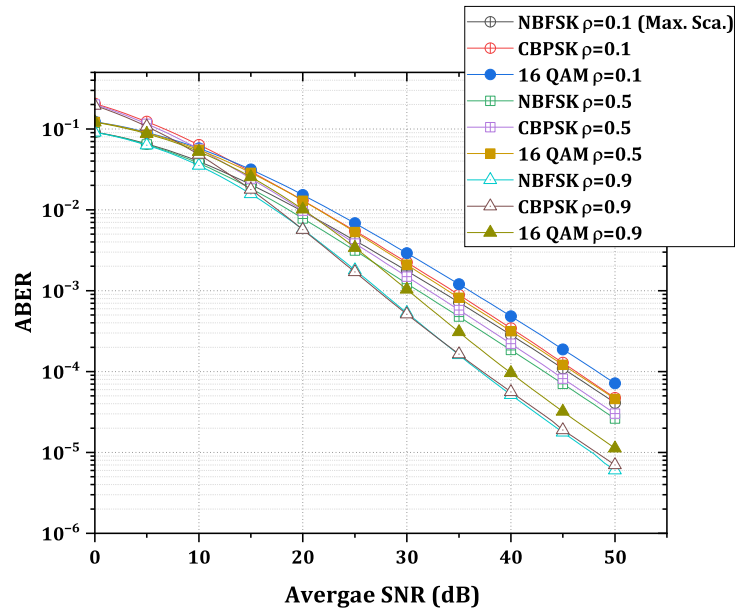
with increased link length. To maintain an ABER of  $10^{-4}$  for 16-QAM modulation, the required SNR is 30 dB at 0.5 km, 45 dB at 1 km, and 50 dB at 1.5 km. Additionally, it's evident that among all three modulation schemes, 16-QAM exhibits a higher ABER compared to the other two binary modulation schemes, NBFSK and CBPSK, across all three link lengths.

Figure 5.8 compares the ABER performance of RIS-assisted RoFSO communication across three distinct modulation schemes under various turbulence conditions. The evaluation is conducted with a 1 km link length and a scattering parameter  $\rho$  0.596. As depicted in the figure, heightened turbulence leads to a noticeable degradation in system performance. Across all three turbulence conditions, 16-QAM exhibited a slightly inferior 1 to 2 dB performance compared to the other two binary modulation schemes.

Figure 5.9 compares the ABER performance of RIS-assisted RoFSO communication involving three distinct modulation schemes under various scattering errors. The evaluation is carried out with a link length of 1 km and under moderate turbulence conditions. The figure clearly illustrates that increased scattering error leads to a degradation in system performance for all three modulation schemes. To maintain an ABER of  $10^{-4}$  with a scattering parameter  $\rho = 0.9$ , 16-QAM necessitates 40 dB SNR.



**Figure 5.8:** ABER against SNR with different turbulence conditions and different modulation schemes in the proposed RIS-assisted RoFSO system.



**Figure 5.9:** ABER against SNR with different scattering error and different modulation schemes in the proposed RIS-assisted RoFSO system.

At  $\rho = 0.5$ , it requires 45 dB SNR; at  $\rho = 0.1$ , it necessitates 47 dB SNR. In summary,

it can be concluded that the impact of scattering error is less pronounced compared to the turbulence effect on the performance of the proposed system.

## 5.7 Summary

This study extensively investigated the performance of the RIS-aided RoFSO system under the influence of the M-distribution. The detection method employed in this research is HD. Notably, this investigation involved deriving closed-form expressions for the PDF and CDF. The study considered three binary modulation techniques: NBFSK, CBPSK, and M-QAM. Leveraging the closed-form expressions, the system's performance was systematically assessed through key metrics, namely, the OP, ECC, and ABER, all expressed in terms of the Meijer-G function. Furthermore, the study featured a comprehensive comparison of various orders of QAM modulation concerning ABER performance. An intriguing observation was that, through RIS, RoFSO communication could be effectively established without the necessity for LOS. Consequently, the proposed system demonstrates its suitability for smart city environments.

# Chapter 6

## RoFSO communication system using multiple RIS for vehicular communication

### 6.1 Introduction

The imperative for efficient resource utilization, driven by urbanization, population growth, and living cost increases, has underscored the development of smart cities. Smart cities aim to integrate information and communication technology into city management and infrastructure. The advent of technologies like augmented reality, virtual reality (VR), the Internet of Things (IoT), and AI-driven applications has led to a surge in data traffic, necessitating ultra-fast wireless connectivity. Vehicular communications, in particular, have gained substantial attention, representing a burgeoning market for cellular system advancements beyond 5G, crucial for diverse smart city applications.

Due to limited spectrum resources, existing RF communications face constraints and may not suffice for the growing demand. Consequently, FSO have emerged as a compelling alternative or complement to RF systems. FSO harnesses unlicensed bandwidth and enables high-speed data transmission over substantial distances. It offers heightened security, immunity to electromagnetic interference, and reduced power consumption, making it a promising solution [Chowdhury *et al.* (2020)].

In FSO communication, challenges like atmospheric turbulence, pointing errors, signal attenuation, and obstacles leading to signal blockage are common. To address these issues and enhance wireless and FSO systems, RISs have been introduced as a hardware solution [Yuan *et al.* (2021)].

RISs provide an effective solution to mitigate dead or skip zones and improve the

SNR of wireless systems [Basar and Poor (2021)]. They excel in customizing channel conditions for wireless systems, outperforming relay systems when equipped with adequate RIS elements [Di Renzo *et al.* (2020)]. These advantages extend to FSO communication. RISs are electronically controllable electromagnetic devices in FSO systems, requiring less power than relays. Extensive research has explored the role of RISs in optical wireless systems and channel models under various physical conditions [Najafi and Schober (2019), Najafi *et al.* (2021)]. For instance, in [Odeyemi *et al.* (2021)], RIS effectiveness in dual-hop decode and forward (DF) relay-enabled asymmetric RF/FSO systems is studied. In [Stefanovic *et al.* (2021)], the performance of RIS-aided FSO communication under atmospheric turbulence is analyzed, considering both first-order and second-order turbulence effects. In [Ndjiongue *et al.* (2021b)], the performance of single RIS-assisted FSO links is examined, focusing on the impact of turbulence and pointing errors. However, limited research has explored using multiple RISs in FSO communication to establish connections between transmitters and receivers. Existing studies mainly concentrate on single RIS-assisted FSO systems. In [Chapala and Zafaruddin (2021)], the potential of using multiple RISs in a hybrid FSO and RF system for multi-hop vehicular communications is investigated.

In [Sandeep *et al.* (2022)], a vehicle-to-infrastructure (V2I) communication system employing roadside infrastructure with transceivers is introduced. The potential of V2I communication in a heterogeneous wireless network is demonstrated in [Dey *et al.* (2016)], focusing on efficient communication utilization and reduced infrastructure requirements while meeting connected vehicle application needs. Authors in [Wang *et al.* (2020b)] present an approach to approximate OP in RIS-assisted vehicular communication under Rayleigh and Rician fading channels, utilizing central limit theorem and series expansion techniques. RIS applications extend to physical layer security for vehicle-to-vehicle (V2V) systems [Mensi *et al.* (2021)] and resource allocation in RIS-aided vehicular communication [Chen *et al.* (2020)]. In [Boulogeorgos *et al.* (2022)], performance analysis of a multi-hop RIS-aided FSO system is conducted, accounting for the impact of Gamma-Gamma atmospheric turbulence and zero boresight pointing errors, utilizing mathematical induction for CDF and PDF derivation. However, further research is needed to analyze multi-RIS-based vehicular communications, focusing on metrics like OP, ergodic capacity, and ABER.

This chapter evaluates single and multi-RIS-aided RoFSO communication systems in a smart city environment, employing the M distribution for modelling at-

atmospheric turbulence. The system utilizes heterodyne detection (HD), offering increased robustness against turbulence compared to intensity modulation direct detection (IM/DD) [Tsiftsis (2008)]. Two modulation schemes are considered: differential binary phase shift keying (DBPSK) and M-ary quadrature amplitude modulation (M-QAM). DBPSK demonstrates resilience to phase shifts caused by frequency-selective fading and multipath propagation. In contrast, M-QAM allows for higher data rates, outperforming modulation schemes like frequency shift keying (FSK) or amplitude shift keying (ASK) by transmitting more symbols per unit time.

### 6.1.1 Contribution

The contribution of our work is as follows.

- To better understand the system performance, we provide a comparative analysis of various metrics for two different scenarios as outlined below:

Scenario 1: The performance of a single RIS-aided RoFSO communication system is analyzed in this case.

Scenario 2: The multi-RIS-assisted RoFSO system performance is analyzed in this case.

- The novel closed-form expressions of PDF, CDF, and various performance metrics, including OP, ECC, and ABER, have been derived.
- Asymptotic analysis for OP performance has been presented.
- OP, ECC, and ABER have been evaluated for the proposed system with different link lengths, turbulence conditions, and scattering errors.

## 6.2 System Model

The system under investigation implements a novel approach for optical wireless communication using a cascaded Reflective Intelligent Surface (RIS) configuration. In this system, a light beam originating from the source (S) is directed towards two distinct destinations labelled Destination 1 (D1) and Destination 2 (D2). This intricate setup is visually presented in Figure 6.1, where various paths are highlighted, denoted as P1, P2, P3, P4, and P5, each corresponding to different communication routes. In this setup, we can differentiate between two scenarios: Scenario 1, represented by S1,

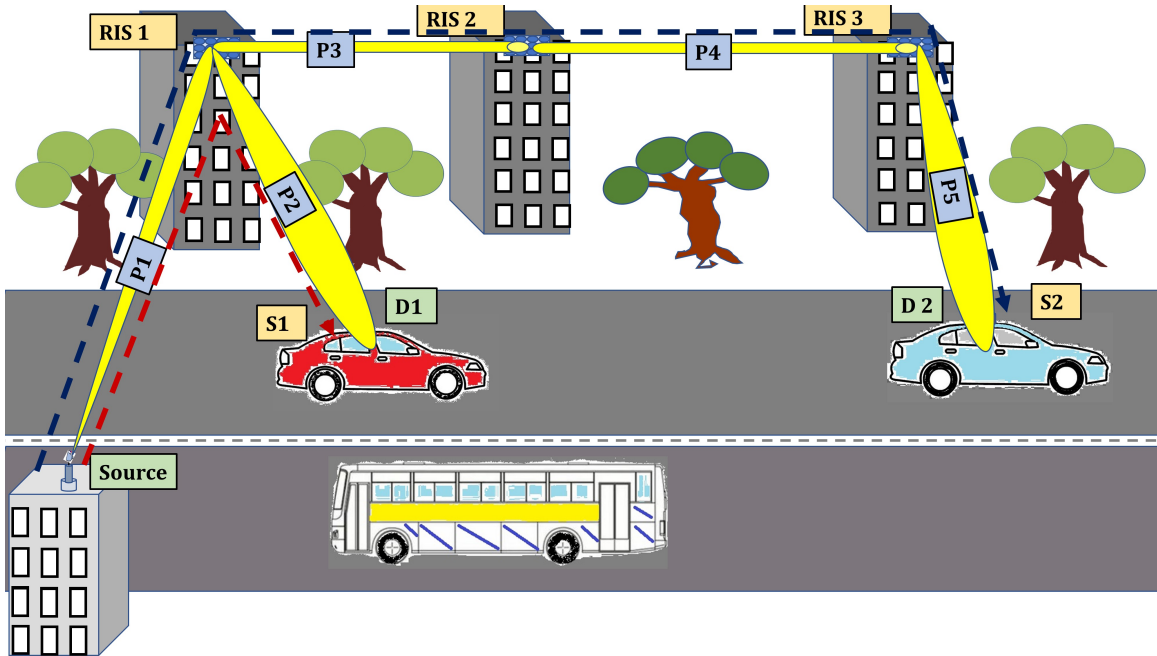


**Figure 6.1:** RIS-assisted RoFSO system for vehicular communication with two scenarios.

encompasses paths P1 and P2, whereas Scenario 2, denoted as S2, involves paths P1, P3, P4, and P5.

The RIS modules are strategically positioned on the uppermost floor of the building. These modules serve as intelligent reflectors, intercepting the incoming optical signal and redirecting it towards the sequence’s next RIS or the intended destination. The study explores two distinct scenarios: the first scenario involves a single RIS, where only one of these intelligent reflectors is employed within the communication system. In contrast, the second scenario uses a multi-RIS setup, utilizing three RIS units to enhance RoFSO. This multi-RIS approach is visually depicted in Figure 6.1. The scenarios simulate varying turbulence levels within the sub-channels, ranging from weak to strong. Furthermore, the analysis accounts for a uniform pointing error experienced by the detectors situated at each receiving end.

### 6.3 Channel model

In the RoFSO, it is essential to account for three significant factors contributing to signal degradation: atmospheric turbulence, path loss, and pointing error. These factors collectively shape our study’s overall channel model, denoted as  $I$ . The channel model can be expressed as the product of three key components:  $I_a$ ,  $I_p$ , and  $I_l$ ; these

components symbolise the impact of atmospheric turbulence, pointing error, and path loss on the received optical signal.

In our investigation, atmospheric turbulence is meticulously characterised by utilising the M-distribution model, as depicted in the graphical representation available in [Aghaei *et al.* (2020), Figure 2 ].

This model delineates the turbulent environment into three distinct constituents. First, we have the line-of-sight component, aptly labelled as  $U_L$ . Secondly, the scattering part disperses along the propagation axis and becomes forward-coupled to the line-of-sight component, termed  $U_S^C$ . Lastly, we encounter an independent scattering component denoted as  $U_S^G$ . Thus, the M-distribution PDF for normalised irradiance is given by [Jurado-Navas *et al.* (2011a), Eqs. (1) and (2)]

$$f_{I_a}(I_a) = A \sum_{m=1}^{\beta} a_m I_a^{\frac{\alpha+m}{2}-1} K_{\alpha-m} \left( 2\sqrt{\frac{\alpha\beta I_a}{g\beta + \Omega}} \right) \quad I_a > 0 \quad (6.1)$$

where,

$$\begin{cases} A = \frac{2\alpha^{\frac{\alpha}{2}}}{g^{1+\frac{\alpha}{2}} \Gamma(\alpha)} \left( \frac{g\beta}{g\beta + \Omega'} \right)^{\beta + \frac{\alpha}{2}} \\ a_m = \binom{\beta-1}{m-1} \frac{(g\beta + \Omega')^{1-\frac{m}{2}}}{(m-1)!} \left( \frac{\Omega'}{g} \right)^{m-1} \left( \frac{\alpha}{\beta} \right)^{\frac{m}{2}} \end{cases}$$

The function  $K_{\alpha-m}(\cdot)$  is the modified Bessel function of the second kind with an order denoted by  $\alpha - m$ . The parameter  $\alpha$  plays a significant role in characterizing the effective number of large-scale cells during the scattering process, directly impacting the system's behaviour. On the other hand,  $\beta$  is a natural number, serving as the fading parameter.

The average power of the independent scattering component is denoted as  $g$ , which can be computed as  $g = \mathbb{E}[|U_S^G|^2] = 2(1 - \rho)b_0$ . Additionally, the average power of the scattering component is  $2b_0$ . The parameter  $\rho$  signifies the ratio of scattering power coupled with the Line-of-Sight (LOS) component concerning the overall scattering component. The term  $\Omega$  embodies the average power of the LOS component  $U_L$ . The average power received from coherent contributions is represented as  $\Omega'$ . This value, derived as  $\Omega' = \Omega + 2\rho b_0 + 2\sqrt{2b_0\Omega\rho} \cos(\phi_A - \phi_B)$ , combines several factors such as LOS and scattering components,  $\rho$ , and the phase difference between  $\phi_A$  and  $\phi_B$ . To elaborate further, the parameters  $\phi_A$  and  $\phi_B$  denote deterministic phases associated with the LOS and LOS-coupled scattering components, respectively.

PDF for depicting pointing error is given by [Ansari *et al.* (2015), Boluda-Ruiz *et al.* (2017)]

$$f_{I_p}(I_p) = \frac{\xi^2}{A_0^{\xi^2}} (I_p)^{\xi^2} \quad 0 \leq I_p \leq A_0 \quad (6.2)$$

Here, the symbol  $\xi$  embodies the essential representation of the ratio between the equivalent beam radius at the receiver and the standard deviation of the jitter. The parameter  $A_0$  holds significant importance, indicating the proportion of collected power precisely at a radial distance of 0. It's noteworthy to mention that  $A_0$  can be calculated as  $A_0 = [\text{erf}(\nu)]^2$ , where the function  $\text{erf}(\cdot)$  signifies the error function, and  $\nu$  is expressed as  $\nu = \frac{r\sqrt{\pi}}{\sqrt{2}w_z}$ . Here,  $r$  and  $w_z$ , respectively, denote the radius of the receiver aperture and the beam waist, playing pivotal roles in characterizing the optical system.

Lastly, the path loss, denoted as  $I_l$ , which can be reasonably assumed to be unchanging for a specific weather condition and link distance [Ansari *et al.* (2015)], is mathematically characterized using the Beer-Lambert law. This expression can be described as follows:  $I_l = e^{-\delta l}$ , where  $\delta$  signifies the attenuation factor and  $l$  is the link length measured in kilometers (km).

The overall channel model for  $I$  is given as [Wang *et al.* (2016), Eq. (8)]

$$f_I(I) = \int f_{I/I_a}(I/I_a) f_{I_a}(I_a) dI_a \quad (6.3)$$

where,  $f_{I/I_a}(I/I_a)$  is a conditional probability for a given turbulence state  $I_a$ . It is defined as

$$\begin{aligned} f_{I/I_a}(I/I_a) &= \frac{1}{I_a I_l} f_{I_p} \left( \frac{I}{I_a I_l} \right) \\ &= \frac{\xi^2}{A_0^{\xi^2} I_a I_l} \left( \frac{I}{I_a I_l} \right)^{\xi^2 - 1} \end{aligned} \quad (6.4)$$

$$0 \leq I \leq A_0 I_a I_l$$

Eqs. (6.1) and (6.4) are substituted in Eq. (6.3) to get  $f_I(I)$  as

$$f_I(I) = \frac{\xi^2 A}{(A_0 I_l)^{\xi^2}} (I)^{\xi^2 - 1} \times \sum_{k=1}^b a_k \int_{I/I_l A_0}^{\infty} I_a^{\frac{\alpha+k}{2} - 1 - \xi^2} K_{\alpha-k} \left( 2 \sqrt{\frac{\alpha \beta I_a}{g \beta + \Omega}} \right) dI_a \quad (6.5)$$

After solving the above Eq. (6.5), the overall channel model can be expressed as

$$f_I(I) = \frac{\xi^2 A I^{-1}}{2} \sum_{m=1}^{\beta} \left[ b_m G_{1,3}^{3,0} \left( \frac{\alpha \beta I}{(g \beta + \Omega') A_0 I_l} \middle| 1 + \xi^2 \right) \right] \quad (6.6)$$

where  $b_m = a_m \left[ \frac{\alpha \beta}{(g \beta + \Omega')} \right]^{-(\alpha+m)/2}$  and  $G_{p,q}^{m,n}[\cdot]$  is the Meijer G-function.

For the HD technique, average SNR is given as  $\bar{\gamma} = \eta_e E_l[I]/N_0$ , where  $\eta_e$  is the effective photoelectric conversion ratio and  $N_0$  symbolizes the AWGN sample and  $E_l[I]$  is average received irradiance. After making use of simple random variable transformation, the SNR  $\gamma$ , PDF  $f_{\gamma}(\gamma)$  for HD is given as

$$f_{\gamma}(\gamma) = \frac{\xi^2 A}{2 \bar{\gamma}} \sum_{m=1}^{\beta} \left[ b_m G_{1,3}^{3,0} \left( B \frac{\gamma}{\bar{\gamma}} \middle| 1 + \xi^2 \right) \right] \quad (6.7)$$

where  $B = \xi^2 \alpha \beta (g + \Omega') / [(\xi^2 + 1)(g \beta + \Omega')]$ ,  $\bar{\gamma}$  is the average SNR.

## 6.4 Closed form Statistical Analysis

In this section, we undertake a comprehensive endeavor to derive precise closed-form expressions pertaining to the PDF and CDF for the end-to-end analysis in both envisaged scenarios.

### 6.4.1 Scenario 1 :Single RIS

Single RIS is used to assist the RoFSO communication

#### 6.4.1.1 End to End SNR

Our system model assumes that the optical signal transmitted from the source to RIS 1 undergoes a singular reflection from the surface of RIS 1. Moreover, we operate under the premise of having complete and precise knowledge of the channel phases at RIS 1 and the destination (D1).

The signal received by the detector can be elegantly expressed as  $y = \sqrt{E_s}(h\mu e^{j\theta}g)x + n$ , as documented in [Ndjiongue *et al.* (2021a)]. Here,  $E_s$  stands for the symbol energy, while  $h$  and  $g$  are intricate channel vectors embodying the transmission from the source to RIS 1 and RIS 1 to D1, respectively. Notably,  $\mu$  and  $\theta$  are critical parameters associated with the RIS element. Specifically,  $\mu$  symbolizes the amplitude reflection coefficient, while  $\theta$  characterizes the phase introduced by the RIS module, as delineated in references [Basar (2020), Yigit *et al.* (2020)]. The symbols  $x$  and  $y$  correspond to the transmitted and received components, respectively, whereas  $n$  signifies the presence of additive white Gaussian noise.

At RIS 1, the central objective is optimally redirecting the signal towards the destination, ensuring that the destination experiences the highest possible SNR. This paramount task hinges upon the maximization of the end-to-end SNR. To be precise, this maximized SNR is briefly defined as  $\gamma = \bar{\gamma}|h\mu e^{j\theta}g|^2$ , wherein  $\bar{\gamma}$  characterizes the end-to-end average SNR encompassing the sub-channels spanning from the source to the destination. This refined conceptualization paves the way for a deeper exploration of the system's performance characteristics.

#### 6.4.1.2 PDF in terms of End to End SNR

The proposed system gain is given by  $h\mu e^{j\theta}g$ , where  $\mu e^{j\theta}$  is deterministic, but  $h$  and  $g$  are random variables. We have considered only HD in our work.

Thus the SNR's PDF  $f_\gamma(\gamma)$  is calculated as [Yang *et al.* (2020c), Eq. (5)]

$$f_\gamma(\gamma) = \int_0^\infty f_{\gamma_h}(t)f_{\gamma_g}\left(\frac{\gamma}{t}\right)\frac{1}{t}dt \quad (6.8)$$

Here  $\gamma_h$  and  $\gamma_g$  are the SNR of sub-channels Source to RIS 1 and RIS 1 to D1, and  $f_{\gamma_g}(\cdot)$  and  $f_{\gamma_h}(\cdot)$  are the PDF's of respective sub-channels. We have assumed constant weather conditions so both sub-channels can be modeled with the same turbulence levels and pointing errors; this will result in a unified PDF defined as [Ansari *et al.* (2015), (Eq. (7))]

$$f_{\gamma_i}(\gamma_i) = \frac{\xi^2 A}{2\gamma_i} \sum_{m=1}^{\beta} b_m G_{1,3}^{3,0} \left[ B \left( \frac{\gamma_i}{\bar{\gamma}_i} \right) \middle| \begin{matrix} \xi^2 + 1 \\ \xi^2, \alpha, m \end{matrix} \right] \quad (6.9)$$

Where  $i \in \{h, g\}$  and  $b_m = a_m[\alpha\beta/(g\beta + \Omega')]^{-(\alpha+m)}$ .

We can now substitute successively  $\gamma_i$  with  $t$  and  $\frac{\gamma}{t}$  in Eq. (6.9) and get  $f_{\gamma_h}(t)$  and  $f_{\gamma_g}(\frac{\gamma}{t})$  as

$$f_{\gamma_h}(t) = \frac{\xi^2 A}{2t} \sum_{m=1}^{\beta} b_m G_{1,3}^{3,0} \left[ B \left( \frac{t}{\bar{\gamma}_h} \right) \middle| \begin{matrix} \xi^2 + 1 \\ \xi^2, \alpha, m \end{matrix} \right] \quad (6.10)$$

and

$$f_{\gamma_g}(\frac{\gamma}{t}) = \frac{\xi^2 A t}{2\gamma} \sum_{m=1}^{\beta} b_m G_{1,3}^{3,0} \left[ B \left( \frac{\gamma}{t\bar{\gamma}_g} \right) \middle| \begin{matrix} \xi^2 + 1 \\ \xi^2, \alpha, m \end{matrix} \right] \quad (6.11)$$

Where  $\bar{\gamma}_h$  and  $\bar{\gamma}_g$  are average of the SNRs  $\gamma_h$  and  $\gamma_g$  respectively. The reflection property of the Meijer-G function, given by [Karp *et al.* (2016)]

$$G_{p,q}^{m,n} \left[ z \middle| \begin{matrix} A_p \\ B_q \end{matrix} \right] = G_{q,p}^{m,m} \left[ z^{-1} \middle| \begin{matrix} 1 - B_q \\ 1 - A_p \end{matrix} \right] \quad (6.12)$$

With the use of the Eq. (6.12), Eq. (6.11) can be written as

$$f_{\gamma_g}(\frac{\gamma}{t}) = \frac{\xi^2 A t}{2\gamma} \sum_{m=1}^{\beta} b_m \times G_{3,1}^{0,3} \left[ \left( \frac{t\bar{\gamma}_g}{B\gamma} \right) \middle| \begin{matrix} 1 - \xi^2, 1 - \alpha, 1 - m \\ -\xi^2 \end{matrix} \right] \quad (6.13)$$

Substituting  $f_{\gamma_h}(t)$  and  $f_{\gamma_g}(\frac{\gamma}{t})$  from Eqs (6.10) and (6.13) respectively, in the Eq. (6.8), and after solving with the help of Meijer G integral expression [Adamchik and

Marichev (1990), Eq. (21)], we get the end-to-end PDF as

$$f_{\gamma}(\gamma) = \frac{\xi^2 A}{2} \sum_{m=1}^{\beta} b_m \frac{\xi^2 A}{2\gamma} \sum_{m=1}^{\beta} b_m G_{6,2}^{0,6} \left[ \left( \frac{\bar{\gamma}}{B^2 \gamma} \right) \middle| \begin{matrix} 1 - \xi^2, 1 - \alpha, 1 - m, 1 - \xi^2, 1 - \alpha, 1 - m \\ -\xi^2, -\xi^2 \end{matrix} \right] \quad (6.14)$$

Here  $\bar{\gamma} = \bar{\gamma}_g \bar{\gamma}_h$ . After Applying the identity from Eq. (6.12), the PDF in terms of end to end SNR becomes

$$f_{\gamma}(\gamma) = \frac{\xi^2 A}{2} \sum_{m=1}^{\beta} b_m \frac{\xi^2 A}{2\gamma} \sum_{m=1}^{\beta} b_m \times G_{2,6}^{6,0} \left[ \left( \frac{B^2 \gamma}{\bar{\gamma}} \right) \middle| \begin{matrix} 1 + \xi^2, 1 + \xi^2 \\ \xi^2, \alpha, m, \xi^2, \alpha, m \end{matrix} \right] \quad (6.15)$$

#### 6.4.1.3 CDF in terms of End to End SNR

The CDF with regard to end to end SNR  $F_{\gamma}(\gamma)$  is calculated as

$$F_{\gamma}(\gamma) = \int_0^{\infty} f_{\gamma}(\gamma) d\gamma \quad (6.16)$$

After the substitution of the  $f_{\gamma}(\gamma)$  from Eq. (6.15) in Eq. (6.16) and permuting the variables  $\gamma_1$ ,  $\infty$  and  $x$  we get

$$F_{\gamma}(\gamma) = \frac{\xi^2 A}{2} \sum_{m=1}^{\beta} b_m \frac{\xi^2 A}{2} \sum_{m=1}^{\beta} b_m \times \int_0^{\gamma} \frac{1}{x} G_{2,6}^{6,0} \left[ \left( \frac{B^2 x}{\bar{\gamma}} \right) \middle| \begin{matrix} 1 + \xi^2, 1 + \xi^2 \\ \xi^2, \alpha, m, \xi^2, \alpha, m \end{matrix} \right] dx \quad (6.17)$$

6. After solving the above Eq. (6.17) with the help of [wolfram (2001a)(Eq. (07.34.21.0084.01))],

we get the CDF as

$$F_\gamma(\gamma) = \frac{\xi^2 A}{2} \sum_{m=1}^{\beta} b_m \frac{\xi^2 A}{2} \sum_{m=1}^{\beta} b_m \times G_{3,7}^{6,1} \left[ \left( \frac{B^2 \gamma}{\bar{\gamma}} \right) \middle| \begin{matrix} 1, 1 + \xi^2, 1 + \xi^2 \\ \xi^2, \alpha, m, \xi^2, \alpha, m, 0 \end{matrix} \right] \quad (6.18)$$

## 6.4.2 Scenario 2: Multi-RIS

Three RIS is used to assist the RoFSO communication

### 6.4.2.1 End to End SNR

Figure 6.1 shows that this configuration employs three RIS to enhance the RoFSO system. Given that the end-to-end SNR for a single RIS-based RoFSO system has been previously established, the present scenario adopts a thoughtful approach. Herein, paths P1 and P3 are considered a unified sub-channel, while paths P4 and P5 are similarly combined into another sub-channel. It's worth noting that all the fundamental assumptions made for the first scenario remain applicable in this context. Consequently, the channel vectors  $h_1$  and  $g_1$  elegantly encapsulate the complex characteristics of the paths, incorporating the amalgamation of P1 and P3, and P4 and P5, respectively.

The signal received at the detector can be described by the expression [Ndjiongue *et al.* (2021a)]:  $y_1 = \sqrt{E_s}(h_1 \mu_1 e^{j\theta_1} g_1)x + n_1$  Here,  $E_s$  represents the symbol energy, and  $\mu_1$  denotes the amplitude reflection coefficient. At the same time,  $h_1$  and  $g_1$  correspond to the intricate channel vectors governing the transmission from the source to the second RIS via the first RIS and from the second RIS to the destination via the third RIS, respectively. The parameter  $\theta_1$  characterizes the phase introduced by the RIS module [Basar (2020), Yigit *et al.* (2020)].

In this context,  $x$  represents the transmitted symbol,  $y_1$  denotes the received symbol, and  $n_1$  accounts for the additive white Gaussian noise. The primary aim of the RIS in this setup is to efficiently reflect the signal towards the intended destination, thereby optimizing the SNR experienced at the destination. To achieve this objective, the maximization of the end-to-end SNR is imperative. The maximized SNR is expressed as:  $\gamma_1 = \bar{\gamma}_1 |h_1 \mu e^{j\theta_1} g_1|^2$ . Here,  $\bar{\gamma}_1$  signifies the average SNR defined for both the source to RIS and RIS to destination sub-channels.

### 6.4.2.2 PDF in terms of End to End SNR

System gain is given by  $h_1\mu_1e^{j\theta_1}g_1$ , where  $\mu_1e^{j\theta_1}$  is deterministic, but  $h_1$  and  $g_1$  are random variables. Same as scenario 1, HD is considered in scenario 2.

Thus the SNR's, PDF  $f_{\gamma_1}(\gamma_1)$  is calculated as [Yang *et al.* (2020c)]

$$f_{\gamma_1}(\gamma_1) = \int_0^\infty f_{\gamma_{1h_1}}(t)f_{\gamma_{1g_1}}\left(\frac{\gamma_1}{t}\right)\frac{1}{t}dt, \quad (6.19)$$

Where  $\gamma_{1h_1}$  and  $\gamma_{1g_1}$  are the SNR of sub-channels, Source to 2nd RIS through 1st RIS and 2nd RIS to D2 through 3rd RIS, and  $f_{\gamma_{1h_1}}(\cdot)$  and  $f_{\gamma_{1g_1}}(\cdot)$  are the PDF's of respective sub-channels. We have assumed the same conditions as in scenario 1. Thus, the unified end-to-end SNR PDF is defined as [Ansari *et al.* (2015)]

$$f_{\gamma_{1i}}(\gamma_{1i}) = \frac{\xi^2 A}{2} \sum_{m=1}^{\beta} b_m \frac{\xi^2 A}{2\gamma_{1i}} \sum_{m=1}^{\beta} b_m \times G_{2,6}^{6,0} \left[ \left( \frac{B^2 \gamma_{1i}}{\gamma_{1i}} \right) \middle| \begin{matrix} 1 + \xi^2, 1 + \xi^2 \\ \xi^2, \alpha, m, \xi^2, \alpha, m \end{matrix} \right] \quad (6.20)$$

All variables represent the same as explained in scenario 1.

$\gamma_{1i}$  is substituted successively with  $t$  and  $\frac{\gamma_1}{t}$  in Eq. (6.19) thus,  $f_{\gamma_{1h_1}}(t)$  and  $f_{\gamma_{1g_1}}\left(\frac{\gamma_1}{t}\right)$  becomes

$$f_{\gamma_{1h_1}}(t) = \frac{\xi^2 A}{2} \sum_{m=1}^{\beta} b_m \frac{\xi^2 A}{2t} \sum_{m=1}^{\beta} b_m \times G_{2,6}^{6,0} \left[ \left( \frac{B^2 t}{\gamma_{1h_1}} \right) \middle| \begin{matrix} 1 + \xi^2, 1 + \xi^2 \\ \xi^2, \alpha, m, \xi^2, \alpha, m \end{matrix} \right] \quad (6.21)$$

and

$$f_{\gamma_{1g_1}} \left( \frac{\gamma_1}{t} \right) = \frac{\xi^2 A}{2} \sum_{m=1}^{\beta} b_m \frac{\xi^2 A t}{2\gamma_1} \sum_{m=1}^{\beta} b_m \times G_{2,6}^{6,0} \left[ \left( \frac{B^2 \gamma_1}{t \bar{\gamma}_{1h_1}} \right) \middle| \begin{array}{l} 1 + \xi^2, 1 + \xi^2 \\ \xi^2, \alpha, m, \xi^2, \alpha, m \end{array} \right]. \quad (6.22)$$

By using identity (6.12) above Eq. (6.22) becomes

$$f_{\gamma_{1g_1}} \left( \frac{\gamma_1}{t} \right) = \frac{\xi^2 A}{2} \sum_{m=1}^{\beta} b_m \frac{\xi^2 A t}{2\gamma_1} \sum_{m=1}^{\beta} b_m \times G_{6,2}^{0,6} \left[ \left( \frac{t \bar{\gamma}_{1h_1}}{B^2 \gamma_1} \right) \middle| \begin{array}{l} \nabla_1 \\ \nabla_2 \end{array} \right], \quad (6.23)$$

Where  $\nabla_1 = -\xi^2, 1 - \alpha, 1 - m, 1 - \xi^2, 1 - \alpha, 1 - m$  and  $\nabla_2 = -\xi^2, -\xi^2$ .

Substituting  $f_{\gamma_{1h_1}}(t)$  and  $f_{\gamma_{1g_1}}(\frac{\gamma_1}{t})$  from Eqs (6.21) and (6.23), in the Eq. (6.19), and after solving, with the help of [Adamchik and Marichev (1990),Eq. (21)], we get the end-to-end PDF as

$$f_{\gamma_1}(\gamma_1) = \frac{\xi^2 A}{2} \sum_{m=1}^{\beta} b_m \frac{\xi^2 A}{2} \sum_{m=1}^{\beta} b_m \frac{\xi^2 A}{2} \sum_{m=1}^{\beta} b_m \frac{\xi^2 A}{2} \sum_{m=1}^{\beta} b_m \times G_{12,4}^{0,12} \left[ \left( \frac{\bar{\gamma}_1}{B^3 \gamma_1} \right) \middle| \begin{array}{l} \Delta_1 \\ \Delta_2 \end{array} \right], \quad (6.24)$$

Where  $\Delta_1 = 1 - \xi^2, 1 - \alpha, 1 - m, 1 - \xi^2, 1 - \alpha, 1 - m, 1 - \xi^2, 1 - \alpha, 1 - m, 1 - \xi^2, 1 - \alpha, 1 - m$  and  $\Delta_2 = -\xi^2, -\xi^2, -\xi^2, -\xi^2$ .

By using Eq. (6.12) we can write above Eq. (6.24) as

$$f_{\gamma_1}(\gamma_1) = \frac{\xi^2 A}{2} \sum_{m=1}^{\beta} b_m \frac{\xi^2 A}{2} \sum_{m=1}^{\beta} b_m \frac{\xi^2 A}{2} \sum_{m=1}^{\beta} b_m \frac{\xi^2 A}{2} \sum_{m=1}^{\beta} b_m \times G_{4,12}^{12,0} \left[ \left( \frac{B^3 \gamma_1}{\bar{\gamma}_1} \right) \middle| \begin{array}{l} \Delta_3 \\ \Delta_4 \end{array} \right], \quad (6.25)$$

Where  $\Delta_3 = 1 + \xi^2, 1 + \xi^2, 1 + \xi^2, 1 + \xi^2$  and  $\Delta_4 = \xi^2, \alpha, m, \xi^2, \alpha, m, \xi^2, \alpha, m, \xi^2, \alpha, m$ .

### 6.4.2.3 CDF in terms of End to End SNR

As stated in scenario one, the CDF in terms of end-to-end SNR  $F_{\gamma_1}(\gamma_1)$  is expressed as

$$F_{\gamma_1}(\gamma_1) = \int_0^\infty f_{\gamma_1}(\gamma_1) d\gamma \quad (6.26)$$

After the substitution of the  $f_{\gamma_1}(\gamma_1)$  from Eq. (6.25) in Eq. (6.26) and permuting the variables  $\gamma_1$ ,  $\infty$  and  $x$  and we get

$$F_{\gamma_1}(\gamma_1) = \frac{\xi^2 A}{2} \sum_{m=1}^{\beta} b_m \frac{\xi^2 A}{2} \sum_{m=1}^{\beta} b_m \frac{\xi^2 A}{2} \sum_{m=1}^{\beta} b_m \frac{\xi^2 A}{2} \sum_{m=1}^{\beta} b_m \times \int_0^\gamma \frac{1}{x} G_{4,12}^{12,0} \left[ \left( \frac{B^3 \gamma_1}{\bar{\gamma}_1} \right) \middle| \begin{matrix} \Delta_3 \\ \Delta_4 \end{matrix} \right] dx, \quad (6.27)$$

Where  $\Delta_3$  and  $\Delta_4$  is same as stated above After solving the above Eq. (6.27) with the help of [wolfram (2001a), Eq. (07.34.21.0084.01)], we got the CDF as

$$F_{\gamma_1}(\gamma_1) = \frac{\xi^2 A}{2} \sum_{m=1}^{\beta} b_m \frac{\xi^2 A}{2} \sum_{m=1}^{\beta} b_m \frac{\xi^2 A}{2} \sum_{m=1}^{\beta} b_m \frac{\xi^2 A}{2} \sum_{m=1}^{\beta} b_m \times G_{5,13}^{12,1} \left[ \left( \frac{B^2 \gamma_1}{\bar{\gamma}_1} \right) \middle| \begin{matrix} 1, 1 + \xi^2, 1 + \xi^2, 1 + \xi^2, 1 + \xi^2 \\ \xi^2, \alpha, m, \xi^2, \alpha, m, \xi^2, \alpha, m, \xi^2, \alpha, m, 0 \end{matrix} \right]. \quad (6.28)$$

## 6.5 Performance analysis

This section is dedicated to a comprehensive performance analysis of the proposed system, considering both single- and multi-RIS configurations in RoFSO scenarios. The assessment involves meticulously evaluating key performance metrics, including ABER, OP, and End-to-End ECC.

### 6.5.1 Outage Probability

#### 6.5.1.1 Scenario 1: Single RIS

The OP serves as a pivotal metric in assessing the reliability of the RoFSO system. It quantifies the probability of the receiver's instantaneous SNR dropping below a

predetermined threshold value. This parameter is crucial in evaluating the system's robustness and ability to maintain a consistent connection under varying conditions.

OP is given as

$$P_{out} = Pr(\gamma \leq \gamma_{th}) = F_{\gamma}(\gamma_{th}). \quad (6.29)$$

Thus, the OP  $P_{out}$  of the proposed RIS-assisted RoFSO system is determined by evaluating  $F_{\gamma}(\gamma_{th})$  from Eq. (6.18),

$$P_{out} = \frac{\xi^2 A}{2} \sum_{m=1}^{\beta} b_m \frac{\xi^2 A}{2} \sum_{m=1}^{\beta} b_m \times G_{3,7}^{6,1} \left[ \left( \frac{B^2 \gamma_{th}}{\bar{\gamma}} \right) \middle| \begin{matrix} 1, 1 + \xi^2, 1 + \xi^2 \\ \xi^2, \alpha, m, \xi^2, \alpha, m, 0 \end{matrix} \right], \quad (6.30)$$

Where  $\gamma_{th}$  is the threshold SNR.

### Asymptotic Analysis

By leveraging the reflective properties of the Meijer-G function as indicated in Eq. (6.12) and referencing (Ansari *et al.*, 2015, Eq. (41)), it is feasible to invert the arguments of Meijer's G function present in Eq. (6.30). As a result, we derive the asymptotic expression of the OP at high SNR in terms of elementary functions as

$$P_{out} \cong \frac{\xi^2 A}{2} \sum_{m=1}^{\beta} b_m \frac{\xi^2 A}{2} \sum_{m=1}^{\beta} b_m \times \sum_{k=1}^6 \left( \frac{\bar{\gamma}}{B^2 \gamma_{th}} \right)^{a_k - 1} \frac{\prod_{l=1; l \neq k}^6 \Gamma(a_k - a_l) \Gamma(1 - a_k)}{\Gamma(2 - a_k) \prod_{l=2}^3 \Gamma(a_k - b_l)}. \quad (6.31)$$

#### 6.5.1.2 Scenario 2: Multi-RIS

As stated in Scenario 1, the expression for the OP is given by:

$$P_{out} = Pr(\gamma_1 \leq \gamma_{th}) = F_{\gamma_1}(\gamma_{th}). \quad (6.32)$$

Thus, the OP  $P_{out}$  of the proposed multi-RIS-assisted RoFSO system is determined by evaluating  $F_{\gamma_1}(\gamma_{th})$  from Eq. (6.28)

$$P_{out} = \frac{\xi^2 A}{2} \sum_{m=1}^{\beta} b_m \frac{\xi^2 A}{2} \sum_{m=1}^{\beta} b_m \frac{\xi^2 A}{2} \sum_{m=1}^{\beta} b_m \frac{\xi^2 A}{2} \sum_{m=1}^{\beta} b_m \times G_{5,13}^{12,1} \left[ \left( \frac{B^2 \gamma_{th}}{\bar{\gamma}_1} \right) \middle| \begin{array}{l} 1, 1 + \xi^2, 1 + \xi^2, 1 + \xi^2, 1 + \xi^2 \\ \xi^2, \alpha, m, \xi^2, \alpha, m, \xi^2, \alpha, m, \xi^2, \alpha, m, 0 \end{array} \right], \quad (6.33)$$

Where  $\gamma_{th}$  is the threshold SNR.

### Asymptotic Analysis

Utilizing the Meijer-G function's reflective property based on Eq. (6.12) and making use of the relationship from [Ansari *et al.* (2015), Eq. (41)], we can reverse the arguments within Meijer's G function in Eq. (6.33). Consequently, we derive an asymptotic expression for the OP under high SNR conditions, expressing it in terms of elementary functions as

$$P_{out} \cong \frac{\xi^2 A}{2} \sum_{m=1}^{\beta} b_m \frac{\xi^2 A}{2} \sum_{m=1}^{\beta} b_m \frac{\xi^2 A}{2} \sum_{m=1}^{\beta} b_m \frac{\xi^2 A}{2} \sum_{m=1}^{\beta} b_m \times \sum_{k=1}^{12} \left( \frac{\bar{\gamma}}{B^4 \gamma_{th}} \right)^{a_k - 1} \frac{\prod_{l=1; l \neq k}^{12} \Gamma(a_k - a_l) \Gamma(1 - a_k)}{\Gamma(2 - a_k) \prod_{l=2}^5 \Gamma(a_k - b_l)}. \quad (6.34)$$

## 6.5.2 Ergodic Channel Capacity

### 6.5.2.1 Scenario 1: Single RIS

The proposed system employs a sufficiently long symbol duration to accommodate data encoding across all potential channel fading states. Additionally, the atmospheric turbulence, characterized by slow fading in the RoFSO channel, remains consistent throughout symbol transmission. However, the presence of pointing errors causes rapid signal fluctuations. By evaluating the statistical properties of the channel during the transference of a single symbol, the system's ECC can be assessed through ergodic channel analysis [Ansari *et al.* (2015)].

The ECC for the proposed RoFSO system is given by

$$\bar{C} = \frac{1}{\ln(2)} \int_0^\infty \ln(1 + \gamma) f_\gamma(\gamma) d\gamma. \quad (6.35)$$

Using the Meijer's G-function representation of  $\ln(1 + \gamma)$  [Adamchik and Marichev (1990), Eq. (11)] and substituting Eq. (6.15) in Eq. (6.33),  $\bar{C}$  is given as

$$\begin{aligned} \bar{C} = & \frac{1}{\ln(2)} \int_0^\infty G_{2,2}^{1,2} \left[ \gamma \left| \begin{matrix} 1, 1 \\ 1, 0 \end{matrix} \right. \right] \frac{\xi^2 A}{2} \sum_{m=1}^\beta b_m \frac{\xi^2 A}{2\gamma} \sum_{m=1}^\beta b_m \times \\ & G_{2,6}^{6,0} \left[ \left( \frac{B^2 \gamma}{\bar{\gamma}} \right) \left| \begin{matrix} 1 + \xi^2, 1 + \xi^2 \\ \xi^2, \alpha, m, \xi^2, \alpha, m \end{matrix} \right. \right] d\gamma. \end{aligned} \quad (6.36)$$

After solving the above Eq. (6.36) using [Adamchik and Marichev (1990), Eq. (21)] the closed-form expression of  $\bar{C}$  is given as

$$\begin{aligned} \bar{C} = & \frac{\xi^2 A}{2\ln(2)} \sum_{m=1}^\beta b_m \frac{\xi^2 A}{2} \sum_{m=1}^\beta b_m \times \\ & G_{4,8}^{8,1} \left[ \left( \frac{B^2}{\bar{\gamma}} \right) \left| \begin{matrix} 1 + \xi^2, 1 + \xi^2, 0, 1 \\ \xi^2, \alpha, m, \xi^2, \alpha, m, 0, 0 \end{matrix} \right. \right]. \end{aligned} \quad (6.37)$$

### 6.5.2.2 Scenario 2: Multi-RIS

As outlined in the first scenario, the ECC performance can be evaluated. The expression for the ECC of the proposed RoFSO system is

$$\bar{C} = \frac{1}{\ln(2)} \int_0^\infty \ln(1 + \gamma_1) f_{\gamma_1}(\gamma_1) d\gamma. \quad (6.38)$$

With the help of [Adamchik and Marichev (1990), Eq. (11)],  $\ln(1 + \gamma)$  is converted in the form of Meijer's G-function and after substituting Eq. (6.24) in Eq. (6.38),  $\bar{C}$  is given as

$$\begin{aligned} \bar{C} &= \frac{1}{\ln(2)} \int_0^\infty G_{2,2}^{1,2} \left[ \gamma_1 \left| \begin{matrix} 1, 1 \\ 1, 0 \end{matrix} \right. \right] \frac{\xi^2 A}{2} \sum_{m=1}^\beta b_m \frac{\xi^2 A}{2} \sum_{m=1}^\beta b_m \frac{\xi^2 A}{2} \\ &\quad \sum_{m=1}^\beta b_m \frac{\xi^2 A}{2} \sum_{m=1}^\beta b_m \times G_{4,12}^{12,0} \left[ \left( \frac{B^3 \gamma_1}{\bar{\gamma}_1} \right) \left| \begin{matrix} \Delta_3 \\ \Delta_4 \end{matrix} \right. \right] d\gamma_1, \end{aligned} \quad (6.39)$$

Where  $\Delta_3 = 1 + \xi^2, 1 + \xi^2, 1 + \xi^2, 1 + \xi^2$  and  $\Delta_4 = \xi^2, \alpha, m, \xi^2, \alpha, m, \xi^2, \alpha, m, \xi^2, \alpha, m$ .

Thus, after solving the above integration with the help of [Adamchik and Marichev (1990), Eq. (21)], the closed-form expression of ECC  $\bar{C}$  is given as

$$\begin{aligned} \bar{C} &= \frac{\xi^2 A}{2 \ln(2)} \sum_{m=1}^\beta b_m \frac{\xi^2 A}{2} \sum_{m=1}^\beta b_m \frac{\xi^2 A}{2} \sum_{m=1}^\beta b_m \frac{\xi^2 A}{2} \sum_{m=1}^\beta b_m \times \\ &\quad G_{6,14}^{14,1} \left[ \left( \frac{B^4}{\bar{\gamma}} \right) \left| \begin{matrix} 1 + \xi^2, 1 + \xi^2, 1 + \xi^2, 1 + \xi^2, 0, 1 \\ \xi^2, \alpha, m, \xi^2, \alpha, m, \xi^2, \alpha, m, \xi^2, \alpha, m, 0, 0 \end{matrix} \right. \right]. \end{aligned} \quad (6.40)$$

### 6.5.3 ABER for DBPSK and M-QAM

#### 6.5.3.1 Scenario 1: Single RIS

BER is an essential metric for evaluating system performance in RoFSO data transmission. First, consider that DBPSK has modulated the data before transmission. The ABER can be evaluated using.

Yang *et al.* (2020b)

$$\bar{P}_b = \frac{q^p}{2\Gamma(p)} \int_0^\infty e^{-q\gamma} \gamma^{p-1} F_\gamma(\gamma) d\gamma. \quad (6.41)$$

To calculate the ABER of DBPSK modulated system, we need to set  $p=1$  and  $q=1$  in Eq. (6.41).

The exponential function is expressed in Meijer-G function [Adamchik and Marichev (1990), Eq. (11)] and  $F_\gamma(\gamma)$  is substituted from Eq.(6.18) into Eq. (6.41). Thus the ABER of the proposed system with DBSK modulation will be

$$\begin{aligned} \bar{P}_b &= \frac{1}{2} \int_0^\infty G_{0,1}^{1,0} \left[ \gamma \middle| \cdot \right] \frac{\xi^2 A}{2} \sum_{m=1}^\beta b_m \frac{\xi^2 A}{2} \sum_{m=1}^\beta b_m \times \\ &G_{3,7}^{6,1} \left[ \left( \frac{B^2 \gamma}{\bar{\gamma}} \right) \middle| \begin{matrix} 1, 1 + \xi^2, 1 + \xi^2 \\ \xi^2, \alpha, m, \xi^2, \alpha, m, 0 \end{matrix} \right] d\gamma. \end{aligned} \quad (6.42)$$

After solving the above Eq. (6.42) using [Adamchik and Marichev (1990), Eq. (21)], we got  $\bar{P}_b$  as

$$\begin{aligned} \bar{P}_b &= \frac{\xi^2 A}{4} \sum_{m=1}^\beta b_m \frac{\xi^2 A}{2} \sum_{m=1}^\beta b_m \times \\ &G_{4,7}^{6,2} \left[ \left( \frac{B^2}{\bar{\gamma}} \right) \middle| \begin{matrix} 1, 1 + \xi^2, 1 + \xi^2, 0 \\ \xi^2, \alpha, m, \xi^2, \alpha, m, 0 \end{matrix} \right]. \end{aligned} \quad (6.43)$$

The proposed RIS-assisted RoFSO system also considers M-QAM modulation, for which the ABER is given as [Singh and Sappal (2019), Eq.(67)]

$$\bar{P}_b = \frac{2(1 - \frac{1}{\sqrt{M}})}{\log_2 M} \int_0^\infty Q \left( \sqrt{\frac{3 \log_2 M \gamma}{2(M-1)}} \right) f_\gamma(\gamma) d\gamma. \quad (6.44)$$

After writing Q function in terms of complementary error function [Kschischang (2017)], ABER  $\bar{P}_b$  is given as

$$\bar{P}_b = \frac{(1 - \frac{1}{\sqrt{M}})}{\log_2 M} \int_0^\infty \operatorname{erfc} \left( \sqrt{\frac{3 \log_2 M \gamma}{4(M-1)}} \right) f_\gamma(\gamma) d\gamma. \quad (6.45)$$

After substituting the *erfc* function from Meijer's G function [wolfram (2001b), Eq. (06.27.26.0006.01)] and  $f_\gamma(\gamma)$  from Eq. (6.15), we get  $\bar{P}_e$  as

$$\begin{aligned} \bar{P}_b &= \frac{1 - \frac{1}{\sqrt{M}}}{\log_2 M \sqrt{\pi}} \int_0^\infty G_{1,2}^{2,0} \left[ \left( \frac{3 \log_2 M \gamma}{4(M-1)} \right) \cdot \middle| \begin{matrix} 1 \\ 0, \frac{1}{2} \end{matrix} \right] \frac{\xi^2 A}{2} \times \\ &\sum_{m=1}^\beta b_m \frac{\xi^2 A}{2\gamma} \sum_{m=1}^\beta b_m \times G_{2,6}^{6,0} \left[ \left( \frac{B^2 \gamma}{\bar{\gamma}} \right) \middle| \begin{matrix} 1 + \xi^2, 1 + \xi^2 \\ \xi^2, \alpha, m, \xi^2, \alpha, m \end{matrix} \right]. \end{aligned} \quad (6.46)$$

After solving the above Eq. (6.46) using [Adamchik and Marichev (1990), Eq. (21)], we obtain a closed-form expression for ABER of M-QAM modulated transmis-

sion, which is given by

$$\begin{aligned} \bar{P}_b = & \frac{1 - \frac{1}{\sqrt{M}}}{\log_2 M \sqrt{\pi}} \frac{\xi^2 A}{2} \sum_{m=1}^{\beta} b_m \frac{\xi^2 A}{2} \sum_{m=1}^{\beta} b_m \times \\ & G_{4,7}^{6,2} \left[ \left( \frac{4B^2(M-1)}{3\bar{\gamma} \log_2 M} \right) \middle| \begin{array}{l} 1 + \xi^2, 1 + \xi^2, 1, 1/2 \\ \xi^2, \alpha, m, \xi^2, \alpha, m, 0 \end{array} \right]. \end{aligned} \quad (6.47)$$

### 6.5.3.2 Scenario 2: Multi-RIS

As stated in scenario 1, The ABER for the transmission of DBPSK modulated signal is given by [Yang \*et al.\* \(2020b\)](#)

$$\bar{P}_b = \frac{q^p}{2\Gamma(p)} \int_0^{\infty} e^{-q\gamma_1} \gamma_1^{p-1} F_{\gamma_1}(\gamma_1) d\gamma_1. \quad (6.48)$$

To estimate the ABER of DBPSK modulated signal, the values of  $p$  and  $q$  in Eq. (6.48) should be set to 1. The exponential function in the expression (6.48) is transformed to the Meijer G function ([Adamchik and Marichev, 1990](#), Eq. (11)) and the expression of CDF  $F_{\gamma_1}(\gamma_1)$  is substituted from Eq. (6.28) into Eq. (6.48). As a result, the ABER of the proposed system with DBPSK modulation can be expressed as

$$\begin{aligned} \bar{P}_b = & \frac{1}{2} \int_0^{\infty} G_{0,1}^{1,0} \left[ \gamma_1 \middle| \cdot \right] \frac{\xi^2 A}{2} \sum_{m=1}^{\beta} b_m \frac{\xi^2 A}{2} \times \\ & \sum_{m=1}^{\beta} b_m \frac{\xi^2 A}{2} \sum_{m=1}^{\beta} b_m \frac{\xi^2 A}{2} \sum_{m=1}^{\beta} b_m \times \\ & G_{5,13}^{12,1} \left[ \left( \frac{B^2 \gamma_1}{\bar{\gamma}_1} \right) \middle| \begin{array}{l} 1, 1 + \xi^2, 1 + \xi^2, 1 + \xi^2, 1 + \xi^2 \\ \xi^2, \alpha, m, \xi^2, \alpha, m, \xi^2, \alpha, m, \xi^2, \alpha, m, 0 \end{array} \right] d\gamma_1. \end{aligned} \quad (6.49)$$

After solving the above Eq. (6.49) using [[Adamchik and Marichev \(1990\)](#), Eq. (21)], we obtained the following expression for the ABER of the proposed system with DBPSK modulation

$$\begin{aligned} \overline{P}_b &= \frac{\xi^2 A}{4} \sum_{m=1}^{\beta} b_m \frac{\xi^2 A}{2} \sum_{m=1}^{\beta} b_m \frac{\xi^2 A}{2} \sum_{m=1}^{\beta} b_m \frac{\xi^2 A}{2} \sum_{m=1}^{\beta} b_m \times \\ &G_{6,13}^{12,2} \left[ \left( \frac{B^2 \gamma_1}{\overline{\gamma}_1} \right) \middle| \begin{array}{l} 1, 1 + \xi^2, 1 + \xi^2, 1 + \xi^2, 1 + \xi^2, 0 \\ \xi^2, \alpha, m, \xi^2, \alpha, m, \xi^2, \alpha, m, \xi^2, \alpha, m, 0 \end{array} \right]. \end{aligned} \quad (6.50)$$

As scenario one states, the proposed RIS-assisted RoFSO system also considers M-QAM modulation, for which the ABER  $\overline{P}_e$  is given as [Singh and Sappal (2019), Eq. (67)]

$$\overline{P}_b = \frac{(1 - \frac{1}{\sqrt{M}})}{\log_2 M} \int_0^\infty \text{erfc} \left( \sqrt{\frac{3 \log_2 M \gamma_1}{4(M-1)}} \right) f_{\gamma_1}(\gamma_1) d\gamma_1. \quad (6.51)$$

With the help of [wolfram (2001b), Eq. (06.27.26.0006.01)], *erfc* function is converted to equivalent Meijer G function and  $f_{\gamma}(\gamma)$  from Eq. (6.25) is substituted in Eq. 6.51, then we get  $\overline{P}_b$  as

$$\begin{aligned} \overline{P}_b &= \frac{1 - \frac{1}{\sqrt{M}}}{\log_2 M \sqrt{\pi}} \int_0^\infty G_{1,2}^{2,0} \left[ \left( \frac{3 \log_2 M \gamma_1}{4(M-1)} \right) \middle| \begin{array}{l} 1 \\ 0, \frac{1}{2} \end{array} \right] \times \\ &\frac{\xi^2 A}{2} \sum_{m=1}^{\beta} b_m \frac{\xi^2 A}{2} \sum_{m=1}^{\beta} b_m \frac{\xi^2 A}{2} \sum_{m=1}^{\beta} b_m \frac{\xi^2 A}{2} \sum_{m=1}^{\beta} b_m \times \\ &G_{4,12}^{12,0} \left[ \left( \frac{B^3 \gamma_1}{\overline{\gamma}_1} \right) \middle| \begin{array}{l} 1 + \xi^2, 1 + \xi^2, 1 + \xi^2, 1 + \xi^2 \\ \xi^2, \alpha, m, \xi^2, \alpha, m, \xi^2, \alpha, m, \xi^2, \alpha, m \end{array} \right] d\gamma_1. \end{aligned} \quad (6.52)$$

After applying Meijer-G integration identity from [Adamchik and Marichev (1990)], Eq. (21)] to solve Eq. (6.52), we obtain a closed-form expression for the ABER for M-QAM modulated signal as

$$\begin{aligned} \overline{P}_b &= \frac{1 - \frac{1}{\sqrt{M}}}{\log_2 M \sqrt{\pi}} \frac{\xi^2 A}{2} \sum_{m=1}^{\beta} b_m \frac{\xi^2 A}{2} \times \\ &\sum_{m=1}^{\beta} b_m \frac{\xi^2 A}{2} \sum_{m=1}^{\beta} b_m \frac{\xi^2 A}{2} \sum_{m=1}^{\beta} b_m \times \\ &G_{6,13}^{12,2} \left[ \left( \frac{4B^4(M-1)}{3\overline{\gamma} \log_2 M} \right) \middle| \begin{array}{l} \Delta_5 \\ \Delta_6 \end{array} \right], \end{aligned} \quad (6.53)$$

Where  $\Delta_5 = 1 + \xi^2, 1 + \xi^2, 1 + \xi^2, 1 + \xi^2, 1, 1/2$

$$\Delta_6 = \xi^2, \alpha, m, \xi^2, \alpha, m, \xi^2, \alpha, m, \xi^2, \alpha, m, 0.$$

## 6.6 Result and discussion

This section presents numerical results to illustrate the performance of the RIS-aided RoFSO system under investigation. In this system, the source and destination are situated at an equal distance, denoted as  $L$  kilometers, from the RIS, and an optical wavelength of 1550 nm is employed. For both scenarios, the system's sub-channels are characterized by a uniform refractive structure and index, represented as  $c_n^2$ , which remains constant throughout the transmission of a single symbol. The values of  $c_n^2$  for strong, moderate, and weak turbulence are taken as  $(5 \times 10^{-13}) m^{-\frac{2}{3}}$ ,  $(2.5 \times 10^{-13}) m^{-\frac{2}{3}}$ , and  $(10 \times 10^{-14}) m^{-\frac{2}{3}}$ , respectively.

In this proposed system, the diameter of the elements in the RIS structure is assumed to be the same as that of the receiver aperture, i.e.,  $D=1$  mm. We conducted an evaluation of the OP, ECC, and ABER for both scenarios employing DBPSK and M-QAM schemes. The selection of 16-QAM modulation is based on its suitability in scenarios where very high spectral efficiency is not an essential requirement. Higher-order QAM schemes are more susceptible to noise and interference, which results in higher error rates, making 16-QAM a preferable choice. To substantiate our theoretical derivations, we conducted Monte Carlo (MC) simulations utilizing MATLAB.

Figure 6.2 provides a graphical representation of the RIS-assisted RoFSO system's performance under varying turbulence conditions. In this depiction, the threshold SNR is fixed at 9 dB, the link length spans 1 km, and the scattering parameter, denoted as  $\rho$ , remains constant at 0.596. Notably, as the turbulence strength escalates, the OP exhibits an upward trend, signifying a decline in the system's performance. Figure 6.2 also elucidates that the system employing a single RIS outperforms the configuration with three RISs. For instance, in scenarios characterized by moderate turbulence, the 1 RIS system attains an OP of  $10^{-2}$  at an SNR of 35 dB. In stark contrast, the 3 RIS system necessitates a significantly higher SNR, exceeding 45 dB, to reach a similar OP threshold.

Figure 6.3 offers a comprehensive performance analysis of the RIS-assisted RoFSO system, focusing on varying RIS configurations. In this context, the link length is consistently set at 1 km, and the scattering parameter  $\rho$  maintains a fixed value of 0.596. Notably, as the average SNR experiences an increase, the ECC exhibits a corresponding augmentation. This figure highlights the comparative ECC performance between

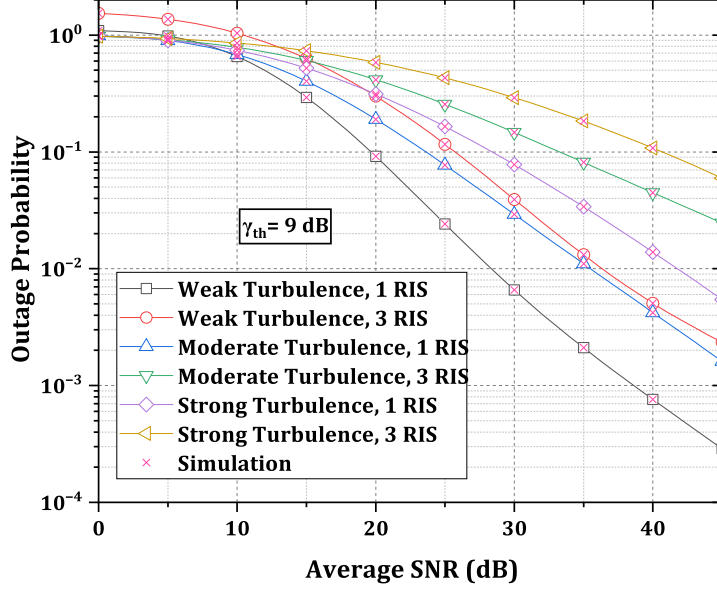


**Figure 6.2:** The results of the OP analysis for the RIS-aided RoFSO system under various turbulence conditions and with varying numbers of RISs, in terms of the average SNR.

two distinct system configurations: the 1 RIS setup and the 3 RIS configuration. It is evident from the results that when the single RIS configuration is technically feasible, it consistently outperforms the system employing 3 RISs. To illustrate, to achieve an ECC of 10 bits per second per Hertz (bits/sec/Hz), the 1 RIS system effectively operates with an SNR of 35 dB. In stark contrast, the 3 RIS system necessitates a significantly higher SNR, exceeding 40 dB, highlighting a notable performance gap between these configurations.

The ECC performance assessment of the RIS-assisted RoFSO system, incorporating varying turbulence conditions and the presence of different RIS configurations, is meticulously detailed in Figure 6.4. Notably, this analysis maintains a consistent 1 km link length alongside a fixed scattering parameter  $\rho$  value of 0.596. As the system's average SNR is systematically elevated, a corresponding increase is observed in the Effective Channel Capacity (ECC). Of particular interest in this Figure 6.4 is the performance comparison between the 1 RIS setup and the 3 RIS system, focusing on ECC while considering different turbulence conditions. The results illustrate that, under most turbulence scenarios, the 1 RIS configuration consistently outperforms

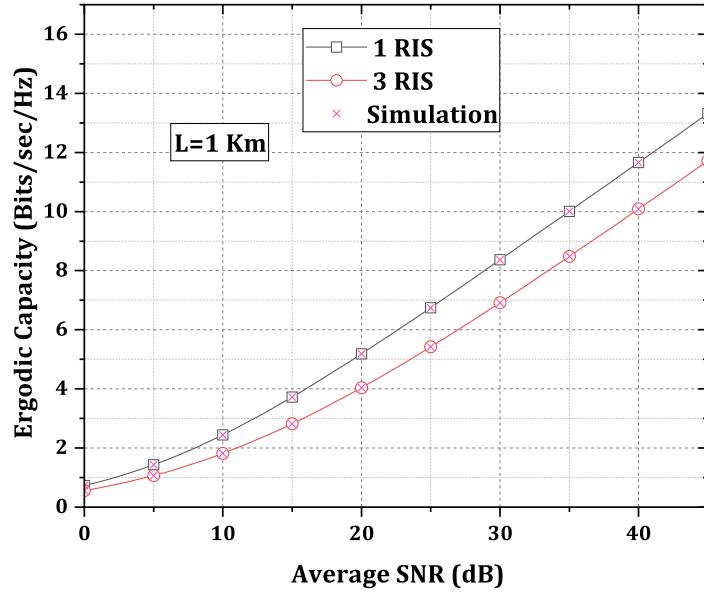


Figure 6.3: ECC against average SNR for various numbers of RISs.

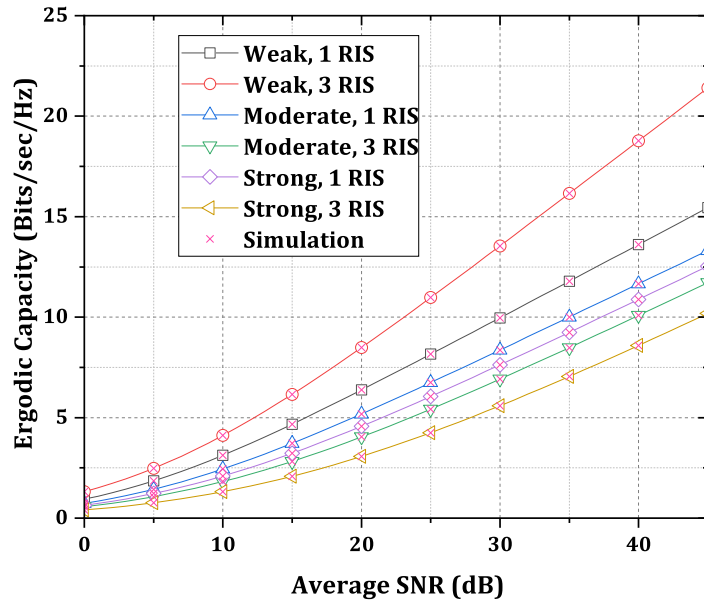
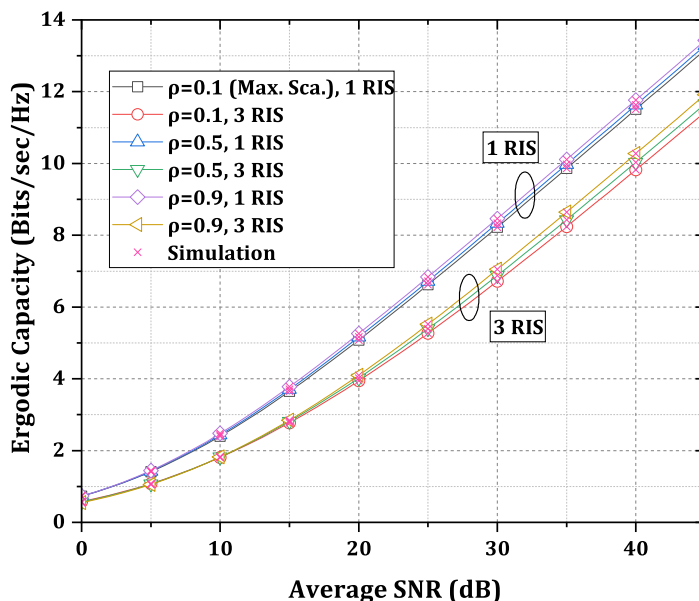


Figure 6.4: ECC performance against the average SNR for different turbulence conditions with various number of RISs.



**Figure 6.5:** ECC performance against average SNR for various scattering errors and numbers of RISs.

the 3 RIS system when it is technically feasible to deploy a single RIS. An exception arises in weak turbulence, where the 3 RIS system exhibits superior ECC performance compared to the single RIS configuration. This anomaly can be attributed to the absence of a direct link between the initial RIS and the destination, resulting in an outcome consistent with previously documented findings in [Wang \*et al.\* \(2022\)](#). In the challenging scenario of strong turbulence, the 1 RIS system can achieve an ECC of 10 bits per second per Hertz (bits/sec/Hz) with an SNR of 37 dB. Conversely, the 3 RIS system necessitates a substantially higher SNR, exceeding 45 dB, indicative of a notable performance distinction between these configurations.

Figure 6.5 is dedicated to the performance evaluation of the RIS-enhanced RoFSO system, considering variations in scattering error and different RIS configurations. The analysis retains a fixed link length of 1 km, set against moderate turbulence. Figure 6.5 precisely juxtaposes the ECC performance of the 1 RIS and 3 RIS systems within different scattering error levels. In comparing the SNR requirements necessary to attain a 10 bits per second per Hertz (bits/sec/Hz) ECC, the results elucidate that the system's ECC performance is notably less susceptible to scattering

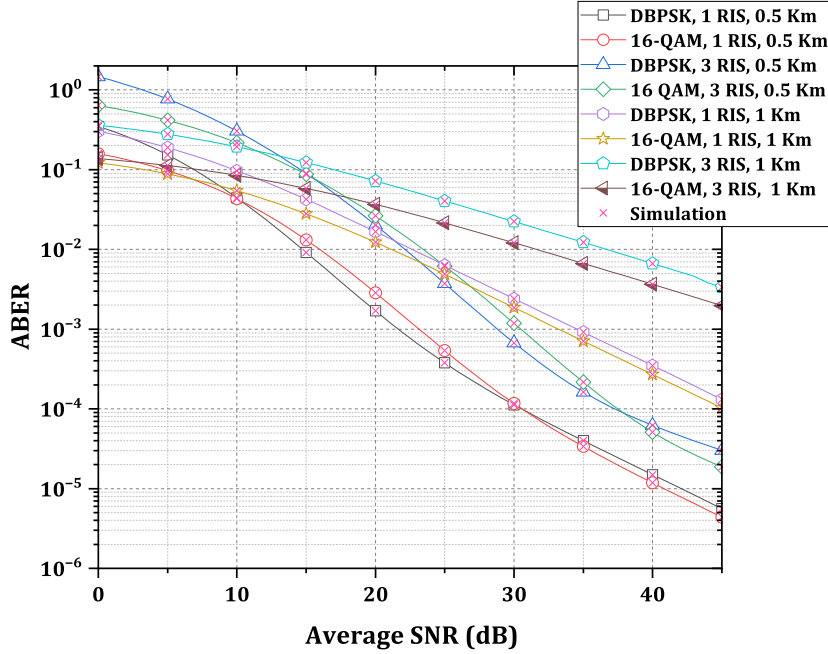


**Figure 6.6:** The performance of the proposed RIS-assisted RoFSO system in terms of its ABER with respect to average SNR values, considering different communication distances, modulation schemes, and numbers of RISs.

errors when contrasted with its sensitivity to turbulence conditions. Specifically, to achieve the specified ECC, the 3 RIS system necessitates SNRs of 38 dB, 40 dB, and 41 dB in scenarios characterized by low scattering conditions ( $\rho = 0.9$ ), moderate scattering ( $\rho = 0.5$ ), and maximum scattering conditions ( $\rho = 0.1$ ), respectively. This observation underscores the relatively milder impact of scattering errors compared to turbulence on the ECC performance of the system.

Figure 6.6 takes a detailed look at the ABER performance within the context of the RIS-aided RoFSO system. It considers various parameters, including link lengths, modulation techniques, and the number of RISs. These evaluations are conducted against a backdrop of moderate turbulence conditions, with a scattering error parameter ( $\rho$ ) fixed at 0.596. The findings conclusively reveal that, regardless of link length and modulation technique, the 1 RIS configuration consistently outperforms the 3 RIS system. As for the modulation techniques, it's noteworthy that 16-QAM tends to perform better in almost all scenarios, except for the 1 RIS system operating with a 0.5 km link length. A more in-depth examination of the ABER performance further discloses that, within the framework of the 3 RIS system, the 1 km link length

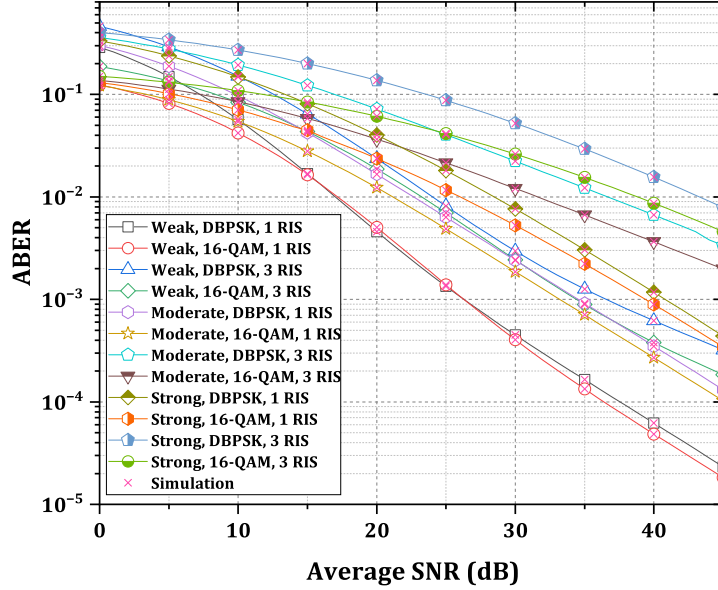


**Figure 6.7:** The performance of the RIS-assisted RoFSO system in terms of ABER for different modulation schemes, turbulence conditions and the number of RISs.

exhibits superior performance compared to the 0.5 km link length. This superiority is observed in cases with an average SNR of up to 15 dB. However, when the average SNR values surpass 20 dB, the 0.5 km link length proves more advantageous. In a final comparison, focusing on the ABER performance of the 16-QAM modulation technique for the 3 RIS system, it's evident that achieving an ABER of  $10^{-2}$  demands a 24 dB SNR for the 0.5 km link length system. In contrast, the 1 km link length system requires a significantly higher 32 dB SNR to meet the same ABER.

Figure 6.7 provides an insightful comparison of the ABER performance in the context of 1 RIS and 3 RIS systems. These comparisons are conducted across varying turbulence conditions and modulation techniques, thereby offering a comprehensive view of system performance. The depicted trends indicate that as turbulence strength increases, the ABER also rises. This direct relationship implies that heightened turbulence is associated with a noticeable degradation in system performance. An essential observation from the figure is that, across both modulation techniques and in all three turbulence conditions, the 1 RIS system consistently outperforms its 3 RIS counterparts. Notably, 16-QAM consistently exhibits superior performance for the

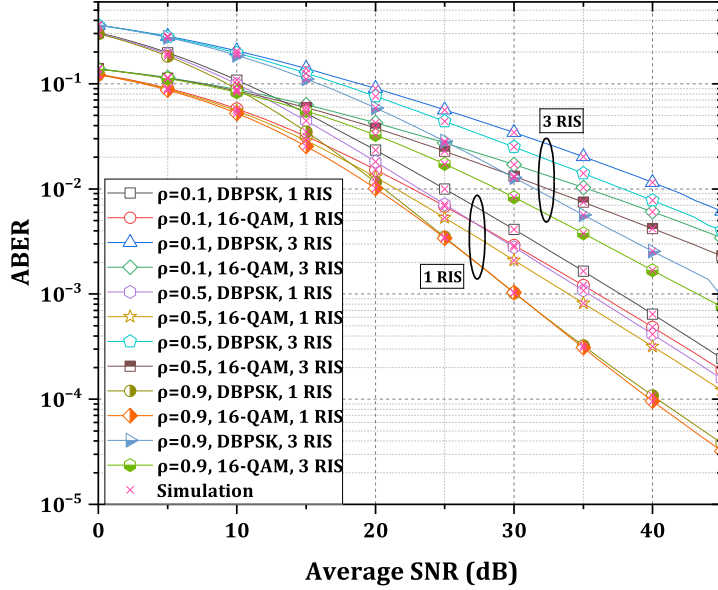


**Figure 6.8:** ABER performance against SNR for various modulation schemes and numbers of RISs, under different levels of scattering error.

modulation technique compared to DBPSK. However, it's important to highlight an exception: within the context of the 1 RIS 16 QAM system, there is a narrow SNR range of 20 dB to 25 dB where DBPSK demonstrates slightly better performance than 16-QAM.

Furthermore, the turbulence conditions are pivotal in influencing the system's ABER performance. This is particularly evident in the example of the 16-QAM 3 RIS system, where, under weak turbulence, achieving a ABER of  $10^{-3}$  necessitates an average SNR of 35 dB. Conversely, a considerably higher average SNR exceeding 45 dB is required to attain the same ABER threshold for the moderate turbulence setting within the same system.

Figure 6.8 offers a detailed insight into the ABER performance exhibited by both 1 RIS and 3 RIS systems across various scattering error conditions and modulation techniques. An overarching observation is that throughout the range of 15 dB average SNR to 45 dB SNR, the 1 RIS system consistently outperforms the 3 RIS system. When considering modulation techniques, 16-QAM consistently demonstrates superior performance compared to DBPSK, regardless of the scattering conditions and whether

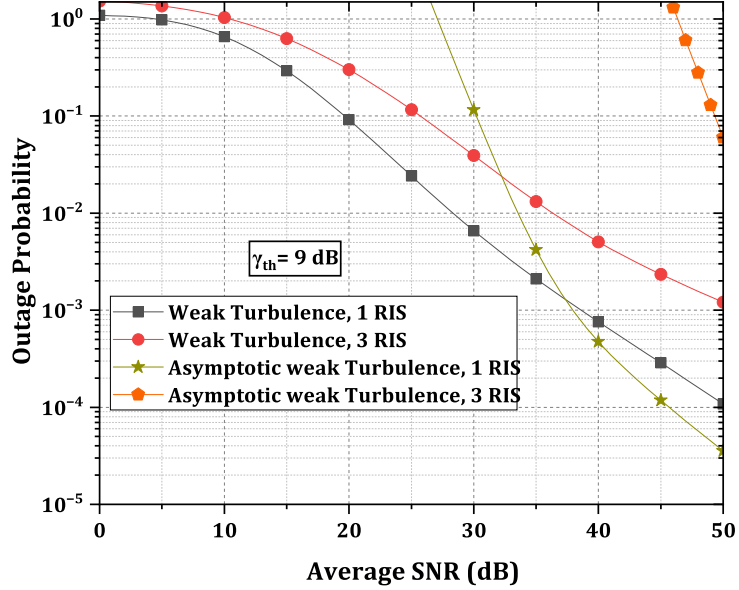


**Figure 6.9:** The findings of the OP exact and asymptotic analysis, considering weak turbulence condition and varying number of RISs, are presented in terms of the average SNR for the RIS-aided RoFSO system.

in the context of 1 RIS or 3 RIS systems. It is worth noting that the influence of scattering error on the system’s ABER performance appears to be notably less substantial than the impact of turbulence. To provide an example, within a 16-QAM 3 RIS system, an ABER of  $10^{-2}$  is achieved with 35 dB SNR under maximum scattering error conditions ( $\rho = 0.1$ ), 32 dB SNR with moderate scattering error conditions ( $\rho = 0.5$ ), and 28 dB SNR with minimal scattering error conditions ( $\rho = 0.9$ ).

Figure 6.9 offers a comparative analysis between the exact OP and the asymptotic OP in the envisioned RIS-aided RoFSO system, specifically under weak turbulence conditions. This graphical representation sheds light on the OP’s characteristics concerning the incremental growth of SNR. A discernible trend emerges as the SNR escalates, with the asymptotic OP gradually converging towards the exact OP.

## 6.7 Summary

This chapter scrutinizes the operational efficacy of RIS-empowered RoFSO systems in M-distributed turbulence, employing heterodyne detection. Analytical expressions for PDF and CDF are derived concerning the end-to-end SNR, utilizing the Meijer-G

function. DBPSK and M-QAM modulation techniques are examined. The chapter proceeds to evaluate and compare the performance of a solitary RIS-supported RoFSO system with that of a three RIS-supported RoFSO system, using metrics such as OP, ECC, and ABER. The results indicate that RIS technology exhibits promising capabilities for ensuring robust RoFSO communication, even under challenging Non-LOS scenarios, particularly in vehicular communication applications. Notably, it is observed that provided the single RIS system maintains a viable channel link, it generally outperforms the three RIS system. Nevertheless, the efficacy of the proposed system declines with an increased number of RISs between the source and destination due to cascading channel coefficients. However, should the single RIS system encounter issues maintaining the communication link, deploying three RISs becomes a viable option for Vehicle-to-Infrastructure (V2I) connectivity.

# Chapter 7

## Conclusions and Future Scope

### 7.1 Conclusions

This research delves into analysing RoFSO systems, focusing on their performance, challenges, and limitations. The study derives analytical channel models under the effect of turbulence, atmospheric attenuation, and pointing errors. It considers various environmental conditions, including haze, fog, and clear air, to assess RoFSO systems comprehensively. An essential aspect of this research is the utilisation of Reconfigurable Intelligent Surfaces (RIS) to address the "skip zone" issue of FSOs.

This research work analysed the ABER performance of DPSK-based RoFSO systems. Spatial diversity at both ends, that is, MIMO is utilised as a mitigation technique, and enhancement in performance of the RoFSO system is shown. The investigation employs OC and EGC combining techniques for MIMO systems. In the following work, two distinct coding techniques, BCH and RS, are used to enhance the performance of the BPSK OFDM RoFSO system. The ABER is derived in terms of Meijer-g function for considered M-distributed channel. It is shown that the BCH-coded system performs better than uncoded and RS-coded systems. The RoFSO system performance is analysed for weather, atmospheric turbulence, pointing error, and scattering parameter conditions.

Further, to mitigate the skip zone problem in RoFSO communication, RIS is introduced. The three modulation techniques considered were NBFSK, CBPSK, and M-QAM. Heterodyne detection is considered. In the following work, previous work is extended with a multi-RIS assisted FSO system, especially for vehicular communication, and analysed. Here, the two scenarios are considered with single RIS and multi-RIS. Here, the DBPSK and M-QAM modulation have been used. The perfor-

mance is analysed through OP, ECC and ABER performance metrics. OP, ECC and ABER are derived in terms of Meijer-g function for considered M-distributed channel. The system performance is analysed for link length, atmospheric turbulence, and scattering parameter conditions. It is shown that communication is possible without clear LOS with the help of RIS for RoFSO, and the multi-RIS-aided RoFSO system can be utilised for vehicular communication.

## 7.2 Future Scope

RoFSO encompasses diverse domains that offer avenues for continued investigation, and this study has laid the foundation for the following prospective areas of exploration. Other than BCH and RS error-correcting codes, such as LDPC or Turbo codes, can be explored to enhance the RoFSO communication system's performance. RIS can be used for the RoFSO communication system application in satellite-to-ground communication. The Doppler effect can be considered, especially for high-speed vehicles in the RoFSO communication application for vehicular communication. Furthermore, the energy harvesting technique, Simultaneous Light Information and Power Transfer (SLIPT), can be implemented within the RoFSO system to explore energy harvesting possibilities, particularly in Internet of Things (IoT) applications.

# Bibliography

- Abdelhady, A. M., A. K. S. Salem, O. Amin, B. Shihada, and M.-S. Alouini** (2020). Visible light communications via intelligent reflecting surfaces: Metasurfaces vs mirror arrays. *IEEE Open Journal of the Communications Society*, **2**, 1–20.
- Adamchik, V. and O. Marichev**, The algorithm for calculating integrals of hypergeometric type functions and its realization in REDUCE system. *In Proceedings of the international symposium on Symbolic and algebraic computation*. 1990.
- Aghaei, M. R., A. A. Hemmatyar, A. Chamanmotlagh, and M. Fouladian** (2020). Analysis of adaptive multi-rate fso/rf hybrid systems using malaga-m distribution model in turbulent channels. *Journal of Modern Optics*, **67**(13), 1159–1169.
- Ajam, H., M. Naja, V. Jamali, and R. Schober**, Channel modeling for irs-assisted fso systems. *In 2021 IEEE Wireless Communications and Networking Conference (WCNC)*. IEEE, 2021a.
- Ajam, H., M. Naja, V. Jamali, and R. Schober**, Channel modeling for irs-assisted fso systems. *In 2021 IEEE Wireless Communications and Networking Conference (WCNC)*. 2021b.
- Ajam, H., M. Najafi, V. Jamali, B. Schmauss, and R. Schober** (2022). Modeling and design of irs-assisted multilink fso systems. *IEEE Transactions on Communications*, **70**(5), 3333–3349.
- Ajewole, B. D., K. O. Odeyemi, P. A. Owolawi, and V. M. Srivastava**, Coded bpsk ofdm-fso over strong turbulence channel. *In 2019 International Conference on Advances in Big Data, Computing and Data Communication Systems (icABCD)*. IEEE, 2019.

- Al-Khafaji, H. M., S. Aljunid, A. Amphawan, H. Fadhil, and A. Safar** (2013). Reducing ber of spectral-amplitude coding optical code-division multiple-access systems by single photodiode detection technique. *Journal of the European Optical Society-Rapid Publications*, **8**.
- Andrews, L. C. and R. L. Phillips** (2005). Laser beam propagation through random media. *Laser Beam Propagation Through Random Media: Second Edition*.
- Ansari, I. S., F. Yilmaz, and M.-S. Alouini** (2015). Performance analysis of free-space optical links over Málaga ( $\mathcal{M}$ ) turbulence channels with pointing errors. *IEEE Transactions on Wireless Communications*, **15**(1), 91–102.
- Arnon, S.** (2003). Optimization of urban optical wireless communication systems. *IEEE Transactions on Wireless Communications*, **2**(4), 626–629.
- Arnon, S., J. Barry, G. Karagiannidis, R. Schober, and M. Uysal**, *Advanced optical wireless communication systems*. Cambridge university press, 2012.
- Arnon, S., M. Uysal, Z. Ghassemlooy, Z. Xu, and J. Cheng** (2015). Guest editorial: Optical wireless communications. *IEEE journal on selected areas in communications*, **33**(9), 1733–1737.
- Attaul Mustafa, H., M. A. Imran, M. Zeeshan Shakir, A. Imran, and R. Tafazolli** (2016). Separation framework: An enabler for cooperative and d2d communication for future 5g networks. *arXiv e-prints*, arXiv-1604.
- Balaji, K. and K. Prabu** (2018a). Ber analysis of relay assisted psk with ofdm rofso system over malaga distribution including pointing errors under various weather conditions. *Optics Communications*, **426**, 187–193.
- Balaji, K. and K. Prabu** (2018b). Performance evaluation of fso system using wavelength and time diversity over malaga turbulence channel with pointing errors. *Optics Communications*, **410**, 643–651.
- Basar, E.** (2020). Reconfigurable intelligent surface-based index modulation: A new beyond mimo paradigm for 6g. *IEEE Transactions on Communications*, **68**(5), 3187–3196.

- Basar, E.** and **H. V. Poor** (2021). Present and future of reconfigurable intelligent surface-empowered communications [perspectives]. *IEEE Signal Processing Magazine*, **38**(6), 146–152.
- Bekkali, A., C. B. Naila, K. Kazaura, K. Wakamori,** and **M. Matsumoto** (2010). Transmission analysis of ofdm-based wireless services over turbulent radio-on-fso links modeled by gamma-gamma distribution. *IEEE photonics journal*, **2**(3), 510–520.
- Bhatnagar, M. R.** and **Z. Ghassemlooy** (2016). Performance analysis of gamma-gamma fading fso mimo links with pointing errors. *Journal of Lightwave technology*, **34**(9), 2158–2169.
- Boluda-Ruiz, R., A. García-Zambrana, C. Castillo-Vázquez, B. Castillo-Vázquez,** and **S. Hranilovic** (2017). Outage performance of exponentiated weibull fso links under generalized pointing errors. *Journal of Lightwave Technology*, **35**(9), 1605–1613.
- Bonetto, E., L. Chiaraviglio, D. Cuda, G. A. G. Castillo,** and **F. Neri**, Optical technologies can improve the energy efficiency of networks. *In 2009 35th European conference on optical communication*. IEEE, 2009.
- Borges, R. M., C. H. de Souza Lopes, E. S. Lima, M. A. de Oliveira, M. S. B. Cunha, L. C. Alexandre, L. G. da Silva, L. A. M. Pereira, D. H. Spadoti, M. A. Romero, *et al.* (2021). Integrating optical and wireless techniques towards novel fronthaul and access architectures in a 5g nr framework. *Applied Sciences*, **11**(11), 5048.**
- Boulogeorgos, A.-A. A., N. D. Chatzidiamantis, H. G. Sandalidis, A. Alexiou,** and **M. Di Renzo** (2022). Cascaded composite turbulence and misalignment: Statistical characterization and applications to reconfigurable intelligent surface-empowered wireless systems. *IEEE Transactions on Vehicular Technology*, **71**(4), 3821–3836.
- Brychkov, Y. A., O. Marichev,** and **A. Prudnikov** (1986). Integrals and series, vol 3: more special functions. *ed: Gordon and Breach science publishers*.

- Chadha, D.**, *Terrestrial wireless optical communication*. McGraw Hill Professional, 2013.
- Chan, V.** (1982). Coding for the turbulent atmospheric optical channel. *IEEE transactions on Communications*, **30**(1), 269–275.
- Chan, V. W.** (2006). Free-space optical communications. *Journal of Lightwave technology*, **24**(12), 4750–4762.
- Chapala, V. K.** and **S. M. Zafaruddin** (2021). Ris-assisted multihop fso/rf hybrid system for vehicular communications over generalized fading. *arXiv preprint arXiv:2112.12944*.
- Chen, Y.**, **Y. Wang**, **J. Zhang**, and **Z. Li** (2020). Resource allocation for intelligent reflecting surface aided vehicular communications. *IEEE Transactions on Vehicular Technology*, **69**(10), 12321–12326.
- Chiani, M.**, **D. Dardari**, and **M. K. Simon** (2003). New exponential bounds and approximations for the computation of error probability in fading channels. *IEEE Transactions on Wireless Communications*, **2**(4), 840–845.
- Choi, J.**, **J. Kim**, **J. H. Cho**, and **J. S. Lehnert** (2021). Widely-linear nyquist criteria for dft-spread ofdm of constellation-rotated pam symbols. *IEEE Transactions on Communications*, **69**(5), 2909–2922.
- Chowdhury, M. Z.**, **M. K. Hasan**, **M. Shahjalal**, **M. T. Hossan**, and **Y. M. Jang** (2020). Optical wireless hybrid networks: Trends, opportunities, challenges, and research directions. *IEEE Communications Surveys & Tutorials*, **22**(2), 930–966.
- Chowdhury, M. Z.**, **M. T. Hossan**, **A. Islam**, and **Y. M. Jang** (2018). A comparative survey of optical wireless technologies: Architectures and applications. *IEEE Access*, **6**, 9819–9840.
- Dabiri, M. T.**, **M. J. Saber**, and **S. M. S. Sadough** (2017). On the performance of multiplexing fso mimo links in log-normal fading with pointing errors. *Journal of Optical Communications and Networking*, **9**(11), 974–983.

- Dey, K. C., A. Rayamajhi, M. Chowdhury, P. Bhavsar, and J. Martin** (2016). Vehicle-to-vehicle (v2v) and vehicle-to-infrastructure (v2i) communication in a heterogeneous wireless network—performance evaluation. *Transportation Research Part C: Emerging Technologies*, **68**, 168–184.
- Di Renzo, M., K. Ntontin, J. Song, F. H. Danufane, X. Qian, F. Lazarakis, J. De Rosny, D.-T. Phan-Huy, O. Simeone, R. Zhang, et al.** (2020). Reconfigurable intelligent surfaces vs. relaying: Differences, similarities, and performance comparison. *IEEE Open Journal of the Communications Society*, **1**, 798–807.
- Ding, C.** (2015). Parameters of several classes of bch codes. *IEEE Transactions on Information Theory*, **61**(10), 5322–5330.
- e Sustainability Initiative, G. et al.** (2008). Smart 2020: Enabling the low carbon economy in the information age, united states report addendum. *Prepared by Boston Consulting Group for GeSI. Accessed December, 29, 2009.*
- ElMossallamy, M. A., H. Zhang, L. Song, K. G. Seddik, Z. Han, and G. Y. Li** (2020). Reconfigurable intelligent surfaces for wireless communications: Principles, challenges, and opportunities. *IEEE Transactions on Cognitive Communications and Networking*, **6**(3), 990–1002.
- Fan, Y. and R. J. Green** (2007). Comparison of pulse position modulation and pulse width modulation for application in optical communications. *Optical Engineering*, **46**(6), 065001.
- Farid, A. A. and S. Hranilovic** (2007). Outage capacity optimization for free-space optical links with pointing errors. *Journal of Lightwave technology*, **25**(7), 1702–1710.
- Gao, Z., M. Eisen, and A. Ribeiro**, Optimal wdm power allocation via deep learning for radio on free space optics systems. *In 2019 IEEE Global Communications Conference (GLOBECOM)*. IEEE, 2019.
- Garlinska, M., A. Pregowska, K. Masztalerz, and M. Osial** (2020). From mirrors to free-space optical communication—historical aspects in data transmission. *Future Internet*, **12**(11), 179.

- Ghassemlooy, Z., S. Arnon, M. Uysal, Z. Xu, and J. Cheng** (2015). Emerging optical wireless communications—advances and challenges. *IEEE journal on selected areas in communications*, **33**(9), 1738–1749.
- Ghassemlooy, Z., A. Hayes, N. L. Seed, and E. Kaluarachchi** (1998). Digital pulse interval modulation for optical communications. *IEEE Communications Magazine*, **36**(12), 95–99.
- Ghassemlooy, Z., W. Popoola, and S. Rajbhandari**, *Optical wireless communications: system and channel modelling with Matlab®*. CRC press, 2019.
- Ghassemlooy, Z. and W. O. Popoola**, *Terrestrial free-space optical communications*. InTech, 2010.
- Ghosh, S.**, *Emergent technology based Radio Access Network (RAN) design framework for next generation broadband wireless systems*. The University of Texas at Arlington, 2004.
- Gradshteyn, I. S. and I. M. Ryzhik**, *Table of integrals, series, and products*. Academic press, 2014.
- Gupta, N., A. Dixit, V. K. Jain, et al.**, Performance analysis of bch and repetition codes in gamma-gamma faded fso link. *In 2019 National Conference on Communications (NCC)*. IEEE, 2019.
- Hassan, M. Z., M. J. Hossain, J. Cheng, and V. C. Leung** (2019). Subcarrier intensity modulated optical wireless communications: a survey from communication theory perspective. *ZTE communications*, **14**(2), 2–12.
- Heatley, D. J., D. R. Wisely, I. Neild, and P. Cochrane** (1998). Optical wireless: The story so far. *IEEE communications magazine*, **36**(12), 72–74.
- Henniger, H. and O. Wilfert** (2010). An introduction to free-space optical communications. *Radioengineering*, **19**(2).
- Hou, J. and D. C. O’Brien** (2006). Vertical handover-decision-making algorithm using fuzzy logic for the integrated radio-and-ow system. *IEEE Transactions on Wireless Communications*, **5**(1), 176–185.

- Ijaz, A., L. Zhang, M. Grau, A. Mohamed, S. Vural, A. U. Quddus, M. A. Imran, C. H. Foh, and R. Tafazolli** (2016). Enabling massive iot in 5g and beyond systems: Phy radio frame design considerations. *IEEE Access*, **4**, 3322–3339.
- Jahid, A., M. H. Alsharif, and T. J. Hall** (2022). A contemporary survey on free space optical communication: Potentials, technical challenges, recent advances and research direction. *Journal of Network and Computer Applications*, **200**, 103311.
- Játiva, P. P., F. Seguel, and P. Adasme**, Evaluation of intelligent reflecting surfaces for diffuse visible light communications link. *In 2020 IEEE Latin-American Conference on Communications (LATINCOM)*. IEEE, 2020.
- Jia, H., J. Zhong, M. N. Janardhanan, and G. Chen**, Ergodic capacity analysis for fso communications with uav-equipped irs in the presence of pointing error. *In 2020 IEEE 20th International Conference on Communication Technology (ICCT)*. IEEE, 2020.
- Juarez, J. C., A. Dwivedi, A. R. Hammons, S. D. Jones, V. Weerackody, and R. A. Nichols** (2006). Free-space optical communications for next-generation military networks. *IEEE Communications Magazine*, **44**(11), 46–51.
- Jurado-Navas, A., J. M. G. Balsells, J. F. Paris, M. Castillo-Vázquez, and A. Puerta-Notario** (2011*a*). General analytical expressions for the bit error rate of atmospheric optical communication systems. *Optics letters*, **36**(20), 4095–4097.
- Jurado-Navas, A., J. Garrido-Balsells, J. F. Paris, M. Castillo-Vazquez, and A. Puerta-Notario**, Further insights on Málaga distribution for atmospheric optical communications. *In 2012 International Workshop on Optical Wireless Communications (IWOW)*. IEEE, 2012*a*.
- Jurado-Navas, A., J. M. Garrido-Balsells, J. F. Paris, M. Castillo-Vázquez, and A. Puerta-Notario** (2012*b*). Impact of pointing errors on the performance of generalized atmospheric optical channels. *Optics Express*, **20**(11), 12550–12562.
- Jurado-Navas, A., J. M. Garrido-Balsells, J. F. Paris, A. Puerta-Notario, and J. Awrejcewicz** (2011*b*). A unifying statistical model for atmospheric optical

scintillation. *Numerical simulations of physical and engineering processes*, **181**(8), 181–205.

**Kanno, A., K. Inagaki, I. Morohashi, T. Sakamoto, T. Kuri, I. Hosako, T. Kawanishi, Y. Yoshida, and K.-i. Kitayama** (2011). 40 gb/s w-band (75–110 ghz) 16-qam radio-over-fiber signal generation and its wireless transmission. *Optics Express*, **19**(26), B56–B63.

**Karp, D., E. Prilepkina, et al.** (2016). Hypergeometric differential equation and new identities for the coefficients of nørlund and bührling. *SIGMA. Symmetry, Integrability and Geometry: Methods and Applications*, **12**, 052.

**Kashani, M. A., M. Uysal, and M. Kavehrad** (2015). A novel statistical channel model for turbulence-induced fading in free-space optical systems. *Journal of Lightwave Technology*, **33**(11), 2303–2312.

**Kaur, K. and A. Nain** (2022). An improved rofso network based on mbmd scheme under hazy weather conditions. *Journal of Optics*, 1–7.

**Kaur, P., V. K. Jain, and S. Kar** (2014). Performance analysis of fso array receivers in presence of atmospheric turbulence. *IEEE Photonics Technology Letters*, **26**(12), 1165–1168.

**Kaushal, H., V. Jain, and S. Kar**, *Free space optical communication*. Springer, 2017.

**Kaushal, H. and G. Kaddoum** (2016). Optical communication in space: Challenges and mitigation techniques. *IEEE communications surveys & tutorials*, **19**(1), 57–96.

**Kazaura, K., K. Wakamori, M. Matsumoto, T. Higashino, K. Tsukamoto, and S. Komaki** (2010). Rofso: a universal platform for convergence of fiber and free-space optical communication networks. *IEEE Communications Magazine*, **48**(2), 130–137.

**Khalighi, M. A. and M. Uysal** (2014). Survey on free space optical communication: A communication theory perspective. *IEEE communications surveys & tutorials*, **16**(4), 2231–2258.

- Khan, M., K. Rao, S. Amuru, and K. Kuchi** (2020). Low papr reference signal transceiver design for 3gpp 5g nr uplink. *EURASIP Journal on Wireless Communications and Networking*, **2020**(1), 1–28.
- Khare, S. and N. Sahayam** (2012). Analysis of free space optical communication system for different atmospheric conditions and modulation techniques.
- Kim, J.-M., J.-H. Lee, Y. Lee, H.-S. Cha, H. Park, J. Sim, C. Kim, and Y.-C. Ko**, Experimental demonstration of rofso transmission combining wlan standard and wdm-fso over 100m distance. In *IEEE INFOCOM 2022-IEEE Conference on Computer Communications Workshops (INFOCOM WKSHPS)*. IEEE, 2022.
- Krishnan, P., U. Jana, and B. Kanekal Ashokkumar** (2018). Asymptotic bit-error rate analysis of quadrature amplitude modulation and phase-shift keying with ofdm rofso over m turbulence in the presence of pointing errors. *IET Communications*, **12**(16), 2046–2051.
- Krishnan, P. and D. S. Kumar** (2014). Performance analysis of free-space optical systems employing binary polarization shift keying signaling over gamma-gamma channel with pointing errors. *Optical Engineering*, **53**(7), 076105.
- Kschischang, F. R.** (2017). The complementary error function. *Online, April*.
- Kumar, A. and P. Krishnan** (2020a). Performance analysis of rofso links with spatial diversity over combined channel model for 5g in smart city applications. *Optics Communications*, **466**, 125600.
- Kumar, L. B. and P. Krishnan** (2020b). Multi-hop convergent fso-uwoc system to establish a reliable communication link between the islands. *Optics Communications*, 126107.
- Kumar, N. and V. Khandelwal**, Simulation of mimo-fso system with gamma-gamma fading under different atmospheric turbulence conditions. In *2019 International Conference on Signal Processing and Communication (ICSC)*. IEEE, 2019.
- Lee, E. J. and V. W. Chan** (2004). Part 1: Optical communication over the clear turbulent atmospheric channel using diversity. *IEEE journal on selected areas in communications*, **22**(9), 1896–1906.

- Li, R., T. Chen, L. Fan, and A. Dang** (2019). Performance analysis of a multiuser dual-hop amplify-and-forward relay system with fso/rf links. *Journal of Optical Communications and Networking*, **11**(7), 362–370.
- Lin, S. and D. J. Costello**, *Error control coding*, volume 2. Prentice hall New York, 2001.
- Liu, X.** (2015). Secrecy capacity of wireless channels subject to log-normal fading. *Security and Communication Networks*, **8**(1), 25–35.
- Long, R. K.** (1963). Atmospheric attenuation of ruby lasers. *Proceedings of the IEEE*, **51**(5), 859–860.
- MacWilliams, F. J. and N. J. A. Sloane**, *The theory of error correcting codes*, volume 16. Elsevier, 1977.
- Majumdar, A. K., Z. Ghassemlooy, and A. A. B. Raj**, *Principles and applications of free space optical communications*. Institution of Engineering and Technology, 2019.
- Mensi, N., D. B. Rawat, and E. Balti**, Physical layer security for v2i communications: Reflecting surfaces vs. relaying. In *2021 IEEE Global Communications Conference (GLOBECOM)*. IEEE, 2021.
- Mishra, A. and R. K. Giri**, Performance analysis of different modulation techniques in sim based fso using different receivers over turbulent channel. In *2018 International Conference on Communication, Computing and Internet of Things (IC3IoT)*. 2018.
- Mohsan, S. A. H., M. A. Khan, and H. Amjad** (2023). Hybrid fso/rf networks: A review of practical constraints, applications and challenges. *Optical Switching and Networking*, **47**, 100697.
- Muhammad, S. S., B. Flecker, E. Leitgeb, and M. Gebhart** (2007). Characterization of fog attenuation in terrestrial free space optical links. *Optical engineering*, **46**(6), 066001–066001.

- Naila, C. B., K. Wakamori, and M. Matsumoto** (2011). Transmission analysis of m-ary phase shift keying multiple-subcarrier modulation signals over radio-on-free-space optical channel with aperture averaging. *Optical Engineering*, **50**(10), 105006.
- Najafi, M., V. Jamali, R. Schober, and H. V. Poor** (2020). Physics-based modeling and scalable optimization of large intelligent reflecting surfaces. *IEEE Transactions on Communications*, **69**(4), 2673–2691.
- Najafi, M., B. Schmauss, and R. Schober** (2021). Intelligent reflecting surfaces for free space optical communication systems. *IEEE transactions on communications*, **69**(9), 6134–6151.
- Najafi, M. and R. Schober**, Intelligent reflecting surfaces for free space optical communications. *In 2019 IEEE Global Communications Conference (GLOBECOM)*. IEEE, 2019.
- Ndjiongue, A. R., T. Ngatched, O. A. Dobre, A. G. Armada, and H. Haas** (2021a). Performance analysis of ris-based nt-fso link over gg turbulence with pointing errors. *arXiv preprint arXiv:2102.03654*.
- Ndjiongue, A. R., T. M. Ngatched, O. A. Dobre, A. G. Armada, and H. Haas** (2021b). Analysis of ris-based terrestrial-fso link over gg turbulence with distance and jitter ratios. *Journal of Lightwave Technology*, **39**(21), 6746–6758.
- Ndjiongue, A. R., T. M. Ngatched, O. A. Dobre, and H. Haas** (2021c). Reconfigurable intelligent surface-based vlc receivers using tunable liquid-crystals: The concept. *Journal of Lightwave Technology*, **39**(10), 3193–3200.
- Ndjiongue, A. R., T. M. Ngatched, O. A. Dobre, and H. Haas** (2021d). Toward the use of re-configurable intelligent surfaces in vlc systems: Beam steering. *IEEE Wireless Communications*, **28**(3), 156–162.
- Ninos, M. P., H. E. Nistazakis, E. Leitgeb, and G. S. Tombras** (2019). Spatial diversity for qam ofdm rofso links with nonzero boresight pointing errors over atmospheric turbulence channels. *Journal of modern optics*, **66**(3), 241–251.

- Nistazakis, H., A. Stassinakis, H. Sandalidis, and G. Tombras** (2014). Qam and psk ofdm rofso over  $m$ -turbulence induced fading channels. *IEEE Photonics Journal*, **7**(1), 1–11.
- Obeed, M., A. M. Salhab, S. A. Zummo, and M.-S. Alouini** (2018). Joint optimization of power allocation and load balancing for hybrid vlc/rf networks. *Journal of Optical Communications and Networking*, **10**(5), 553–562.
- Odeyemi, K. O., G. Aiyetoro, P. A. Owolawi, and O. O. Olakanmi** (2021). Performance analysis of reconfigurable intelligent surface in a dual-hop df relay empowered asymmetric rf/fso networks. *Optical and Quantum Electronics*, **53**(11), 1–17.
- Palliyembil, V., J. Vellakudiyan, and P. Muthuchidambaranathan** (2018). Asymptotic bit error rate analysis of free space optical systems using spatial diversity. *Optics Communications*, **427**, 617–621.
- Pati, P. S. and P. Krishnan** (2019). Modelling of ofdm based rofso system for 5g applications over varying weather conditions: A case study. *Optik*, **184**, 313–323.
- Pham, H. T., N. T. Dang, and A. T. Pham** (2014). Effects of atmospheric turbulence and misalignment fading on performance of serial-relaying m-ary pulse-position modulation free-space optical systems with partially coherent gaussian beam. *IET communications*, **8**(10), 1762–1768.
- Pham, T. V., T. C. Thang, and A. T. Pham** (2018). Average achievable rate of spatial diversity mimo-fso over correlated gamma–gamma fading channels. *Journal of Optical Communications and Networking*, **10**(8), 662–674.
- Prabu, K., D. S. Kumar, and R. Malekian** (2014). BER analysis of BPSK-SIM-based SISO and MIMO FSO systems in strong turbulence with pointing errors. *Optik*, **125**(21), 6413–6417.
- Rahman, A., M. S. Anuar, S. A. Aljunid, and M. Junita**, Study of rain attenuation consequence in free space optic transmission. *In 2008 6th National Conference on Telecommunication Technologies and 2008 2nd Malaysia Conference on Photonics*. IEEE, 2008.

- Ramavath, P. N., S. A. Udupi, and P. Krishnan** (2020a). Experimental demonstration and analysis of underwater wireless optical communication link: Design, bch coded receiver diversity over the turbid and turbulent seawater channels. *Microwave and Optical Technology Letters*, **62**(6), 2207–2216.
- Ramavath, P. N., S. A. Udupi, and P. Krishnan** (2020b). High-speed and reliable underwater wireless optical communication system using multiple-input multiple-output and channel coding techniques for IoUT applications. *Optics Communications*, **461**, 125229.
- Saari, J. I., M. M. Krause, B. R. Walsh, and P. Kambhampati** (2013). Terahertz bandwidth all-optical modulation and logic using multiexcitons in semiconductor nanocrystals. *Nano letters*, **13**(2), 722–727.
- Saeed, R. A. and E. B. Abbas**, Performance evaluation of mimo fso communication with gamma-gamma turbulence channel using diversity techniques. *In 2018 International Conference on Computer, Control, Electrical, and Electronics Engineering (ICCCEEE)*. IEEE, 2018.
- Safi, H., A. Dargahi, and J. Cheng**, Performance analysis of fso mimo multiplexing links with beam wander and nonzero boresight pointing errors. *In 2019 16th Canadian Workshop on Information Theory (CWIT)*. IEEE, 2019.
- Sandalidis, H. G., T. A. Tsiftsis, and G. K. Karagiannidis** (2009). Optical wireless communications with heterodyne detection over turbulence channels with pointing errors. *Journal of lightwave technology*, **27**(20), 4440–4445.
- Sandeep, V., D. S. Gurjar, S. Yadav, P. Pattanayak, and Y. Jiang** (2022). On the performance analysis of v2n mixed rf and hybrid fso/rf communication system. *IEEE Photonics Journal*, **14**(6), 1–14.
- Schulz, P., M. Matthe, H. Klessig, M. Simsek, G. Fettweis, J. Ansari, S. A. Ashraf, B. Almeroth, J. Voigt, I. Riedel, et al.** (2017). Latency critical iot applications in 5g: Perspective on the design of radio interface and network architecture. *IEEE Communications Magazine*, **55**(2), 70–78.
- Selvi, M. and K. Murugesan** (2012). Performance of ofdm based fso communication systems using m-ary psk modulation. *International Journal of Computer Applications*, **49**(7), 41–45.

- Seymour, T., A. Shaheen, et al.** (2011). History of wireless communication. *Review of Business Information Systems (RBIS)*, **15**(2), 37–42.
- Shafi, M., A. F. Molisch, P. J. Smith, T. Haustein, P. Zhu, P. De Silva, F. Tufvesson, A. Benjebbour, and G. Wunder** (2017). 5g: A tutorial overview of standards, trials, challenges, deployment, and practice. *IEEE journal on selected areas in communications*, **35**(6), 1201–1221.
- Sharma, V. and G. Kaur** (2013). High speed, long reach ofdm-fso transmission link incorporating ossb and otsb schemes. *Optik*, **124**(23), 6111–6114.
- Sinefeld, D., D. Shayovitz, O. Golani, and D. M. Marom**, Adaptive rate and bandwidth wdm optical sampling pulse streams with lcos-based photonic spectral processor. In *2013 Optical Fiber Communication Conference and Exposition and the National Fiber Optic Engineers Conference (OFC/NFOEC)*. IEEE, 2013.
- Singh, C., J. John, Y. Singh, and K. Tripathi** (2002). A review of indoor optical wireless systems. *IETE Technical review*, **19**(1-2), 3–17.
- Singh, H. and A. S. Sappal** (2019). Analytic and simulative comparison of turbulent fso system with different modulation techniques. *Optics & Laser Technology*, **114**, 49–59.
- Singh, M. and J. Malhotra** (2020). Performance comparison of  $2 \times 20$  gbit/s-40 ghz ofdm based rofso transmission link incorporating mdm of hermite gaussian modes using different modulation schemes. *Wireless Personal Communications*, **110**, 699–711.
- Soni, G. and J. Malhotra** (2011). Free space optics system: performance and link availability. *International journal of computing and corporate research*, **1**(3), 24.
- Stefanovic, C., M. Morales-Céspedes, and A. G. Armada** (2021). Performance analysis of ris-assisted fso communications over fisher–snedecor f turbulence channels. *Applied Sciences*, **11**(21), 10149.
- Tang, X., Z. Ghassemlooy, S. Rajbhandari, W. O. Popoola, and C. G. Lee** (2012). Coherent heterodyne multilevel polarization shift keying with spatial diversity in a free-space optical turbulence channel. *Journal of lightwave technology*, **30**(16), 2689–2695.

- Tang, X., S. Rajbhandari, W. O. Popoola, Z. Ghassemlooy, E. Leitgeb, S. S. Muhammad, and G. Kandung**, Performance of bpsk subcarrier intensity modulation free-space optical communications using a log-normal atmospheric turbulence model. *In 2010 Symposium on Photonics and Optoelectronics*. IEEE, 2010.
- Torabi, M., N. Mohammadi, and C. Nerguizian** (2022). Performance analysis of an asymmetric two-hop amplify-and-forward relaying rf-fso system in a cognitive radio with partial relay selection. *Optics Communications*, **505**, 127478.
- Trichili, A., A. Ragheb, D. Briantcev, M. A. Esmail, M. Altamimi, I. Ashry, B. S. Ooi, S. Alshebeili, and M.-S. Alouini** (2021). Retrofitting fso systems in existing rf infrastructure: A non-zero-sum game technology. *IEEE Open Journal of the Communications Society*, **2**, 2597–2615.
- Tsiftsis, T.** (2008). Performance of heterodyne wireless optical communication systems over gamma-gamma atmospheric turbulence channels. *Electronics Letters*, **44**(5), 372–373.
- Tsiftsis, T. A., H. G. Sandalidis, G. K. Karagiannidis, and M. Uysal** (2009). Optical wireless links with spatial diversity over strong atmospheric turbulence channels. *IEEE Transactions on Wireless Communications*, **8**(2), 951–957.
- Vailshery, L. S.** (2023). Number of Internet of Things (IoT) connected devices worldwide from 2019 to 2023, with forecasts from 2022 to 2030. <https://www.statista.com/statistics/1183457/iot-connected-devices-worldwide/>. [Online; accessed 04-september-2023].
- Vorontsov, M. A., G. W. Carhart, and J. C. Ricklin** (1997). Adaptive phase-distortion correction based on parallel gradient-descent optimization. *Optics letters*, **22**(12), 907–909.
- Wang, H., Z. Zhang, B. Zhu, J. Dang, L. Wu, L. Wang, K. Zhang, and Y. Zhang** (2020a). Performance of wireless optical communication with reconfigurable intelligent surfaces and random obstacles. *arXiv preprint arXiv:2001.05715*.
- Wang, H., Z. Zhang, B. Zhu, J. Dang, L. Wu, L. Wang, K. Zhang, Y. Zhang, and G. Y. Li** (2021). Performance analysis of multi-branch reconfigurable intelligent surfaces-assisted optical wireless communication system in environment with obstacles. *IEEE Transactions on Vehicular Technology*, **70**(10), 9986–10001.

- Wang, J., W. Zhang, X. Bao, T. Song, and C. Pan**, Outage analysis for intelligent reflecting surface assisted vehicular communication networks. *In GLOBECOM 2020-2020 IEEE Global Communications Conference*. IEEE, 2020b.
- Wang, P., R. Wang, L. Guo, T. Cao, and Y. Yang** (2016). On the performances of relay-aided fso system over m distribution with pointing errors in presence of various weather conditions. *Optics Communications*, **367**, 59–67.
- Wang, Y., D. Wang, and J. Ma** (2015). On the performance of coherent ofdm systems in free-space optical communications. *IEEE photonics journal*, **7**(4), 1–10.
- Wang, Y., W. Zhang, Y. Chen, C.-X. Wang, and J. Sun** (2022). Novel multiple ris-assisted communications for 6g networks. *IEEE Communications Letters*, **26**(6), 1413–1417.
- Williams, W. D., M. Collins, D. M. Boroson, J. Lesh, A. Biswas, R. Orr, L. Schuchman, and O. S. Sands**, Rf and optical communications: A comparison of high data rate returns from deep space in the 2020 timeframe. *In 12th Ka and Broadband Communications Conference*, E-15723. 2007.
- Wilson, K., P. Leatherman, R. Cleis, J. Spinhirne, and R. Fugate** (1997). Results of the compensated earth-moon-earth retroreflector laser link (cemerll) experiment. Technical report.
- wolfram** (2001a). wolfram research. <https://functions.wolfram.com/07.34.21.0084.01>. [Online; accessed september-2023].
- wolfram** (2001b). wolfram research. <https://functions.wolfram.com/06.27.26.0006.01>. [Online; accessed september-2023].
- Wu, Q., S. Zhang, B. Zheng, C. You, and R. Zhang** (2021). Intelligent reflecting surface-aided wireless communications: A tutorial. *IEEE Transactions on Communications*, **69**(5), 3313–3351.
- Yang, L., X. Gao, and M.-S. Alouini** (2014). Performance analysis of free-space optical communication systems with multiuser diversity over atmospheric turbulence channels. *IEEE Photonics Journal*, **6**(2), 1–17.

- Yang, L., W. Guo, and I. S. Ansari** (2020a). Mixed dual-hop fso-rf communication systems through reconfigurable intelligent surface. *IEEE Communications Letters*, **24**(7), 1558–1562.
- Yang, L., F. Meng, Q. Wu, D. B. Da Costa, and M.-S. Alouini** (2020b). Accurate closed-form approximations to channel distributions of ris-aided wireless systems. *IEEE Wireless Communications Letters*, **9**(11), 1985–1989.
- Yang, L., F. Meng, J. Zhang, M. O. Hasna, and M. Di Renzo** (2020c). On the performance of ris-assisted dual-hop uav communication systems. *IEEE Transactions on Vehicular Technology*, **69**(9), 10385–10390.
- Yigit, Z., E. Basar, and I. Altunbas** (2020). Low complexity adaptation for reconfigurable intelligent surface-based mimo systems. *IEEE Communications Letters*, **24**(12), 2946–2950.
- Yilmaz, O. N., Y.-P. E. Wang, N. A. Johansson, N. Brahmi, S. A. Ashraf, and J. Sachs**, Analysis of ultra-reliable and low-latency 5g communication for a factory automation use case. In *2015 IEEE international conference on communication workshop (ICCW)*. IEEE, 2015.
- Yuan, X., Y.-J. A. Zhang, Y. Shi, W. Yan, and H. Liu** (2021). Reconfigurable-intelligent-surface empowered wireless communications: Challenges and opportunities. *IEEE wireless communications*, **28**(2), 136–143.
- Zedini, E. and M.-S. Alouini** (2015). Multihop relaying over im/dd fso systems with pointing errors. *Journal of Lightwave Technology*, **33**(23), 5007–5015.
- Zeng, M., X. Li, G. Li, W. Hao, and O. A. Dobre** (2020). Sum rate maximization for irs-assisted uplink noma. *IEEE Communications Letters*, **25**(1), 234–238.
- Zhang, D., S. Hao, Q. Zhao, L. Wang, Q. Zhao, and X. Wan**, High-throughput interleaving scheme in free space optical communication system. In *2017 IEEE 17th International Conference on Communication Technology (ICCT)*. IEEE, 2017.
- Zhou, H., S. Mao, and P. Agrawal**, Optical power allocation for adaptive wdm transmissions in free space optical networks. In *2014 IEEE wireless communications and networking conference (WCNC)*. IEEE, 2014.



# Publications Based on the Thesis

## Journals:

1. **Abhishek Kumar**, and Prabu Krishnan. “RoFSO system based on BCH and RS coded BPSK OFDM for 5G applications in smart cities” *Optical and Quantum Electronics* 54.1 (2022): 18.  
<https://doi.org/10.1007/s11082-021-03392-y>
2. **Abhishek Kumar**, and Prabu Krishnan. “Performance analysis of radio-over-free-space optical communication system with spatial diversity over combined channel model” *Optical and Quantum Electronics* 54.4 (2022): 211. <https://doi.org/10.1007/s11082-022-03604-z>
3. **Abhishek Kumar**, Prabu Krishnan and A. Arockia Bazil Raj. “Performance analysis of a RIS-assisted RoFSO communication system over Malaga distribution for smart city applications.” *Applied Optics* 62.19 (2023): 5325-5333.  
<https://doi.org/10.1364/AO.493878>
4. **Abhishek Kumar**, and Prabu Krishnan. “Performance Analysis of Multi-RIS enabled RoFSO System for V2I Communications” (Under Review in *Optical and Quantum Electronics*)



# CURRICULUM VITAE

## Abhishek Kumar

S/o Arjun Prasad, Rishi Bhawan, Makchund Toli,  
Chutia, Ranchi, Jharkhand- 834001

☎ : +91 9205952067

✉ : abhishekranchi01@gmail.com

## EDUCATIONAL QUALIFICATIONS

### Doctor of Philosophy (Ph.D.)

National Institute of Technology Karnataka, Surathkal 2020–Till date

### Master of Technology (M.Tech)

Defence Institute Of Advanced Technology, Pune. 2017–2019

Branch : Optical Communicaiton and Photonics

### Bachelor of Engineering (B.E.)

Sant Longowal Institute of Engineering and Technology, Longowal. 2013–2016

Branch : Instrumentation and control Engineering

### Diploma

Sant Longowal Institute of Engineering and Technology, Longowal. 2011–2013

Branch :Instrumentation and Process control

## Research Interests:

Free Space Optical commnuication (FSOC), Underwater wireless optical commu-  
nication (UWOC), Visible light communication (VLC), Satellite to ground optical  
cpommunication.

## Publications:

- Abhishek Kumar, and Prabu Krishnan. “Performance analysis of RoFSO links with spatial diversity over combined channel model for 5G in smart city applications” Optics Communications 466 (2020): 125600.
- Abhishek Kumar, and Prabu Krishnan. “RoFSO system based on BCH and RS coded BPSK OFDM for 5G applications in smart cities” Optical and Quantum Electronics 54.1 (2022): 18.

- Abhishek Kumar, and Prabu Krishnan. “Performance analysis of radio-over-free-space optical communication system with spatial diversity over combined channel model” *Optical and Quantum Electronics* 54.4 (2022): 211.
- Abhishek Kumar, Prabu Krishnan and A. Arockia Bazil Raj. “Performance analysis of a RIS-assisted RoFSO communication system over Malaga distribution for smart city applications.” *Applied Optics* 62.19 (2023): 5325-5333.